Cogging Torque Reduction for Interior Permanent Magnet Synchronous Motors

Master Thesis
Miquel Tost Candel | 2293132
M. Sc. Electrical Engineering

TECHNISCHE UNIVERSITÄT DARMSTADT

Institut für Elektrische Energiewandlung

Miquel Tost Candel
Matriculation number: 2293132
M. Sc. Electrical Engineering

Master Thesis
“Cogging Torque Reduction for Interior Permanent Magnet Synchronous Motors”

Submitted on: 15.09.2016

Supervisor: M. Sc. Jeongki An

Prof. Dr.-Ing. habil. Dr. h.c. Andreas Binder
Institute of Electrical Energy Conversion
Department of Electrical Engineering and Information Technology
Technical University of Darmstadt
Landgraf-Georg-Str. 4
64283 Darmstadt

Declaration of honor

I solemnly declare that I have written this Master Thesis independently and the other sources that I have been used in the present document are referenced as such.
This Master Thesis has not been submitted to any examination board and not yet been published.

Darmstadt, 15.09.2016

Acknowledgments

I want to express my gratitude to my home university “Polytechnic University of Catalonia” and the receiving university “Technische Universität Darmstadt” for the agreement between both institutions which makes my Erasmus experience possible. Secondly I am also grateful for the “Institute of Electrical Energy Conversion”, which provided me a master topic and a good work atmosphere. This master thesis would not be possible without the help and supervision of my tutor M. Sc. Jeongki An, with whom I have learned and understood a lot of concepts in the field of electrical machines.

Most important, I would like to express my eternal gratefulness to my family. They are the reason why I am able to come this far despite numerous challenges. They are my greatest pillar of support, both emotionally and economically. For that few, but important contributions, I want to say thank you to Miquel, Maria José, Anna and Núria.

Contents

Declaration of honor iv

Acknowledgments v

Contents vi

List of Figures viii

List of Tables xi

Nomenclature xii

Abstract xviii

1.....Introduction 1

2.....Theoretical background 2

2.1. Synchronous machines 2

2.2. Rotor configurations for permanent magnet synchronous machines (PMSM) 3

2.3. Permanent magnet properties 4

2.4. Stator windings design 7

2.4.1. Concentrated and distributed windings 7

2.4.2. One and two layer windings 7

2.4.3. Arrangement of the stator winding 8

2.4.4. Calculation of integer and fractional distributed winding 9

2.4.5. Winding factor 10

2.5. Maxwell stress tensor for cogging torque and radial pressure calculation 15

2.6. Cogging torque 16

2.7. Torque ripple 17

2.8. Minimization of cogging torque and torque ripple 18

2.8.1. Steeped and skewed rotor 18

2.8.2. Shape of stator slots and slot opening 18

2.8.3. Pole-arc to pole-pitch ratio optimization 19

2.8.4. Slotless construction 20

2.8.5. Fractional number of stator slots per pole and phase 20

2.9. Vibrations and electromagnetic noise in PMSM 23

2.10. Torque production and maximum torque per ampere (MTPA) technic 24

2.11. Flux weakening operation 27

2.12. Mechanical stress in iron bridges 28

2.13. Losses calculations 30

2.13.1. Ohmic losses 30

2.13.2. Iron losses 31

2.13.3. Friction losses 32

2.13.4. Motor efficiency 32

3.....Design of the IPMSM with fractional slot windings 33

3.1. Operational points of work 33

3.2. Materials 35

3.2.1. Laminated core material 35
3.2.2. Magnet material 36
3.3. Analytical calculations for the IPMSM 37
4. .... FEM modelling 45
4.1. Rotor core and V-shape magnets modelling 46
4.2. Stator core and coils modelling 47
5. .... Electromagnetic analysis of the FEM model 48
5.1. Design of the model 48
5.1.1. Variation of the angle between magnets 49
5.1.2. Variation of the dimensions of the stator slots 50
5.1.3. Irreversible demagnetization of the magnets for a sudden short-circuit 51
5.1.4. Mechanical stress in iron bridges 52
5.2. Results of the electromagnetic calculation of the machine at no-load condition 54
5.2.1. Magnetic flux density distribution 54
5.2.2. Induced phase voltage 56
5.2.3. Cogging torque 57
5.3. Results of the electromagnetic calculation of the machine at rated load condition 59
5.3.1. Voltage and current 59
5.3.2. Torque ripple and torque production with MTPA 60
5.3.3. Calculated parameters of $q = 1.5$ model 61
5.3.4. Maximum torque for loss minimization 63
5.4. Radial pressure for vibration and electromagnetic noise calculation 66
6. .... Comparisons of four IPMSM models 68
6.1. Parameters comparison between the 4 models 68
6.2. Magnetic flux distribution comparison between the 3 models 69
6.3. Cogging torque comparison between the 4 models 71
6.4. Radial pressure comparison between 3 models 73
6.5. Results comparison between 3 models 76
7. .... Conclusions 77
8. .... Annexes 79
8.1. Iron sheets material M270-35A from Sura® 79
8.2. Design parameters for the original model with $q = 2$ and $Q = 36$. 80
8.3. Design parameters for the 2nd Variation model with $q = 2.5$ and $Q = 45$. 81
References 82

List of Figures

Figure 1: Classification of the main different types of synchronous machines with the saliency ratio (L_d/L_q) [1]..... 2
Figure 2: Location of the permanent magnets on the rotor. a), b) and c) are different configurations of surface mounted permanent magnets; d), e) and f) are different configurations of interior permanent magnets; g) interior permanent magnets for synchronous reluctance machine [15]..... 3
Figure 3: Hysteresis loop curve of the magnetization of a rare earth permanent magnet [3]. . 4
Figure 4: Second quadrant of the *B-H* curves of a N48M NdFeB permanent magnet. The graph shows the *B-H* curves for the influence on magnet temperature [14]. 5
Figure 5: Remanence and coercivity properties comparison between four permanent magnets at 20° [14]. 6
Figure 6: Stator windings with a concentrated stator winding (left) and a distributed stator winding (right) [21]..... 7
Figure 7: Two slots of a stator with one layer winding (left) and two layers winding (right) [25]. 8
Figure 8: The winding arrangements of two machines with fractional slot and two layer windning. a) unsymmetrical winding distribution, b) symmetrical winding distribution [15]. 8
Figure 9: Integer slot winding distribution. (a) Slot distance between the positive and negative sites of one coil; (b) Voltage diagram for each phase (*U*, *V*, and *W*); (c) Phasor diagram of the slots [1]. 9
Figure 10: Magnetic voltage calculation from a fully-pitched stator slots winding distribution [13]. 12
Figure 11: Magnetic voltage calculation from a short-pitched stator slots winding distribution [13]. 12
Figure 12: Magnetic voltage calculation from a fully-pitched stator slots winding distribution with group of coils $q = 2$ [13]. 12
Figure 13: Interaction of the magnetic field of the permanent magnets with the stator teeth [3]. 16
Figure 14: Calculation of the torque ripple from a time-graph at load condition. 17
Figure 15: Step-skewed rotor in three steps (C1, C2, and C3) [30]. 18
Figure 16: Different stator slots shapes for the minimization of the cogging torque: (a) notched teeth, (b) empty teeth, (c) closed slots, (d) teeth with different width on the active surface [14]..... 19
Figure 17: Pole-pitch to pole-arc coefficient in IPMSM for the reduction of cogging torque [31]. 19
Figure 18: Two brushless motors with a slotted configuration (left) and a slotless configuration (right) [32]..... 20
Figure 19: Park transformation from a three-phase reference frame to a *dq* reference frame [37]. 24
Figure 20: Motor model of a PMSM in *dq* reference frame. 24
Figure 21: Flux path of a SPMSM. (a) *q*-axis flux path and (b) *d*-axis flux path [2]. 25
Figure 22: Flux path of an IPMSM. (a) *q*-axis flux path and (b) *d*-axis flux path [2]..... 26
Figure 23: For a given torque there is a combination of currents I_d and I_q, which is the lowest value to minimize the copper losses [2]..... 26

Figure 24: Variables (stator voltage, power, torque, and back-emf) of a PMSM with the increase of speed [3]. 27
Figure 25: Phasor diagram of a PMSM working in the flux weakening operation. 27
Figure 26: IPMSM with buried V-shape magnets. The parameters for the mechanical stress calculations are drawn. The red area is the equivalent area A_{equiv}, the blue areas are the magnets A_M and the green one is the iron area A_{Fe} considered for the calculation. 28
Figure 27: Schematic stress/strain curve for a material with the yield strength R_e, the 0.2%-yield strength $R_{p,\,0.2\%}$ and the tensile strength R_m points [39]. 29
Figure 28: *S-N* curve for the fatigue properties of a given material [40]..... 29
Figure 29: Current displacement effect. Conductor current I, slot magnetic flux B, slot height h, current density J [13]..... 30
Figure 30: Operational points of the machine at nominal and maximum conditions. 34
Figure 31: *B-H* characteristic curve of the SURA® material M270-35A at 50 Hz [43]. 35
Figure 32: Magnetic flux density versus loss density for different values of frequency of the SURA® material M270-35A [43]. 36
Figure 33: *B-H* curve characteristic of the VACODYM 863 TP material for different operational point´s temperatures [44]. 36
Figure 34: Phasor diagram distribution of the fractional slot distributed winding of 27 slots and 6 poles..... 38
Figure 35: Voltage phase diagram of the fractional slot distributed winding of 27 slots and 6 poles. 39
Figure 36: Slot coils sequence for a basic phasor diagram which corresponds to 9 stator slots. 40
Figure 37: Stator slot parameters..... 42
Figure 38: JMAG® screens. (Upper) is the project manager screen, (below) is the geometry editor for CAD. 45
Figure 39: Drawings of the rotor core (green) and V-shape magnets (purple) with the geometry editor of JMAG® software. 46
Figure 40: Drawings of the stator core (yellow) and coils (blue) with the geometry editor (CAD) of JMAG® software. This stator core belongs to a motor of $Q = 27$ and $q = 1.5$..... 47
Figure 41: FEM model of an IPMSM with $q = 1.5$, $Q = 27$, $m = 3$ and $p = 3$. The main parts of the machine are displayed such as magnets (pink), rotor (green), stator (grey) and slots (green, red and blue). 48
Figure 42: Variation of the angle between magnets α_M for the model $q = 1.5$ and calculated results of cogging torque, torque ripple and efficiency. 49
Figure 43: Cogging torque and torque ripple for each tooth width of the stator slots. 50
Figure 44: Magnetic field strength simulation for checking the demagnetized area of the magnets of 1 pole when a sudden short-circuit in the three phases is carried out. 51
Figure 45: Percentage of demagnetized area of 1 pole, for a given angle between the magnets α_M. 52
Figure 46: The calculated tangential stress (blue) on the iron bridge due to the centrifugal forces of the magnets for a given angle between magnets and half of the tensile strength (red) of the iron sheets SURA®, material M270-35A. 52
Figure 47: Mises Stress simulation for checking the iron bridge strength due to centrifugal forces at $n = 12000$ min^{-1} (left). Comparison of the Mises Stress simulated, at $n = 12000$ min^{-}

[1] and $\alpha_M = 120°$, and the limit of half of the maximum tensile strength that the material can support (right). 53
Figure 48: Magnetic flux density distribution thought the stator and rotor cores at no-load condition. 54
Figure 49: The radial component of the magnetic flux density (blue) and the fundamental component (red) in the air-gap at no-load condition. 55
Figure 50: FFT of the magnetic flux density in the air-gap at no-load condition. 55
Figure 51: Induced phase voltage at no-load condition. Phase *U* (blue), phase *V* (red) and phase *W* (green). 57
Figure 52: At no-load condition, simulation of the cogging torque M_{cog} for one electrical period *T*. 58
Figure 53: *Fourier* analysis of the cogging torque. 58
Figure 54: For one electrical period, the phase voltage *W* (red), the phase current *W* (green) and the fundamental component of the phase voltage *W* (blue) are displayed. 59
Figure 55: Torque response of the IPMSM $q = 1.5$ model for the rated load condition. It can be seen the torque response (blue) and the average torque (red). 60
Figure 56: Torque curve depending on the phase current and the current angle at rated speed $n = 4167\ \text{min}^{-1}$. MTPA technique finds the maximum torque *M* for a given stator current I_s by finding the optimal current angle β. 60
Figure 57: At the rated operational point; efficiency η and stator current I_s depending on the *d*-axis stator current I_{sd}. 64
Figure 58: At the rated operational point; iron losses $P_{d,Fe}$ and ohmic losses $P_{d,Cu,ac}$ depending on the d-axis stator current I_{sd}. 64
Figure 59: At the operational point for M_{max}; efficiency η and stator current I_s depending on the *d*-axis stator current I_{sd}. 65
Figure 60: At the operational point for M_{max}; iron losses $P_{d,Fe}$ and ohmic losses $P_{d,Cu,ac}$ depending on the d-axis stator current I_{sd}. 66
Figure 61: Radial pressure at no-load and load condition caused by the electromagnetic forces for the model $q = 1.5$. 66
Figure 62: *Fourier* analysis of the radial pressure at no-load and load condition for the model $q = 1.5$. 67
Figure 63: (a) Original model with $q = 2$, (b) 1st Variation model with $q = 1.5$, (c) 2nd Variation model with $q = 2.5$. 68
Figure 64: Fourier analysis of the magnetic flux distribution, at no-load, for the models with $q = 2$, $q = 1.5$ and $q = 2.5$. 70
Figure 65: Cogging torque waves for each IPMSM model. 71
Figure 66: For each model, the periodicity of the cogging torque for 1 slot pitch. 72
Figure 67: *Fourier* analysis of the cogging torque for each IPMSM model. 72
Figure 68: Radial pressure distribution calculated from the magnetic flux distribution, at no-load condition for each model. 74
Figure 69: Radial pressure distribution calculated from the magnetic flux distribution, at load condition for each model. 74
Figure 70: *Fourier* analysis of the radial pressure at no-load condition for the Original, 1st Variation and 2nd Variation. 75
Figure 71: *Fourier* analysis of the radial pressure at load condition for the Original, 1st Variation and 2nd Variation. 75

List of Tables

Table 1: Winding definitions for fractional slot machines [15]. 10
Table 2: Winding factor calculation for a fully-pitched group of coils $q = 2$. 13
Table 3: Winding factor calculation for a fractional slot winding $q = 1.5$ with $W/\tau_p = 4/4.5$. 14
Table 4: The first rotor harmonic orders, which contribute to the cogging torque generation for integer and fractional slot winding machines. 22
Table 5: Required parameters for each operational point for the design of the IPMSM. 34
Table 6: Calculation of a fractional slot distributed winding for a 2^{nd}-grade case. 37
Table 7: Calculated parameters for the pitch and distribution factors. 40
Table 8: Calculated parameters for the design of the IPMSM with fractional slot winding with $q = 1.5$. 44
Table 9: Calculated parameters for each variation of the angle between magnets for the model $q = 1.5$. 49
Table 10: Stator slots dimensions with the same slot area A_{Qs}. The parameters that vary are the teeth width b_{st} and the slot height h_{sl}. 50
Table 11: Calculated harmonic orders of the magnetic flux density distribution in the air-gap from the interaction of the rotor harmonics orders μ and the stator slots Q. 56
Table 12: Harmonic content of the cogging torque for $q = 1.5$. The parameters l and k for the analytically calculation of the harmonics numbers are shown for each harmonic order as well as the amplitude. 58
Table 13: For a given stator current I_s, the variation of produced torque between current angle β at 0° and the angle which gives maximum torque. 61
Table 14: Calculated parameters of $q = 1.5$ model for each operational point. 62
Table 15: Calculated results of the motor with $q = 1.5$ for each operational point. 63
Table 16: At the operational point for M_N; calculated parameters for the optimal points of MTPA and Loss Minimization techniques. 64
Table 17: At the operational point for M_{max}; calculated parameters for the optimal points of MTPA and Loss Minimization techniques. 65
Table 18: The main parameters of the four IPMSM models. 68
Table 19: Calculated parameters for the 4 IPMSM models at rated operational point of $M = 55$ Nm and $n = 4167$ min^{-1} 69
Table 20: Calculated rotor harmonics μ that contribute to the generation of the cogging torque for each model. 70
Table 21: For each model, the calculated periodicity and percentages values of the cogging torque. 71
Table 22: For each model, the highest harmonic amplitude and its order of the cogging torque. 73
Table 23: Final comparison between the 4 IPMSM models in terms of cogging torque, torque ripple, efficiency and the manufacturing associated costs. 76

Nomenclature

Abbreviations

ASM	Asynchronous Machine
SM	Synchronous Machine
IPM	Interior Permanent Magnet
SPM	Surface Permanent Magnet
IPMSM	Interior Permanent Magnet Synchronous Machine
SPMSM	Surface Permanent Magnet Synchronous Machine
AC	Alternating Current
DC	Direct Current
CAD	Computer-Aided Design
GCD	Greatest Common Divisor
FEA	Finite Element Analysis
FEM	Finite Element Method
FFT	Fast Fourier Transform
MTPA	Maximum Torque Per Ampere
MTPLM	Maximum Torque Per Loss Minimization
emf	electromotive force
mmf	magnetomotive force
PWM	Pulse Width Modulation

List of Symbols

a	-	number of parallel branches of winding in AC machines
a_i	-	number of parallel wires per turn
A	m^2	area
A	A/m	current loading
b	m	breadth
B	T	magnetic flux density
B_R	T	remanent magnetic flux density
c	m/s	traveling speed of sound
c_f	-	friction coefficient
C	$\mathrm{kV{\cdot}A{\cdot}min/m^3}$	*Esson*'s number, electromagnetic utilization
d	m	diameter
d_E	m	penetration depth

E	N/m^2	*Young´*s modulus
f	Hz	electric frequency
F	N	force
h	m	height
H	A/m	magnetic field strength
H_c	A/m	coercivity
I	A	current
J	T	magnetic polarization
J	A/m^2	electric current density
k	-	correction factors
k_c	-	*Carter´*s coefficient
k_d	-	distribution factor
k_f	-	fill factor
k_{Fe}	-	stack fill factor
k_p	-	pitch factor
k_{vd}	-	punching factor for iron losses in stator teeth
k_{vy}	-	punching factor for iron losses in stator yoke
k_W	-	winding factor
k_ϑ	-	temperature coefficient
$\overline{K}_{R2}$	-	current displacement factor
l	m	axial length
l_b	m	end winding length
L	H	self-inductance
L_w	dB	sound
$L_{\sigma b}$	H	stray inductance of the winding overhangs
m	-	number of phases
m	kg	mass
m_v	-	number of vertical wire layers
M	Nm	torque
M_{cog}	Nm	cogging torque
M_N	Nm	nominal torque
M_{rip}	Nm	torque ripple
n	1/min	rotational speed
n	-	denominator of q reduced at the lowest term
n_h	-	number of horizontal wire layers

N	-	number of fatigue cycles
N_c	-	number of turns per coil
N_{period}	-	number of cogging torque periods for one slot pitch
N_s	-	number of turns per phase
p	-	number of pole pairs
p	W/kg	loss density
p	N/mm^2	pressure
p^*	-	number of poles in a base phasor diagram
P	W	power
P_s	W	sound power level reference
q	-	number of slots per pole and phase
Q	-	number of stator slots
Q^*	-	number of stator slots in one phasor diagram
r	m	radius
R	Ω	electrical resistance
$\mathcal{R}$	1/H	reluctance
R_e	N/m^2	yield strength
Re	-	*Reynolds* number
R_m	N/m^2	tensile strength
$R_{p,0,2}$	N/m^2	0,2%-yield strength
s_Q	M	slot opening
S	V·A	apparent power
S	N/m^2	mechanical stress
t	-	number of the electrically equal slots sequences
t	s	time
T	s	time constant, duration of period
T	K	absolute temperature
U	V	electric voltage
U	-	stator phase U
$U_{p,0}$	V	back-emf, synchronous generated voltage
v	m/s	velocity
V	m^3	volume
V	-	stator phase V
W	m	coil width
W	-	stator phase W

x	m	displacement, circumferential coordinate
X	Ohm	reactance
y_Q	-	distance in slots between two wound slots
z	-	numerator of q reduced at the lowest term
α_e	-	equivalent pole coverage ratio
α_M	°	angle between magnets of one pole
α_Q	°	slot angle
α_u	°	angle between two adjacent slots
α_z	°	angle between two wound slots
β	°	phase current angle between I_s and q-axis
γ	°	circumferential angle
δ	m	air-gap width
η	-	efficiency
ϑ	°C	temperature
Θ	A	ampere turns
κ	S/m	electric conductivity
μ	-	ordinal number of rotor space harmonics
μ_0	Vs/(A·m)	magnetic permeability of vacuum ($4\pi \cdot 10^{-7}$ Vs/(Am))
μ_r	-	relative permeability
ν	-	ordinal number of stator space harmonics
ν	m²/s	kinematic viscosity
ρ	kg/m³	mass density
ρ	m	electric resistivity
ξ	-	reduced conductor height
σ	N/m^2	mechanical stress
σ_s	-	coefficient of stray flux in stator core
τ_p	m	pole pitch
τ_Q	m	stator slot pitch
φ	°	phase angle
Φ	Wb	magnetic flux
Ψ	Vs	magnetic flux linkage
ω	rad/s	electric angular frequency
ω	rad/s	natural angular frequency (“Eigen-frequency”)
ω_m, Ω_m	rad/s	mechanical angular frequency

Subscripts

0	no-load, initial
1	fundamental wave, starting
a	axis
a	armature
ac/AC	alternating current
av	average
c	coil
cog	cogging
crit	critical
Cu	copper
d	direct axis stator component, distribution, total losses
dc/DC	direct current
el	electrical
equiv	equivalent
exc	excitation
f	field
fr	friction
Fe	iron
Ft	Foucault
Hy	Hysteresis
i	inner, induced, internal
in	input
k	short-circuit
m	mechanical
mag	magnetic
max	maximum
min	minimum
M	magnet
N	rated
o	outer
out	output
OP1	operational point 1
OP2	operational point 2
OP3	operational point 3

p	pole, pitch
period	period
ph	phase
PM	permanent magnet
q	quadrature axis stator component
Q	slot
r	rotor, radial
ref	reference
rip	ripple
s	shaft
s	stator
skew	skew
sl	slot
st	stator tooth
syn	synchronous
t	tangential, tooth
th	thermal, theoretical
y	yoke
w	winding

Abstract

Interior permanent magnet synchronous machines show a good range of behaviours, which make these kinds of machines good candidates for an electromechanical energy conversion. However, in order to improve their accuracy in their torque responses, the cogging torque and torque ripple phenomena should be mitigated to obtain better performance of the machine.
In order to reduce the cogging torque and torque ripple, control techniques as well as geometric parameters of the machine have to be improved. In this thesis, geometric parameters such as the use of the fractional slot windings, the improvement of the pole-arc to pole-pitch ratio and the dimensions of the stator slots are considered for the better minimization of the cogging torque and torque ripple.
The results are presented to show the performance of the IPMSM with fractional slot windings as well as the reduction of the cogging torque and torque ripple. Furthermore, four models of IPMSM with fractional and integer slot windings are going to be compared with the aim of the attenuation of the cogging torque phenomenon.

1. Introduction

In many applications, interior permanent magnet synchronous machines (IPMSM) have been chosen to achieve an electromechanical energy conversion. These kinds of machines have some advantages over other electrical machines. For example, having the magnets mounted in the interior of the rotor makes these machines more compact. IPMSM have higher efficiency since they do not have electrical excitation and hence fewer losses in the rotor. In some applications IPMSM do not require gear case since there is the control of power electronics, which avoid some mechanical losses in the electromechanical conversion [1]. Having the magnets mounted inside the rotor generates a difference between the direct and quadrature reactances for magnetic path. Therefore a higher saliency ratio is achieved, which allows IPMSM to produce additional reluctance torque and hence a high torque density is achieved [2]. In addition, they can work in a wide range of speeds since a strong field weakening control can be achieved. This operation cuts the increase of the voltage due to the rise of the speed and consequently the inverter can be smaller [3]. For IPMSM, the rotation of the magnets inside the rotor at high speeds causes the rotor bridges to suffer mechanical stress due to the centrifugal forces [4]. This structure can protect the magnets from irreversible demagnetization like in case of a sudden short-circuit, which reduces the torque on the machine due to the reduction of the remanent magnetic field density [5]. However, having a short air-gap contributes to more harmonics that can cross the air-gap. Furthermore, the reluctance variation between the magnets of the rotor and the stator teeth is more noticeable and phenomena such as cogging torque and torque ripple appear. In many applications both cogging torque and torque ripple are important enough to be studied and reduced.

A lot of applications need an accurate response such as tooling machines working in high speeds; other applications need the mitigation of the cogging torque when they are in the phase of the start-up such as the wind turbines [6]. In addition, many applications are interested in the reduction of the cogging torque since it contributes to vibration of the stator structure and hence more noise is generated from these machines. It is desirable to reduce the cogging torque since it does not contribute to generate work torque and it contributes to generate ripple torque, vibrations and acoustic noise [7]. Several techniques are employed to reduce the unwanted cogging torque and torque ripple. There are two main groups, the solutions that involve geometrical parameters and the ones that are related with control and power supply of the machine [8]. In this thesis the aim of reducing cogging torque and torque ripple relies on the geometrical construction of the IPMSM. Previous researches tried to reduce the cogging torque using optimal pole-pitch to pole-arc ratios [9], different magnet design [8], reducing the slop opening width [10], skewing the rotor or stator [9] [11], using slotless constructions [12].

In this case, the purpose of the thesis is changing the number of stator slots per pole and phase to a fractional number. For that, several calculations are done to design an IPMSM with fractional slot windings. The designed model is implemented in JMAG®, which is software for a finite element analysis. The implemented model is analysed by using the *Maxwell* stress tensor to calculate the electromagnetic forces in the air-gap, at no-load and load condition of the machine, which are the responsible ones of the torque generation and hence the cogging torque and torque ripple. This proposed model will be compared with a previous model with integer number of stator slots per pole and phase as well as with two other models that improves the reduction of the cogging torque; a step-skewed IPMSM and a second model of fractional slot windings with a larger value of slots per pole and phase.

2. Theoretical background

2.1. Synchronous machines

Synchronous machines encompass a large group of electrical machines. The latter are made up of three main groups, namely electrical excited synchronous machines, permanent magnet synchronous machines and reluctance synchronous machines. Inside each family, different types of machines can be found. Both the electrical excited or permanent magnet synchronous machines have either saliency or non-saliency ratio, which arises from the difference between the direct and quadrature inductances. This saliency ratio can contribute to the generation of reluctance torque, which increases the total amount of torque produced by the machine. The surface mounted permanent magnet synchronous machine is considered, in principle, non-saliency due to the long equivalent distance of the air-gap and the small difference between inductances due to their quasi equal flux path. In contrary the interior permanent magnet synchronous machine is salient pole machine, which produces an additional reluctance torque [1]. This will be discussed in section 2.10.

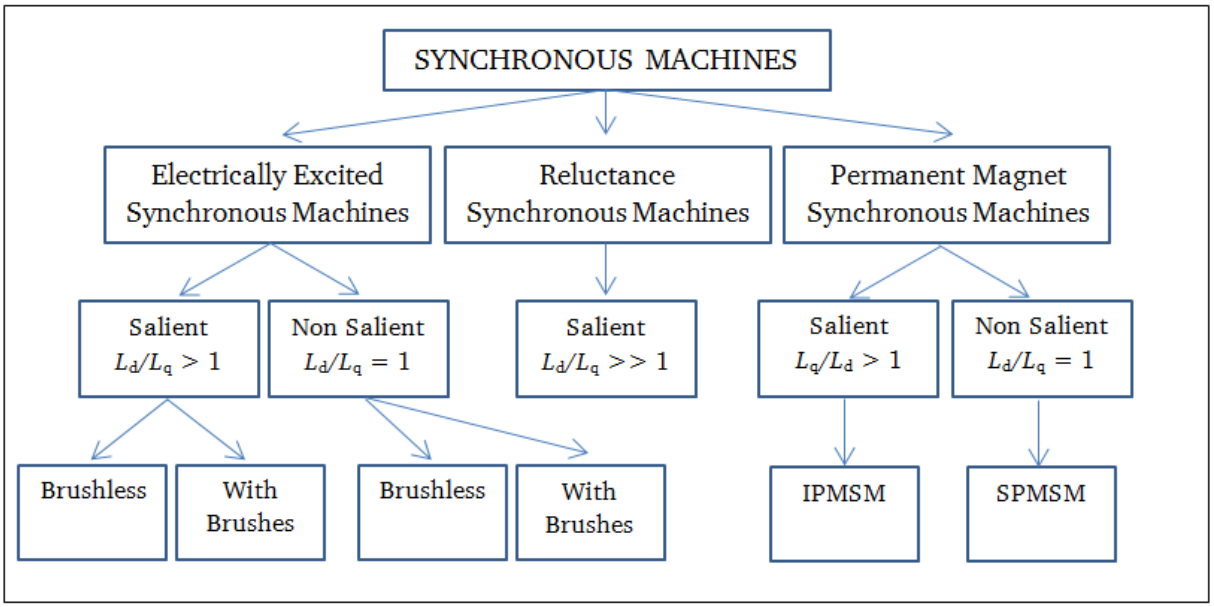

Figure 1: Classification of the main different types of synchronous machines with the saliency ratio (L_d/L_q) [1].

The most common synchronous machine is the slotted stator with three-phase winding, which can be built with an electrical excited rotor by coils or an excited rotor by permanent magnets. The machines can be either work as a motor or a generator. First operation mode is caused by the interaction of the rotor magnetic field and the stator rotating field, which is generated from the power supply. The stator field drags the rotor synchronously. When an external force drives the rotor together with the rotating rotor field creating an alternating flux linkage in the stator winding, this induces a voltage in the stator windings and the second mode is achieved [13]. Normally, permanent magnet rotors are preferred over small synchronous machines in order to avoid the maintenance and the rotor losses by the electrical excitation, thus achieving better efficiencies. In spite of those advantages, for large synchronous machines it is preferred to have an electrically excited rotor by a DC current in order to regulate any demands of the power factor of the line [13]. In addition, the interior permanent magnet synchronous machines (IPMSM) can be directly coupled to the drive or load, thus no gear box is required. This avoids maintenance and reduces mechanical losses.

2.2. Rotor configurations for permanent magnet synchronous machines (PMSM)

There exist several rotor configurations for the case of synchronous machines excited by permanent magnets. The most commonly used configurations are surface permanent magnets (SPM) and interior permanent magnets (IPM) types as Figure 2 shows. Interior permanent magnets synchronous machines (IPMSM) have the magnets inside the rotor. These configurations have the value of the inductance in direct axis L_d smaller than in quadrature axis L_q due to the different equivalent air-gap distance $L \sim 1/\delta_{equiv}$ [14]. Permanent magnets in surface mounted synchronous machines (SPMSM) can be radially or circumferentially magnetized. Normally, in SPMSM the difference between direct L_d and quadrature L_q inductances is low, which means that almost zero reluctance torque is provided since the saliency ratio is almost 1. IPMSM and SPMSM configurations are subjected to partial irreversible demagnetization of the magnets as well as mechanical stress due to the centrifugal forces of the magnets.

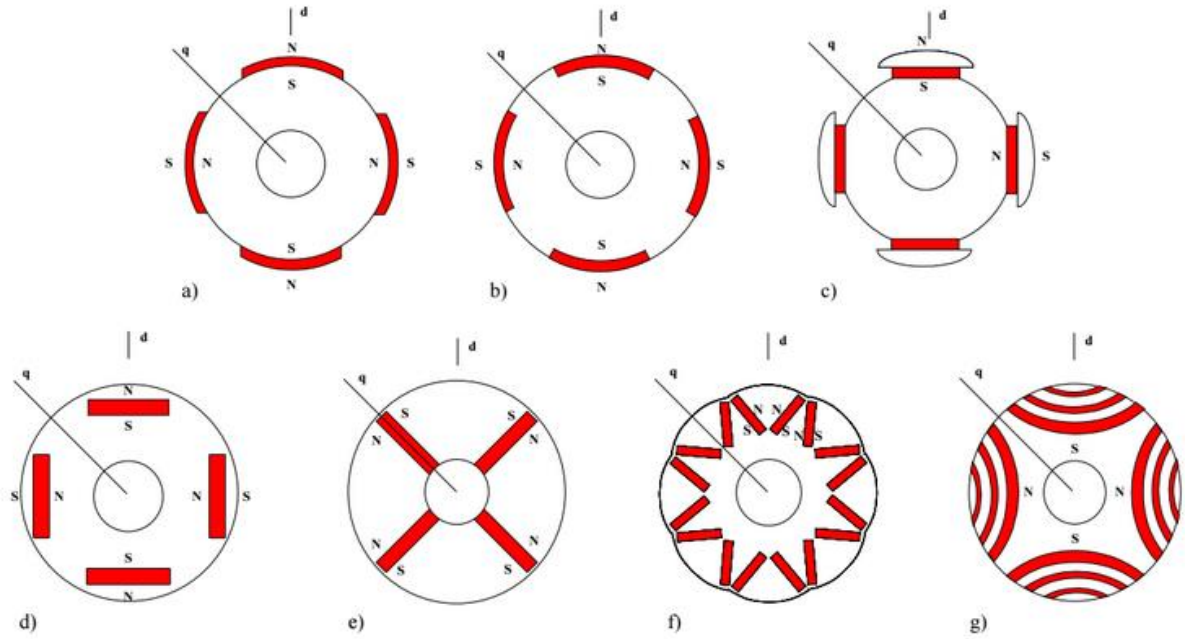

Figure 2: Location of the permanent magnets on the rotor. a), b) and c) are different configurations of surface mounted permanent magnets; d), e) and f) are different configurations of interior permanent magnets; g) interior permanent magnets for synchronous reluctance machine [15].

If a comparison is made between IPMSM and SPMSM machines, IPMSM have more load capability over the entire speed range. Furthermore, the maximum torque per ampere technic (MTPA) can be used to achieve better efficiency [16] [17]. IPMSM can produce more cogging torque due to the smaller air-gap, which contributes to a higher variation of the reluctance between the magnets of the rotor and the teeth of the stator. In addition, the magnets are sensitive to harmonic losses. SPMSM is easier to manufacturer but is affected by losses in the permanent magnets (PM). In order to reduce these PM losses, the magnets can be segmented, which reduces the area of the induced eddy currents. This method will reduce the losses and it will increase the cost of manufacturing time.
IPMSM suited for many applications due to high efficiency, high torque density, extended speed range and compact structure. For these reasons, IPMSMs are becoming attractive candidates in multiple purposes.

2.3. Permanent magnet properties

Permanent magnets have its origins from three common earth materials which are Iron (Fe), Nickel (Ni) and Cobalt (Co). These three materials need to be with other elements in order to increase the coercive field H_C. Thus, the most used permanent magnet materials are: AlNiCo, Ba-Ferrite and Sa-Ferrite and the rare earth magnets such as SmCo and NdFeB.
These permanent magnet materials are exposed to an external field H in order to have the same direction of magnetization in the whole magnet and also to give the permanent magnet a remanence flux density B_R. Figure 3 shows a magnetization process of a rare earth permanent magnet. The material is exposed to an external field H, which creates an own magnetic polarization J to the magnet. When the external field is switched off, the loop reaches the remanence magnetic flux density B_R [3].

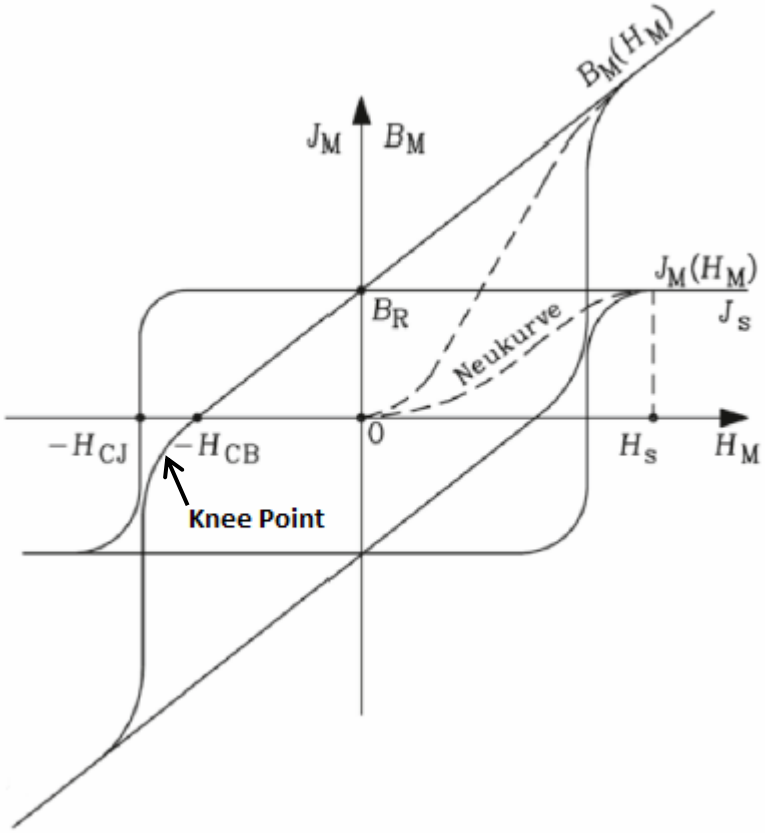

Figure 3: Hysteresis loop curve of the magnetization of a rare earth permanent magnet [3].

The remanence B_R of a permanent magnet is the property that a magnet has of keeping a flux density when the external field is removed. The value of this property will be important when a machine is going to be designed. Another important property is the coercive field strength H_c. This property shows the value of reverse field necessary to drive the magnetization to zero. After that moment, if the magnetic field has crossed the knee point, the permanent magnet is permanently demagnetized and cannot reach again the original remanence [14].
There are several cases, which causes permanent demagnetization of the permanent magnets, which have to be taken into account. One of them is when the air-gap is increased significantly, which make that the operation point of the flux density reaches below the knee point and it is irreversibly demagnetized 2.3-1.

$$B_\delta = \mu_0 \cdot H_\delta = -\mu_0 \cdot \frac{h_M}{\delta} \cdot H_M = B_M \tag{2.3-1}$$

where B_δ and B_M are the magnetic flux densities in the air-gap and of the permanent magnet respectively, H_δ and H_M are the magnetic field strengths in the air-gap and of the permanent magnet respectively, δ is the length of the air-gap, h_M is the height of the permanent magnet and μ_0 is the vacuum permeability, a value of $4\pi \cdot 10^{-7}$ N/A^2.
At load condition of the machine, the armature field acts against the magnetic field of the permanent magnets. In the interaction between both fields, if the armature field is strong enough to bring the magnetic field below the knee point, it will cause irreversible demagnetization on the magnets as equation 2.3-2 explains [3].

$$B_\delta = \mu_0 \cdot H_\delta = -\mu_0 \cdot (H_M - \Theta/h_M) \cdot \frac{h_M}{\delta} = B_M \tag{2.3-2}$$

Another problem, that the designers and manufacturers have to think about, is the maximum temperature of a permanent magnet working in a steady state. The increase in the temperature on magnets makes, that the coercive field decreases and the knee point is achieved earlier. Furthermore, the effect of increasing temperature also causes the remanence to decreases. Figure 4 illustrates the second quadrant of the *B-H* curves of a N48M NdFeB permanent magnet, when it is exposed to higher temperatures.

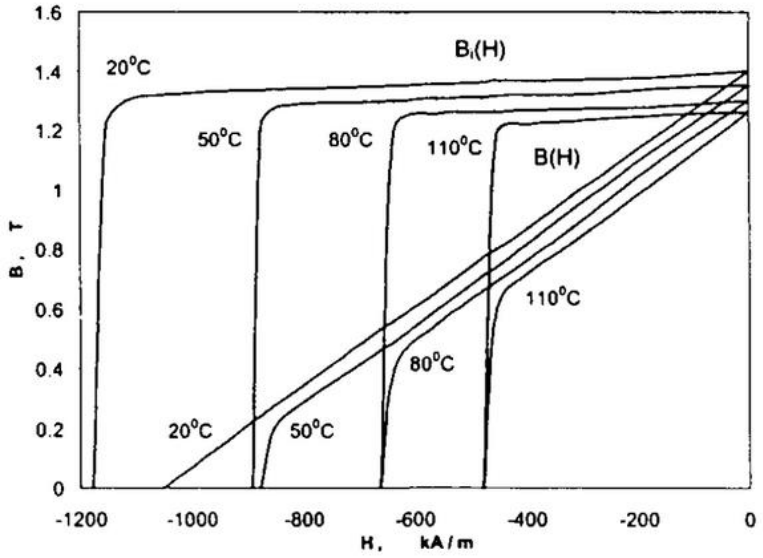

Figure 4: Second quadrant of the *B-H* curves of a N48M NdFeB permanent magnet. The graph shows the *B-H* curves for the influence on magnet temperature [14].

At the end, when the designers of the machines are going to select a type of permanent magnet, they have to think about different concepts such as remanence, coercivity, demagnetization, losses and price. As it can be seen in Figure 5, the rare earth materials show higher remanence and coercive field than Ferrites and hence the rare earth materials support better the demagnetization effects commented above. In applications where the demagnetization is not going to be a problem, the AlNiCo or Ferrites materials can be used since they exhibit smaller coercive field strength. The magnet properties and the application, where the permanent magnet is going to be used, have to be taken into account since better properties of the magnet will increase the price. The B_M-H_M loop gives an idea of the amount of the hysteresis losses that a permanent magnet has. The area of the loop is proportional to the amount of losses. For example an NdFeB magnet presents more Foucault losses than a Ferrite material.

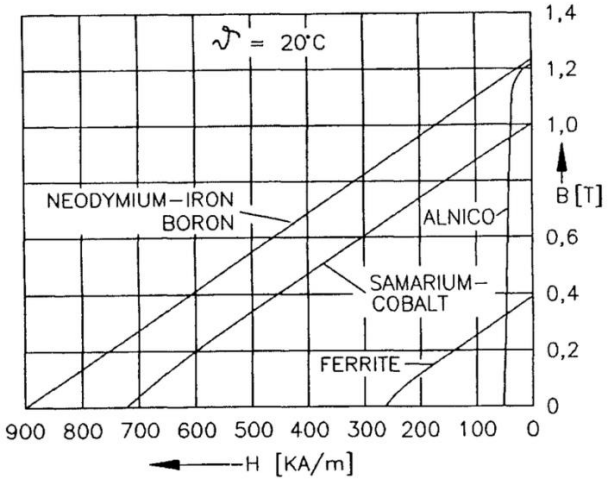

Figure 5: Remanence and coercivity properties comparison between four permanent magnets at 20° [14].

Once the technical design is done, another problem that can cause demagnetization is the sudden short-circuit. When the stator windings have a sudden short-circuit, they induce a strong magnetic field, which acts strongly against the magnetic flux of the permanent magnet. So when a simulation of the machine in a FE analysis is carried out, a test of a sudden short-circuit should be done to see how much percentage of the area of the permanent magnet will suffer irreversible demagnetization by the high field strength for a given temperature.
The sudden short-circuit test is done at no-load condition when the three-phase stator terminals, which are open, suddenly close at the same time and with the same connection point. The worst case is when the voltage phase is crossing the 0 V, which cause maximum DC current, to twice the value of the AC amplitude [18]. This high current induces a strong magnetic flux that acts against the magnetic flux of the permanent magnet, causing irreversible demagnetization. The current of a three-phase short-circuit can be calculated as:

$$\hat{I}_{\mathrm{k}} = \frac{2 \cdot \sqrt{2} \cdot U_{\mathrm{p,0}}}{\sqrt{R_{\mathrm{s}}^2 + (\omega \cdot L_{\mathrm{k}})^2}} \tag{2.3-3}$$

where $U_{\mathrm{p,0}}$ is the induced voltage at no-load condition, R_{s} is the stator phase resistance, ω is the angular speed and L_{k} is the inductance of the short-circuit.

2.4. Stator windings design

2.4.1. Concentrated and distributed windings

The synchronous machines (SM) can be built with two different stator winding methods, distributed or concentrated. Both methods will depend on the combination of the number of the slots and poles and each winding has each advantages and disadvantages. For the SM built with concentrated windings, they have shorter end coils, which reduce the total ohmic losses, the length and the weight of the machine. In addition the torque density increases due to a greater fill factor. On the other hand, the machines with distributed windings can achieve higher efficiencies and this configuration has less eddy current losses in the permanent magnets at high speeds [19] [20].

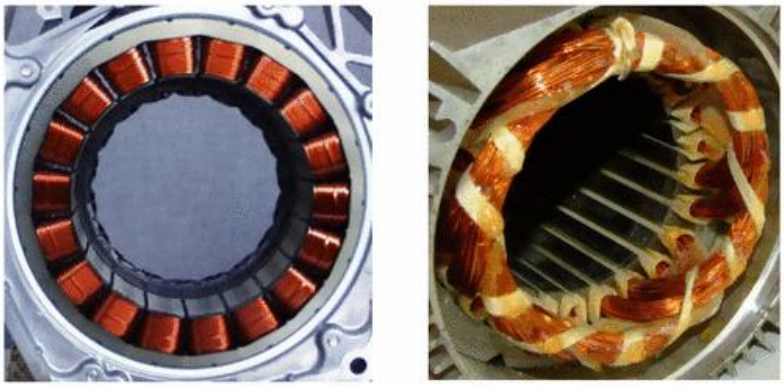

Figure 6: Stator windings with a concentrated stator winding (left) and a distributed stator winding (right) [21].

A comparison made with a concentrated and a distributed winding IPMSM, working at the nominal operation point and at the high speed operational point, shows that the IPMSM with a distributed stator winding produces more torque due to higher reluctance torque since there is a greater salient ratio (L_q/L_d). Although the distributed winding arrangement has significantly higher copper losses, the efficiency is a little bit higher than concentrated winding IPMSM due to the high magnetic eddy current losses. These eddy current losses are caused by the large harmonic content in the back-mmf distribution, that concentrated winding has [19].
At the end the selection of a concentrated or a distributed stator winding depends of the need of the machine. If a high speed operation is needed, a distributed winding would be suitable due to less eddy current losses, higher torque production and higher efficiency. If the challenge is to have short end coils and the reduction of copper losses or having a compact machine, the concentrated winding arrangement would be a beneficial solution.

2.4.2. One and two layer windings

The winding of an electrical machine can be called integer slot winding or fractional slot winding depending on the number of slots per pole and phase q of the machine. If q is an integer number, it refers to an integer slot winding, if q is a fractional number, it is called fractional slot winding. Both cases can have concentrated or distributed windings, as well as an arrangement in a one-layer or two layer windings. Having two-layer winding means that in each slot, coils of different phases are arranged in two layers, so the coils can be pitched, meaning that the coils span W can be smaller than the pole pitch τ_p. As literature shows in [22] [23], having more than one-layer is useful in order to reduce harmonic components due to an elimination of harmonic components in the air-gap flux, which improves the winding factor and reduces the harmonic losses. In addition, it can significantly reduce torque ripple,

vibrations and noise since there is better balance of magnetic forces, as it has been demonstrated in [24]. On the other hand, having more than one-layer winding and a shorter coil span than a pole pitch, means that a pitching factor k_p is introduced and it decreases the flux linkage, which is proportional to torque production.

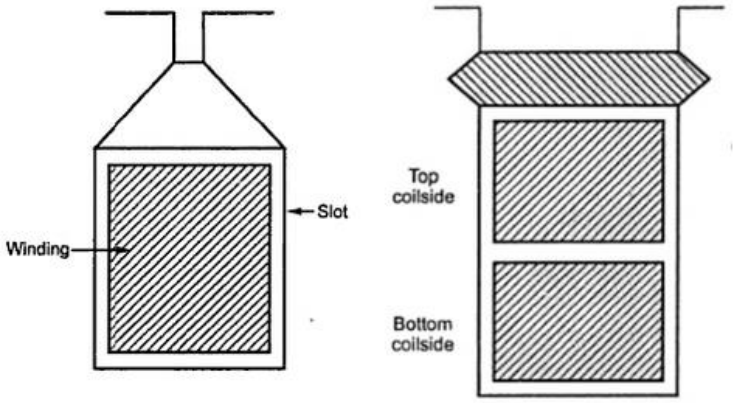

Figure 7: Two slots of a stator with one layer winding (left) and two layers winding (right) [25].

2.4.3. Arrangement of the stator winding

When the coils are arranged in the stator, a symmetrical placement of the coils should be made not to have unwanted forces at load condition. The forces in a symmetrical placement can cancel each other; otherwise they can produce more electromagnetic forces in the radial direction which contributes to vibration, noise and a reduction of the lifetime of the machine.

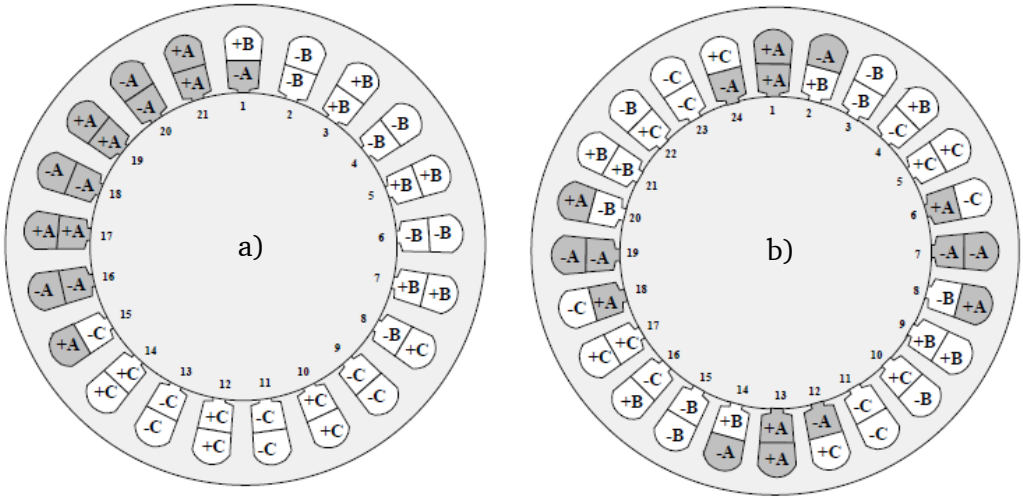

Figure 8: The winding arrangements of two machines with fractional slot and two layer windning. a) unsymmetrical winding distribution, b) symmetrical winding distribution [15].

Figure 8 shows, at one time, phase A with a peak current of $+\hat{\imath}$ and phases B and C having a peak current of $-1/2\hat{\imath}$. In that situation, magnetic forces are generated. In the case of Figure 8 a), the unsymmetrical phase distribution causes the forces to act only in one side of the stator causing a magnetic pull effect. In the case of Figure 8 b) the symmetrical phase distribution causes the magnetic forces to cancel each other and thus the stator is not theoretically affected by them. For this reason, the symmetrical distribution of the stator windings should be considered. Furthermore, different researches agree that the designer should consider choosing a fractional number of slots per pole and phase when a machine is designed with distributed and two-layer windings to compensate the unbalanced pull effect [15] [26].

2.4.4. Calculation of integer and fractional distributed winding

The distribution of the phase windings through the stator slots can be achieved either by integer or fractional slot windings. Some formulas and definitions are needed to illustrate the vector distribution of the phases. In addition, a vector diagram of the slot voltage can be built to get the individual voltage of each phase. The literature shows, that for each case of winding configurations, the formulas and definitions can vary. Literature [1] shows how to calculate an integer or fractional distributed winding; also [15] demonstrates how to build a vector distribution and a voltage vector diagram for fractional slot windings and for the particular case of a concentrated winding configuration.
Later, in this thesis, it will deal with integer and fractional slot distributed winding. For that, this section shows how to build the vector distribution of the phases and the diagram of the slot voltage for the cases of integer and fractional slot distributed windings.

2.4.4.1 – Integer slot distributed winding

The basic parameters of the machine that are needed for the following calculation, are the number of stator slots Q, the number of phases of the machine m, the number of pole pairs p, and the number of slots per pole per phase q:

$$Q = 2 \cdot m \cdot p \cdot q \tag{2.4-1}$$

The first thing that is required is the distribution of the slots into the phases, thus the sequence of the slots for the phases is achieved. For example; a machine with $p = 1$, $m = 3$ and $Q = 12$; has the number of slots per pole and phase $q = 2$, giving a sequence of U+, U+, W-, W-, V+, V+, U-, U-, W+, W+, V-, V-. The sequence is drawn as a phasor diagram with the angle between two phasors of adjacent slots like:

$$\alpha_u = \frac{360 \cdot p}{Q} \tag{2.4-2}$$

Finally the distance between two wound slots is required or in other words, the distance in slots from the positive site of the coil to the negative site of it:

$$y_Q = \frac{Q}{2p} \tag{2.4-3}$$

For the previous example, α_u is 30° and y_Q is 6. Thus the phasor diagram and the voltage diagram are drawn as:

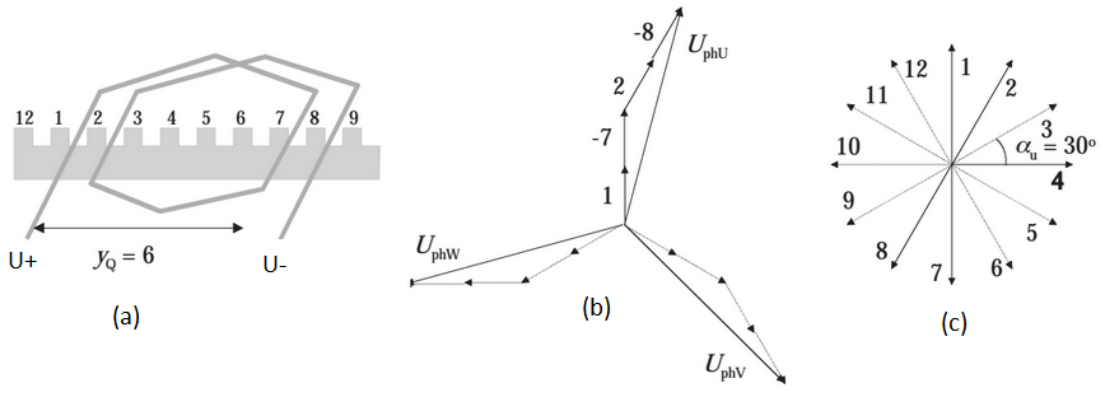

Figure 9: Integer slot winding distribution. (a) Slot distance between the positive and negative sites of one coil; (b) Voltage diagram for each phase (*U*, *V*, and *W*); (c) Phasor diagram of the slots [1].

2.4.4.2 – Fractional slot distributed winding

The calculation of fractional slot machines is separated into two groups, the 1st-grade and the 2nd-grade windings. In order to know which group should be chosen, the equation 2.4-1 is needed in this case and rewritten as the equation 2.4-4:

$$q = \frac{Q}{2 \cdot p \cdot m} = \frac{z}{n} \tag{2.4-4}$$

where z and n are the numerator and the denominator of q respectively, reduced to the lowest terms. The values of z and n indicate if the calculation will be done with respect to the 1st-grade or the 2nd-grade group. For the first one, the number of layers does not matter, whereas for the second group there are two possibilities, when the winding has one-layer or two-layers in the slots. When the denominator n is an odd number the calculations will be done for a 1st-grade winding and if n is even the winding is a 2nd-grade. The parameters for the design of a fractional slot winding are in Table 1.

Table 1: Winding definitions for fractional slot machines [15].

	1st-grade	2nd-grade	2nd-grade
denominator, n	odd	even	even
T	p/n	$2p/n$	$2p/n$
layer	one or two	one	two
Q^*	Q/t	$2Q/t$	Q/t
p^*	n	n	$n/2$
t^*	1	2	1

where t is the number of the electrically equal slot sequences or how many times the phasor diagram will be repeated, Q^* is the number of vectors per on cycle that the diagram has, p^* is the number of poles in a base diagram and t^* is the number of base diagrams in a stator winding.
In order to build the vector diagram of the phases, two more concepts have to be introduced; the distance between two adjacent slots α_u and the distance between two slots α_z:

$$\alpha_u = \frac{360 \cdot p^*}{Q^*} \tag{2.4-5}$$

$$\alpha_z = \frac{360 \cdot t^*}{Q^*} \tag{2.4-6}$$

When the calculations are done, the phasor diagram, which distributes the coils around the stator slots for a fractional slot winding, can be drawn.

2.4.5. Winding factor

Having the windings in a distributed configuration makes the magnetic voltage distribution more sinusoidal, although this configuration introduces the distributed factor k_d, which reduces the total induced voltage on each phase. This factor reduces also the higher harmonics due to $q > 1$ and some coils per pole and phase are connected in series [3].

The configuration of the windings is important as some factors appear. The pitch factor k_p and the distribution factor k_d will determine the winding factor k_w and all of them have their amplitude for each harmonic component. The fundamental amplitude value of these factors should be as high as possible to increase the flux linkage and therefore the induced voltage. The amplitude of the harmonic components should be as low as possible to reduce unwanted forces and additional losses caused from them.

$$k_\mathrm{w} = k_\mathrm{p} \cdot k_\mathrm{d} \tag{2.4-7}$$

The pitch and distribution factors are deduced from the *Fourier* series and in both cases there are differences results depend on integer or fractional slot windings. The periodic function $V(\gamma)$ witch period 2π can be described as equation 2.4-8 from [13]:

$$V(\gamma) = V_0 + \sum_{\nu=1,2,3\ldots}^{\infty} \left[\hat{V}_{\nu,\mathrm{a}} \cdot \cos(\nu \cdot \gamma) + \hat{V}_{\nu,\mathrm{b}} \cdot \sin(\nu \cdot \gamma)\right] \tag{2.4-8}$$

The individual amplitudes of ordinal number for each harmonic $\nu = 1, 2, 3\ldots$ are calculated:

$$\hat{V}_{\nu,\mathrm{a}} = \frac{1}{\pi}\int_0^{2\pi} V(\gamma) \cdot \cos(\nu \cdot \gamma) \cdot d\gamma \qquad \hat{V}_{\nu,\mathrm{b}} = \frac{1}{\pi}\int_0^{2\pi} V(\gamma) \cdot \sin(\nu \cdot \gamma) \cdot d\gamma \tag{2.4-9}$$

and the average value is calculated using:

$$\hat{V}_0 = \frac{1}{2\pi}\int_0^{2\pi} V(\gamma) \cdot d\gamma \tag{2.4-10}$$

The circumferential angle γ is expressed by the circumferential coordinate x and the pole pitch τ_p:

$$\gamma = x\frac{\pi}{\tau_\mathrm{p}} \tag{2.4-11}$$

If a *Fourier* analysis of the magnetic voltage per phase of a three-phase winding supplied by a symmetrical three-phase system is carried out, the result will be such that the multiple numbers of the 3$^{\mathrm{rd}}$ harmonic component will not appear since the three positive-sequences and negative-sequences of the rotating waves cancel each other. Furthermore, using the *Fourier* series, the pitch factor and the distribution factor can be calculated for a given integer or fractional slot winding.

2.4.5.1 – Integer slot distributed winding (pitch and distribution factors)

If a *Fourier* analysis of a function like in Figure 10 is carried out and the circumferential angle γ is set to 0, an even function is generated. The result of the *Fourier* analysis gives the value of the magnetic voltage for each ordinal number:

$$\hat{V}_{\mathrm{c},\nu=1,5,7} = \frac{2}{\pi}\int_0^{\pi} V_\mathrm{c}(\gamma) \cdot \cos(\nu \cdot \gamma) \cdot d\gamma = \frac{\Theta_\mathrm{Q}}{2} \cdot \frac{4}{\nu\pi} \cdot \sin\left(\frac{\nu\pi}{2}\right) \tag{2.4-12}$$

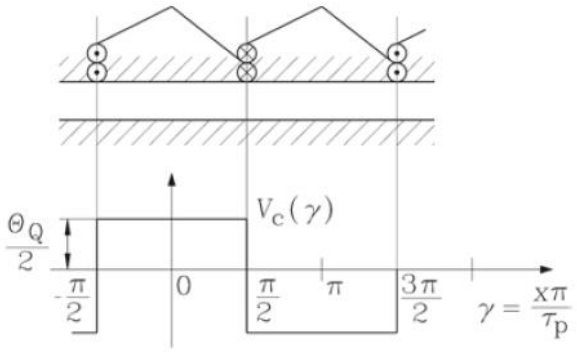

Figure 10: Magnetic voltage calculation from a fully-pitched stator slots winding distribution [13].

An even function means that only cosine-functions are contained in the *Fourier*-sum. In addition the function is symmetrical to the abscissa which makes that the even ordinal numbers are removed.
In case of a short pitched coil like in Figure 11, the pitch factor will be deduced from the *Fourier* calculation of the magnetic voltage as in equation 2.4-13:

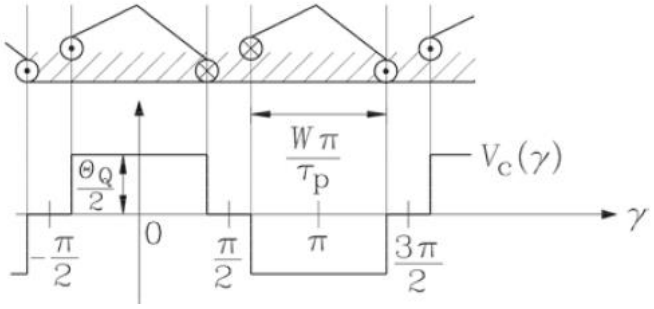

Figure 11: Magnetic voltage calculation from a short-pitched stator slots winding distribution [13].

$$\hat{V}_{c,\nu=1,5,7} = \frac{\Theta_Q}{\pi}\int_0^{\pi\cdot W/(2\tau_p)} (\cos(\nu\cdot\gamma) - \cos(\nu\cdot\gamma + \nu\pi/2))\cdot d\gamma = \frac{\Theta_Q}{2}\cdot\frac{4}{\nu\pi}\cdot\sin\left(\frac{W}{\tau_p}\cdot\frac{\nu\pi}{2}\right) \qquad (2.4\text{-}13)$$

When the winding configuration is set up as group of coils $q > 1$, the distribution factor appears as in equation 2.4-14:

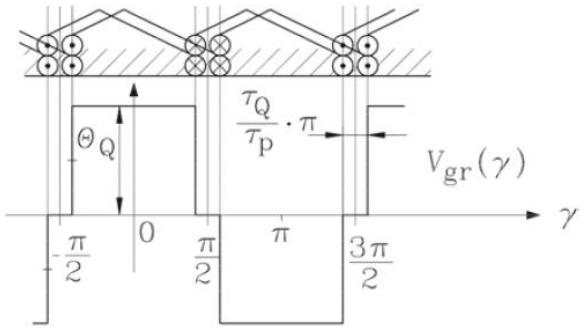

Figure 12: Magnetic voltage calculation from a fully-pitched stator slots winding distribution with group of coils $q = 2$ [13].

$$\hat{V}_{\mathrm{gr},\nu=1,5,7} = \frac{2}{\pi}\int_0^{\pi} V_{\mathrm{gr}}(\gamma)\cdot\cos(\nu\cdot\gamma)\cdot d\gamma = \frac{q\Theta_{\mathrm{Q}}}{2}\cdot\frac{4}{\nu\pi}\cdot\sin\left(\frac{\nu\pi}{2}\right)\cdot\frac{\sin\left(\frac{\nu\pi}{2m}\right)}{q\cdot\sin\left(\frac{\nu\pi}{2mq}\right)} \tag{2.4-14}$$

In case of a three phases machine with a winding configuration with $q = 2$ and a short pitch of $W/\tau_{\mathrm{p}} = 5/6$, the pitch, distribution and winding factors can be calculated for each harmonic. The harmonic orders ν are deduced from $\nu = 1 + 2m\cdot g$ since the configuration is for integer slot winding, where $g = 0, \pm1, \pm2, \pm3, \ldots$ As it can be seen in Table 2, the winding factor calculated from the pitch and distributed factors for each harmonic will give a reduction in the amplitudes of each harmonic component. For the fundamental component, the magnetic voltage will be almost 7 % reduced, although harmonics such as the 5$^{\mathrm{th}}$ or the 7$^{\mathrm{th}}$ will be almost 100 % reduced.

Table 2: Winding factor calculation for a fully-pitched group of coils $q = 2$.

harmonic order, ν	$k_{\mathrm{p},\nu}$	$k_{\mathrm{d},\nu}$	$k_{\mathrm{w},\nu}$
1	0.966	0.966	0.933
-5	0.259	0.259	0.067
7	0.259	0.259	0.067
-11	0.966	0.966	0.933
13	0.966	0.966	0.933
-17	0.259	0.259	0.067

2.4.5.2 – Fractional slot distributed winding (pitch and distribution factors)

For the case of a fractional slot distributed winding, the expressions of pitch and distribution factors also can be analysed from the *Fourier* series [13].
The pitch factor $k_{\mathrm{p},\nu}$ results to be the same like in the case on integer slot winding:

$$k_{\mathrm{p},\nu} = \sin\left(\frac{\nu\cdot W}{\tau_p}\cdot\frac{\pi}{2}\right) \tag{2.4-15}$$

The distribution factor $k_{\mathrm{d},\nu}$ results to be a complicated equation 2.4-16, which needs some explanations of its terms:

$$k_{\mathrm{d},\nu} = \frac{\sin(\nu\cdot\alpha_{\mathrm{u}}\cdot Y\cdot q_1/2) - \cos(\nu\cdot p^*\cdot\pi\cdot Y)\cdot\sin(\nu\cdot\alpha_{\mathrm{u}}\cdot Y\cdot q_2/2)}{(q_1+q_2)\cdot\sin(\nu\cdot\alpha_{\mathrm{u}}\cdot Y/2)} \tag{2.4-16}$$

The coefficients q_1 and q_2 are calculated depending on the number of the stator slots of one basic phasor diagram Q^*:

$$Q^* \text{ is even} \rightarrow q_1 = q_2 = \frac{Q^*}{2m} \tag{2.4-17}$$

$$Q^* \text{ is odd} \rightarrow q_1 = q_2 + 1 = \frac{Q^* + m}{2m} \tag{2.4-18}$$

The parameter Y will be calculated with $Q^*$and p^*, which have been explained in Table 1. The $g_{\min}$ is an integer number and it is the minimum value that makes the Y parameter also integer:

$$Y = \frac{g_{\min} \cdot Q^* + 1}{p^*} \tag{2.4-19}$$

Also the angle between two slots is needed for the calculation of the distribution factor:

$$\alpha_{\mathrm{u}} = \frac{360 \cdot p^*}{Q^*} \tag{2.4-20}$$

An examples of fractional slot winding is carried out to calculate the pitch, distribution and winding factors. The examples is for $q = 3/2 = 1.5$. The harmonic orders are calculated for a fractional slot winding model with the denominator n as even number, with the expresion $\nu = (2/n) \cdot (1 + m \cdot g)$, where $g = 0, \pm 1, \pm 2, \pm 3, \ldots$

Table 3: Winding factor calculation for a fractional slot winding $q = 1.5$ with $W/\tau_{\mathrm{p}} = 4/4.5$.

harmonic order, ν	$k_{\mathrm{p},\nu}$	$k_{\mathrm{d},\nu}$	$k_{\mathrm{w},\nu}$
1	0.9848	0.9567	0.9452
-2	0.3420	0.1774	0.0607
4	0.6428	0.2176	0.1398
-5	0.6428	0.2176	0.1398
7	0.3420	0.1774	0.0607
-8	0.9848	0.9567	0.9452
10	0.9848	0.9567	0.9452
-11	0.3420	0.1774	0.0607
13	0.6428	0.2176	0.1398
-14	0.6428	0.2176	0.1398
16	0.3420	0.1774	0.0607

2.5. Maxwell stress tensor for cogging torque and radial pressure calculation

There are several methods to calculate the electromagnetic forces such as the *Maxwell* stress tensor, the Coenergy method or the *Lorentz* Force theorem [14]. The choice of method used will depend of the problem. In this thesis, the *Maxwell* stress tensor is going to be used to calculate the electromagnetic forces in the air-gap of the motor. This method calculates the electromagnetic force, using the magnetic flux density distribution along a circumferential coordinate x, in this case the air-gap. From the *Lorentz* Force law $\vec{F} = q(\vec{E} + \vec{v} \times \vec{B})$ and using the four *Maxwell* equations, the total force that the electromagnetic field produces in a surface is given by equation 2.5-1, [14]:

$$\vec{F} = \iint \left[\frac{1}{\mu_0} \vec{B}(\vec{B} \cdot \vec{n}) - \frac{1}{2\mu_0} \vec{B}^2 \vec{n} \right] dS \tag{2.5-1}$$

where $\vec{n}$ is the normal vector to the surface S and $\vec{B}$ is the magnetic flux density. The electromagnetic force has two force components, the radial and the tangential forces expressed in equations 2.5-2 and 2.6-3 respectively:

$$F_{\mathrm{r}} = \frac{l_{\mathrm{Fe}}}{2\mu_0} \int [B_{\mathrm{r}}^2 - B_{\mathrm{t}}^2] dx \tag{2.5-2}$$

$$F_{\mathrm{t}} = \frac{l_{\mathrm{Fe}}}{\mu_0} \int [B_{\mathrm{r}} B_{\mathrm{t}}] dx \tag{2.5-3}$$

where l_{Fe} is the iron stack length, B_{r} is the normal or radial component of the magnetic flux density in the air-gap and B_{t} is the tangential component of the magnetic flux density in the air-gap.
The torque is calculated by multiplying the tangential force of the magnetic flux density 2.5-3 and for the radius where the *Maxwell* stress tensor is applied. In this case, it is applied in the middle of the air-gap with a radius r. If the radial and tangential components of the magnetic flux are chosen for the no-load condition, the cogging torque will be calculated. Furthermore, the torque can be expressed with the circumferential angle γ, since $x = \gamma \cdot r$, as equation 2.5-4:

$$M = \frac{l_{\mathrm{Fe}}}{\mu_0} r^2 \int_0^{2\pi} [B_{\mathrm{r}}(\gamma) B_{\mathrm{t}}(\gamma)] d\gamma \tag{2.5-4}$$

It has been demonstrated that the electromagnetic forces are the main sources of vibration and acoustic noise in electrical motors. Since cogging torque and torque ripple are electromagnetic forces, the reduction of both parameters will improve the reduction of vibration and noise of the motor [7]. When *Maxwell* stress tensor is applied to the air-gap, the radial electromagnetic force F_{r} can be calculated, which is the main component that makes the stator core vibrates. Therefore, the radial pressure caused by the radial electromagnetic force acting on the structure per unit area is given by 2.5-5:

$$p_{\mathrm{r}}(\gamma, t) \approx \frac{F_{\mathrm{r}}}{l_{\mathrm{Fe}} x} = \frac{[B_{\mathrm{r}}^2(\gamma, t) - B_{\mathrm{t}}^2(\gamma, t)]}{2\mu_0} \tag{2.5-5}$$

In equation 2.5-5 the tangential component of the magnetic flux density can be neglected due to the magnetic flux lines are nearly perpendicular to the stator and rotor cores.

2.6. Cogging torque

The cogging torque, which appears at no-load condition of the machine, is generated due to the interaction between the field of permanent magnets and the stator slots. The field of permanent magnets generates a tangential force on the stator teeth, as can be seen in Figure 13. This force tries to find an equilibrium position since there are slots and teeth on the stator, causing a variation of the reluctance, which produces a periodicity of the cogging torque [8]. A simplified equation of cogging torque is given in 2.6-1, where Φ_δ is the magnetic flux crossing the air-gap, $\mathcal{R}$ is the reluctance through which the flux passes and γ is the circumferential angle or rotor position [27].

$$M_{\text{cog}} = \frac{1}{2} \cdot \Phi_\delta^2 \cdot \frac{d\mathcal{R}}{d\gamma} \tag{2.6-1}$$

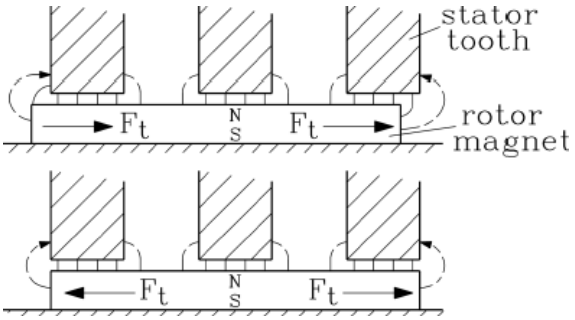

Figure 13: Interaction of the magnetic field of the permanent magnets with the stator teeth [3].

Cogging torque produces zero net-work and it should be mitigated to cause fewer disturbances on the electromagnetic torque. The percentage of cogging torque can be calculated with the maximum and minimum cogging torque values and the nominal torque M_{N} as [3]:

$$\widehat{w}_{\text{M}} = \frac{\widehat{M}_{\text{cog}}}{M_{\text{N}}} \cong \frac{(M_{\text{max}} - M_{\text{min}})/2}{(M_{\text{max}} + M_{\text{min}})/2} \cdot 100 \tag{2.6-2}$$

The periodicity of the cogging torque N_{period} during a rotation of a slot pitch τ_{Q} can be calculated with equation 2.6-3 since it depends on the number of stator slots and poles [28]. With this expression, a comparison of the periodicity of the cogging torque between two motors can be achieved,

$$N_{\text{period}} = \frac{2p}{\text{GCD}\,\{Q, 2p\}} \tag{2.6-3}$$

where Q is the number of stator slots and p the number of pole pairs.

When the values of N_{period} are low, it means that the positive and negative elementary torques happen at the same time. Both waves superimpose onto each other giving a high cogging torque. So in the case of higher N_{period} the amplitude of cogging torque will be lower. Furthermore, it has been studied that a higher GCD increases the cogging torque amplitude and at the same time increases the radial forces since they are not well balanced and that increases the electromagnetic noise produced for the motor [24]. So the designer has to decide on a compromise between the number of stator slots and the rotor poles.

The mechanical angle corresponding to each cogging torque period, which could mitigate the cogging torque, is a skew angle γ_{skew} given by [28]:

$$\gamma_{\text{skew}} = \frac{2\pi}{N_{\text{period}} \cdot Q} \tag{2.6-4}$$

2.7. Torque ripple

The torque ripple appears in the load condition and it is undesirable due to cause vibration in the load response. The three main contributions to torque ripple are the electromagnetic torque which generates the work torque, the reluctance torque which appears due to the saliency and the cogging torque. The first contribution is caused by the distortion of the magnetic flux density distribution in the air-gap or the distortion in the stator current. The second contribution is more notable in machines which have higher saliency ratio and it further explains why the IPMSM can show more cogging torque and torque ripple than SPMSM. The third contribution arises from the interaction between the magnetic field of permanent magnets and the slotted iron stator structure [11].

The torque ripple can be defined as a percentage of the average torque:

$$\widehat{w}_{\text{M}} = \frac{\widehat{M}_{\text{rip}}}{M_{\text{av}}} \cong \frac{(M_{\text{max}} - M_{\text{min}})/2}{(M_{\text{max}} + M_{\text{min}})/2} \cdot 100 \tag{2.7-1}$$

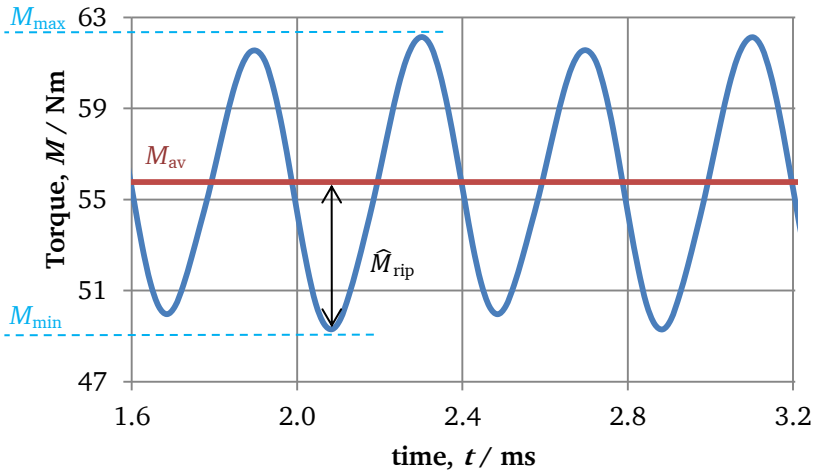

Figure 14: Calculation of the torque ripple from a time-graph at load condition.

2.8. Minimization of cogging torque and torque ripple

The cogging torque and torque ripple can be minimized by two different ways. The first one is related with improvements in the geometry of motor and the second one is related with control technics of the motor. This thesis will focus in geometric parameters since a proper design of the machine will smoothen the cogging torque and the torque ripple. Geometric parameters can be improved such as, skewing the rotor or stator, variation of slot opening, especial shapes of slots, a proper slot-pole number combination, using fractional slot windings, designs with odd number of slots per pole and phase, variation of the magnet width, magnets mounted in V-shape configurations, pole-arc to pole-pitch ratio optimization, creating flux barriers in the rotor or slotless configurations.
Next, some of the most relevant design methods and the ones that are going to be used in the simulation analysis are explained.

2.8.1. Steeped and skewed rotor

Steeping and skewing the rotor are probably the most effective design methods to reduce the cogging torque. However, the manufacturing cost and time of this method is high. For a rotor of an asynchronous machine or a SPMSM, skewing of the rotor is a common technique; on the other hand for an IPMSM the rotor has to be step-skewed since the magnets are placed inside of the rotor [9]. In order to eliminate the cogging toque the skew angle γ_{skew} 2.6-3 should be equal to the period of the fundamental spatial harmonic of the cogging torque. Skewing either the rotor or the stator can improve the back-emf waveform, although it can produce more stray losses and increases the leakage inductance [9]. Skewing the stator reduces the effective slot area, increases the conductor length and the winding installation becomes more complicated [29].

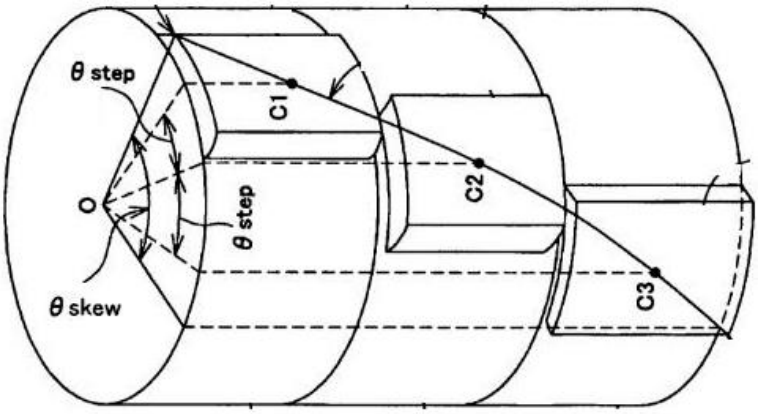

Figure 15: Step-skewed rotor in three steps (C1, C2, and C3) [30].

2.8.2. Shape of stator slots and slot opening

It was demonstrated that the smaller the slot opening, the less harmonic components appear in the back-emf and the cogging torque is reduced. In addition, it has been proven that a significant reduction of slot opening causes an increment of L_{d}, which reduces the saliency ratio and the reluctance torque [9].
If the number of notches per stator tooth is introduced like in Figure 16 (a), some harmonics can be cancelled, reducing the amplitude of the cogging torque. On the other hand, this method produces more reluctance variation due to the notches, which contributes to a greater cogging torque fundamental frequency [9].

Closed slots like in Figure 16 (c) can be a great solution since there is a better flux path through the stator teeth, however not all winding configurations allow for closed stator slots [14]. Building empty teeth like in Figure 16 (b) between slots will produce an increment of cogging torque if the opening of the slots is too big. Furthermore, it will produce an unacceptable increasing in the slot leakage and a high saturation due to the thickness of the bridge.

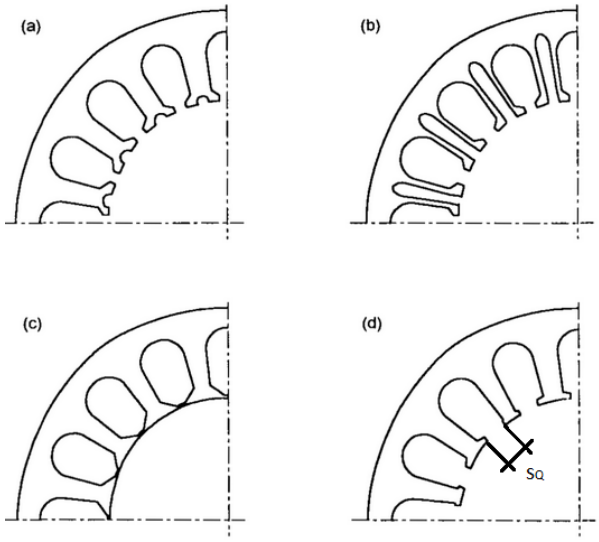

Figure 16: Different stator slots shapes for the minimization of the cogging torque: (a) notched teeth, (b) empty teeth, (c) closed slots, (d) teeth with different width on the active surface [14].

2.8.3. Pole-arc to pole-pitch ratio optimization

It has been proved that a suitable pole-arc to pole-pitch ratio reduces the cogging torque [31]. However, the same ratio may not be the appropriated one for reducing the torque ripple. Furthermore, the same ratio can reduces cogging torque and increase the torque ripple. This technique is applicable in SPMSM as well as in IPMSM [31]. In IPMSM with V-shape configuration, the pole arc can be achieved with the magnet length variation or changing the angle between magnets α_M. The variation of this angle is important because the pole-arc can be varied without changing the total amount of magnetic material, which contributes to build the magnetic flux density in the air-gap. This method is very economic and there are no increments in cost or time manufacturing process.

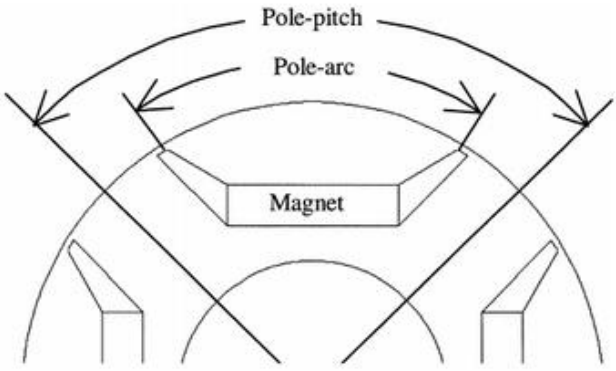

Figure 17: Pole-pitch to pole-arc coefficient in IPMSM for the reduction of cogging torque [31].

2.8.4. Slotless construction

Since the cogging torque is generated by the interaction between the magnetic field from the rotor and the stator slots, the slotless stator configuration contributes to reduce the cogging torque.

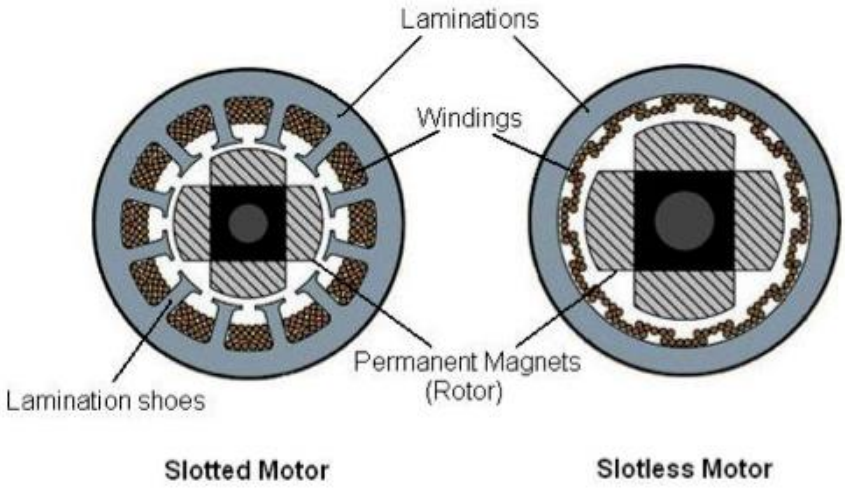

Figure 18: Two brushless motors with a slotted configuration (left) and a slotless configuration (right) [32].

This configuration can be suitable adopted for application where the motor has to be very small and there is no space for winding the coils around stator slots. Furthermore, not having stator slots makes the design more compact, more lightweight, produces a reduction of the iron losses through the stator iron structure and it can be achieved a better cooling for windings due to the large air-gap [33]. Having a large air-gap in slotless structures makes the reluctance in the air-gap higher and it reduces the magnetic flux, which will report a reduction of the electromagnetic torque in comparison with an IPMSM [12]. In order to increase the magnetic flux, larger amount of rare earth magnets should be used making an expensive construction and taking the risk of stator saturation. Furthermore, the armature inductance decreases causing an increment of the losses in case of PWM control and decrements the difference between L_q and L_d, thus few reluctance torque is generated.

2.8.5. Fractional number of stator slots per pole and phase

The fact that choosing a configuration of the machine with a fractional number of stator slots per pole and phase means that the stator teeth and the rotor poles are not fully aligned with each other and this produces a partial cancellation of harmonics. Thus, the cogging torque amplitude decreases at the same time whereas the frequency increases [34]. At the same time when some harmonics cancel each other for a fractional slot winding machine, the magnetic flux distribution wave is not symmetrical to the x-axis anymore and that will make that even harmonics appear in the magnetic flux distribution. Those harmonics cause more oscillations, which can increase the torque ripple and the vibrations of the machine contributing to sound and electromagnetic noise [3].
When the selection of the fractional slot winding number q is done, it could be a coincidence that the number of the stator slots Q is an odd number, since $Q = 2 \cdot p \cdot m \cdot q$. In that case if the design of a machine is made with an odd number of stator slots, each magnet sees a fractional number of slots and the magnetic field that contributes to the generation of cogging torque is placed out of phase [34], [35]. Thus, the overall cogging torque can be reduced since several harmonics cancel each other.

The fact that using fractional number of stator slots per pole and phase, causes that the main harmonic orders of the magnetic flux from the rotor that contributes to generate cogging torque, are higher in fractional slot winding machines than in integer slot winding machines. Thus, the amplitude of these harmonics will be lower, giving a reduction of cogging torque. The explanation of that phenomenon can be deduced since $M_{\mathrm{cog}} \sim B_1 \cdot B_\mu \cdot \lambda_l$, where the magnetic flux of the rotor for a harmonic number B_μ is inversely proportional to the rotor harmonic order μ and the value of the permeance λ_l is also inversely proportional to the parameter l. Hence, using fractional slot windings is the main reason of this thesis to reduce the cogging torque.
In order to calculate the harmonic components which cause cogging torque, an analytical calculation can be done from the electromagnetic torque equation that the machine produces [13]:

$$M_{\mathrm{e},\nu,\mu} = \frac{d_{\mathrm{si}}^2 \cdot l_{\mathrm{Fe}}}{4} \cdot \int_0^{2\pi} \hat{A}_\nu \cdot \sin(\nu p \cdot \gamma_{\mathrm{m}} - \omega_\nu t) \cdot \hat{B}_\mu \cdot \cos(\mu p \cdot \gamma_{\mathrm{m}} - \omega_\mu t) \cdot d\gamma_{\mathrm{m}} \tag{2.8-1}$$

From equation 2.8-1 the cogging torque can be deduced if the current loading component at load condition $\hat{A}_\nu$ is changed with the equivalent current loading components at no-load condition. The equivalent current loading is deduced from the radial component of the magnetic flux density of the air-gap B_δ that appears in the stator slots.
At no-load condition, B_δ is function of the radial component of the magnetic flux from the permanent magnets B_{r} and the permeance coefficient λ, which takes into account the *Carter´*s coefficient k_{C} for the slot opening effect. All the parameters are expressed by the circumferential mechanical angle $\gamma_{\mathrm{m}} = (\pi \cdot x)/(p \cdot \tau_{\mathrm{p}})$.

$$B_\delta(\gamma_{\mathrm{m}}) = B_{\mathrm{M}}(\gamma_{\mathrm{m}}) \cdot \lambda(\gamma_{\mathrm{m}}) \tag{2.8-2}$$

If the expressions of the magnetic flux from the permanent magnets and the permeance coefficient from [13] are replaced in the equation 2.8-2, the resulting air-gap magnetic flux density due to the sum of the harmonic components is:

$$B_\delta(\gamma_{\mathrm{m}}) = \sum_{\mu=1,3,5\ldots}^{\infty} \hat{B}_\mu \cdot \cos\big(\mu p(\gamma_{\mathrm{m}} - \Omega_{\mathrm{m}} t)\big) \cdot \left(\frac{1}{k_{\mathrm{C}}} + \sum_{l=1,2\ldots}^{\infty} \lambda_l \cdot \cos(l \cdot Q \cdot \gamma_{\mathrm{m}})\right) \tag{2.8-3}$$

where $\hat{B}_\mu$ is the peak value of the magnetic flux for a rotor harmonic μ, Ω_{m} is the mechanical angular speed, l is an integer number (1, 2, 3…) and Q is the number of stator slots. When the equation 2.8-3 is reorganized and considered for the fundamental component $\hat{B}_1$, the slotting effect part of the magnetic flux density can be calculated as:

$$B_\sim(\gamma_{\mathrm{m}}) = \frac{\hat{B}_1}{2} \cdot \sum_{l=1,2\ldots}^{\infty} \lambda_l \cdot \cos(\gamma_{\mathrm{m}}(p + Q \cdot l) - p\Omega_{\mathrm{m}} t) + \frac{\hat{B}_1}{2} \cdot \sum_{l=1,2\ldots}^{\infty} \lambda_l \cdot \cos(\gamma_{\mathrm{m}}(p - Q \cdot l) - p\Omega_{\mathrm{m}} t) \tag{2.8-4}$$

The slotting effect part of the magnetic flux density $B_\sim(\gamma_{\mathrm{m}})$ can be used to obtain the equivalent current loading components at no-load condition, by using the method of the equivalent current loading. The equivalent current loading will be the superposition of two components $A_{l+}(\gamma_{\mathrm{m}})$ and $A_{l-}(\gamma_{\mathrm{m}})$. These two components are derived from $B_\sim(\gamma_{\mathrm{m}})$ since the magnetomotive force (mmf) can be deduced from the magnetic flux density as $B_\delta = \mu_0 \cdot V/\delta$ and the current loading is hence $A(x) = dV/dx$. Thus, the two components of the current loading that derives from $B_\sim(\gamma_{\mathrm{m}})$ are:

$$A_{l+}(\gamma_{\mathrm{m}}) = -\frac{\delta \cdot \hat{B}_1 \cdot \pi}{2 \cdot \mu_0 \cdot p \cdot \tau_{\mathrm{p}}} \cdot \sum_{l=1,2\ldots}^{\infty} \lambda_l \cdot (p + Q \cdot l) \cdot \sin(\gamma_{\mathrm{m}}(p + Q \cdot l) - p\Omega_{\mathrm{m}} t) \tag{2.8-5}$$

$$A_{l-}(\gamma_{\mathrm{m}}) = -\frac{\delta \cdot \hat{B}_1 \cdot \pi}{2 \cdot \mu_0 \cdot p \cdot \tau_{\mathrm{p}}} \cdot \sum_{l=1,2\ldots}^{\infty} \lambda_l \cdot (p - Q \cdot l) \cdot \sin(\gamma_{\mathrm{m}}(p - Q \cdot l) - p\Omega_{\mathrm{m}} t) \tag{2.8-6}$$

When the equivalent current loading is changed to the current loading of equation 2.8-1, the amplitude of the cogging torque $M_{\mathrm{cog},l,\mu}$ depends on the fundamental component of the magnetic flux $\hat{B}_1$ and the permeance parameter λ_{l} from the equivalent current loading, the magnetic flux from the rotor $\hat{B}_\mu$ and the constructive parameters such as the iron stack length l_{Fe} and the inner stator diameter d_{si}. The argument of the cogging torque will depend on the term μp from the argument part of the $\hat{B}_\mu$ and it will depend on the term $p \pm Q \cdot l$, which comes from the argument part of the equivalent current loading. In this situation, the generation of cogging torque only is possible if the terms $p \pm Q \cdot l$ and μp are the same. For that, two different cases can be seen to calculate the rotor harmonic orders μ that contribute to the generation of the cogging torque:

$$\mu = 1 + l \cdot Q/p \tag{2.8-7}$$

$$\mu = 1 - l \cdot Q/p \tag{2.8-8}$$

Since μ is an odd and integer number (1, 3, 5…) and l is an integer number (1, 2, 3…), they can be defined as $\mu = 2k + 1$ and $l = 2k \cdot p/Q$. The term k is also an integer number (1, 2, 3…). Finally, the frequency of the cogging torque harmonics ω_l that will appear in the cogging torque *Fourier* analysis can be calculated with the term l, the number of stator slots Q and the electrical angular speed ω_{e}:

$$\omega_l = l \cdot Q \cdot \omega_{\mathrm{e}}/p \tag{2.8-9}$$

Table 4 shows the first rotor harmonic orders, of three machines, which contribute to the generation of cogging torque. The first model is a motor with integer slot winding with $q = 2$ and the second and third models have fractional slot winding with $q = 1.5$ and $q = 2.5$. It can be seen that the most relevant harmonic orders for the fractional slot winding configurations are higher than the most relevant harmonic orders of the integer slots winding model. Thus, the amplitude of the cogging torque is smaller in the case of fractional slot winding models since $M_{\mathrm{cog},l,\mu} \sim \hat{B}_\mu$ and $\hat{B}_\mu \sim 1/\mu$. Furthermore, the increase of the number of the stator slots for the configurations of the fractional slot winding causes a significant reduction on the amplitude of the cogging torque.

Table 4: The first rotor harmonic orders, which contribute to the cogging torque generation for integer and fractional slot winding machines.

Model	k	l	rotor harmonic order, μ
$q = 2$	6	1	11, 13
$q = 1.5$	9	2	17, 19
$q = 2.5$	15	2	29, 31

This method, using fractional slot windings, improves the cogging torque and torque ripple reduction with a few changes in manufacturing process and without increases in cost. It is a good candidate to substitute the skewing or step-skewing methods, which are quite expensive [35].

2.9. Vibrations and electromagnetic noise in PMSM

Many researches attribute the cogging torque and the torque ripple to be the main reasons of the vibrations and hence the electromagnetic noise of the PMSM [9], [11], [36]. Although, it is true that both phenomena contributes to the vibration of the stator structure, it has been proved that the main cause of the vibrations is the radial component of the electromagnetic force created for the magnetic flux density in the air-gap [7]. The radial and tangential components of the electromagnetic forces can be calculated, by using the *Maxwell* stress tensor.
In order to calculate the vibration and the sound of the motor, the radial component of the electromagnetic force is set up as radial pressure in order to have the force per unit area at any point of the air-gap in equation 2.9-1.

$$p_{\mathrm{r}}(\gamma,t) \approx \frac{F_{\mathrm{r}}}{l_{\mathrm{Fe}} \cdot x} = \frac{[B_{\mathrm{r}}^2(\gamma,t) - B_{\mathrm{t}}^2(\gamma,t)]}{2 \cdot \mu_0} \tag{2.9-1}$$

The internal radial pressure caused by the electromagnetic forces makes that the stator structure suffers deformation. However, the radial forces appear depending on the combination between the poles and the slots of the machine. The vibration and noise of a PMSM can be predicted starting with the calculation of the internal radial pressure from a function of the rotor angle γ, and then a fast *Fourier* transform (FFT) of the function is carried out to see the amplitude contribution of each harmonic of the radial pressure. In the *Fourier* analysis, there is one harmonic component which has the biggest amplitude and hence it is used to calculate the deformation or the displacement, which stator structure suffers. This displacement x can be calculated by FEA and analytically by using the harmonic order and its amplitude, the inner and outer radius of the stator and some parameters of the material of the stator core such as the *Poisson´*s ratio and the *Young´*s modulus [7]. The sound power P_{s} that a machine will emit is expressed in equation 2.9-2 and it is function of the displacement x, the exitation frequency of the stator f_{exc}, the geometric parameters such as iron stack length l_{Fe} and outer stator radius r_{so}, the relative sound intensity σ_{rel}, the traveling speed of sound in the medium c and the air density ρ [7].

$$P_{\mathrm{s}} = 4 \cdot \sigma_{\mathrm{rel}} \cdot \rho \cdot c \cdot \pi^3 \cdot f_{\mathrm{exc}}^2 \cdot x^2 \cdot r_{\mathrm{so}} \cdot l_{\mathrm{Fe}} \tag{2.9-2}$$

Finally, the noise that the machine emits L_{w} is calculated from power sound to decibels using the sound power level reference $P_{\mathrm{s,ref}}$ of 10^{-12} W.

$$L_{\mathrm{w}} = 10 \cdot \log\left(\frac{2 \cdot P_{\mathrm{s}}}{P_{\mathrm{s,ref}}}\right) \tag{2.9-3}$$

An approximated estimation of the vibration and noise between two machines can be achieved from the calculation of the internal radial pressure, since the noise is proportional to the sound power $L_{\mathrm{w}} \sim P_{\mathrm{s}}$, which is proportional to the displacement $P_{\mathrm{s}} \sim x$ and this is proportional to the radial pressure $x \sim p_{\mathrm{r}}$.

2.10. Torque production and maximum torque per ampere (MTPA) technic

For the control of the motor, the *abc* reference frame of the balanced 3-phase system can be transformed to a *dq* reference frame by using the *Park* transformation, as the Figure 19 shows. The *abc* reference can be represented in a stationary two-phase reference frame or also called the *αβ* stator reference frame. If the *αβ* reference rotates at the same frequency as the three-phase reference, the projections will become constant. Thus, the three-phase AC values will be converted into two DC quantities, the *dq* rotor reference frame. These references are the "direct" and "quadrature" axes, which has the reference of the rotor position θ [23].

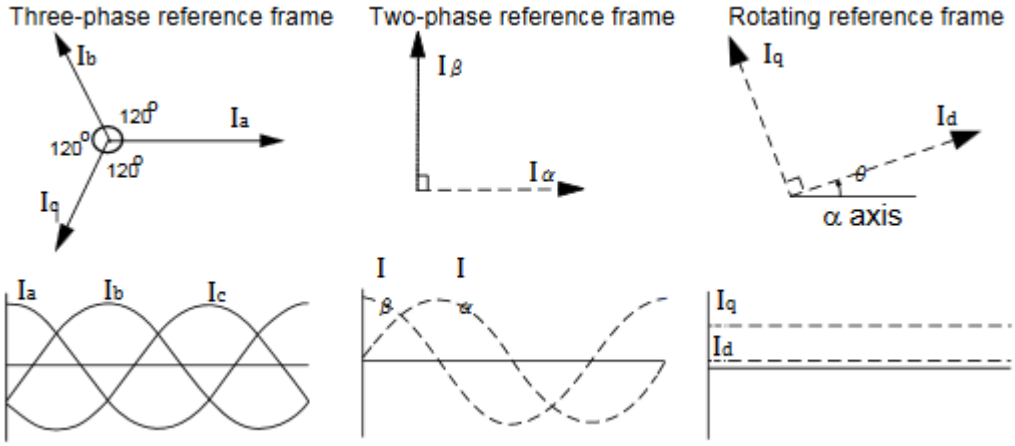

Figure 19: Park transformation from a three-phase reference frame to a *dq* reference frame [37].

When the *dq* reference frame is achieved, the control of the motor becomes easier since the values of the stator currents, back-emf and voltages become DC quantities. Thus, the equations that will be used to explain the generated torque can be deduced from the motor model in *dq* reference frame in Figure 20.

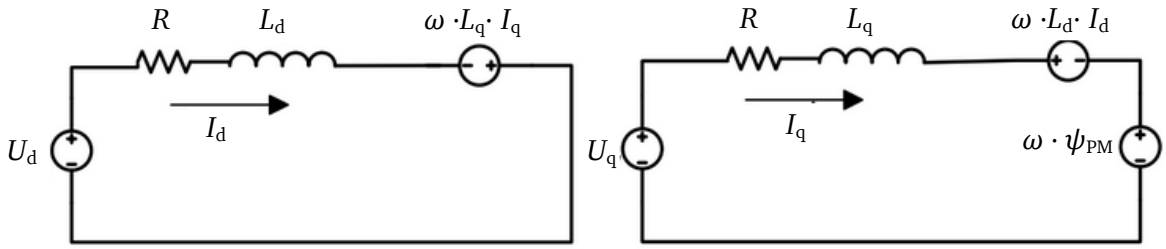

Figure 20: Motor model of a PMSM in *dq* reference frame.

$$\begin{bmatrix} U_\mathrm{q} \\ U_\mathrm{d} \end{bmatrix} = \begin{bmatrix} R + L_\mathrm{q}\frac{d}{dt} & \omega L_\mathrm{d} \\ -\omega L_\mathrm{q} & R + L_\mathrm{d}\frac{d}{dt} \end{bmatrix} \cdot \begin{bmatrix} I_\mathrm{q} \\ I_\mathrm{d} \end{bmatrix} + \begin{bmatrix} \frac{\omega\psi_\mathrm{PM}}{\sqrt{2}} \\ 0 \end{bmatrix} \tag{2.10-1}$$

When the voltage formulas in the *dq* reference frame are known, the generated torque from the machine can be deduced from the electrical power equation 2.10-2:

$$P_\mathrm{el} = m \cdot U_\mathrm{s} \cdot I_\mathrm{s} \cdot \cos(\varphi_\mathrm{s}) = m \cdot \mathrm{Re}\{\underline{U_s}\underline{I_s^*}\} = m \cdot (U_\mathrm{q} I_\mathrm{q} + U_\mathrm{d} I_\mathrm{d}) \tag{2.10-2}$$

With the supposition of no losses the electrical power can be set equal to the mechanical power, then:

$$M_{\mathrm{e}} = \frac{P_{\mathrm{m}}}{\omega_{\mathrm{syn}}} \tag{2.10-3}$$

$$M_{\mathrm{e}} = m \cdot p \cdot \left(\frac{\psi_{\mathrm{PM}}}{\sqrt{2}} \cdot I_{\mathrm{q}} + \left(L_{\mathrm{d}} - L_{\mathrm{q}} \right) \cdot I_{\mathrm{d}} I_{\mathrm{q}} \right) \tag{2.10-4}$$

The equation 2.10-4 shows the torque generated by a PMSM. The torque arises from two components. The first one is the magnetic torque which is generated by the interaction between the permanent magnetic flux and the armature winding flux:

$$M_{\mathrm{magnetic}} = m \cdot p \cdot \frac{\psi_{\mathrm{PM}}}{\sqrt{2}} \cdot I_{\mathrm{q}} \tag{2.10-5}$$

And the second component is generated by the saliency ratio which is the so called reluctance torque:

$$M_{\mathrm{reluctance}} = m \cdot p \cdot \left(L_{\mathrm{d}} - L_{\mathrm{q}} \right) \cdot I_{\mathrm{d}} I_{\mathrm{q}} \tag{2.10-6}$$

From the reluctance part of the generated torque another concept is introduced for PMSM, the saliency ratio. For a SPMSM like Figure 21, the flux path crossing the magnets for any position of rotor is always the same. Thus, there is no difference between the inductances for *d* and *q* axes. Thus, the generated torque for a SPMSM calculated with the equation 2.10-4, it will show that the reluctance part is zero. If the same flux path is built for an IPMSM like Figure 22, it can be seen that for different rotor positons the value of the inductances vary in *d*-axis and *q*-axis. Furthermore, the notable difference between the inductances in both axes will contribute to generate the reluctance torque. In case of Figure 22 (b) the inductance is very low since the magnets have more reluctance than the iron stack, and the opposite happens with the Figure 22 (a) [2].

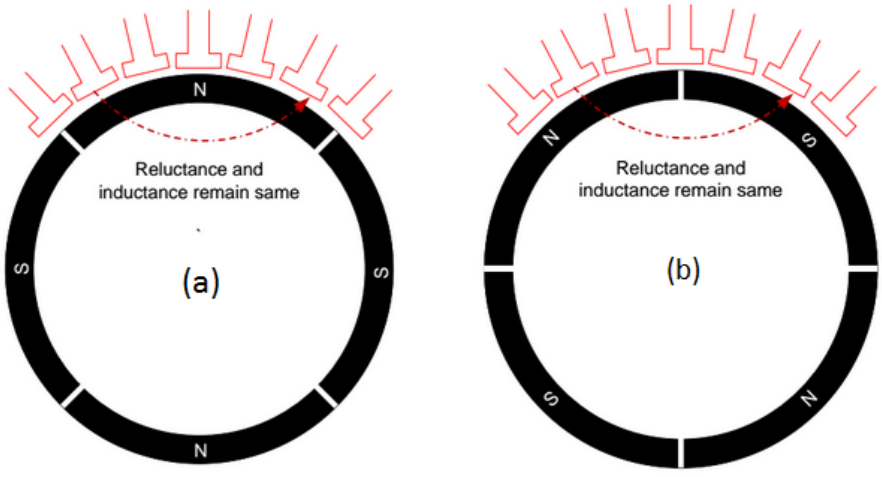

Figure 21: Flux path of a SPMSM. (a) *q*-axis flux path and (b) *d*-axis flux path [2].

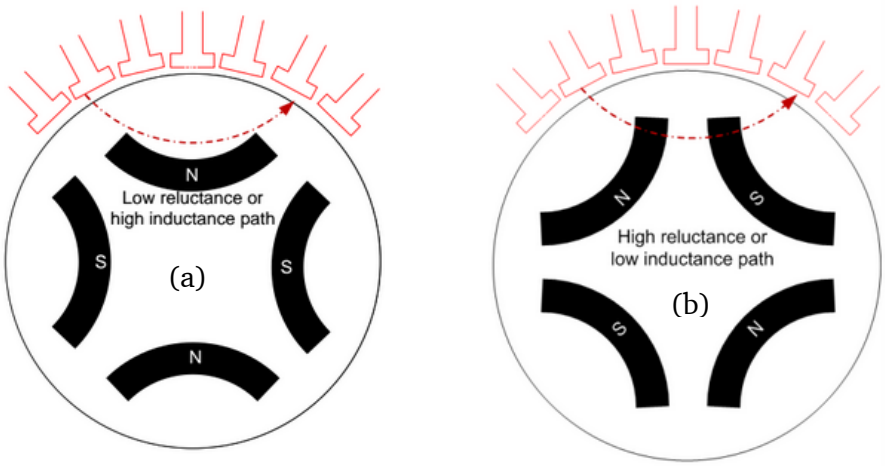

Figure 22: Flux path of an IPMSM. (a) *q*-axis flux path and (b) *d*-axis flux path [2].

In Figure 22 the inductance in *d*-axis (a) is lower than the inductance in *q*-axis (b). If a positive I_d current is introduced, the reluctance torque will be negative and the total amount of generated torque will be lower than expected. Thus, a negative I_d current should be introduced to generate positive reluctance torque. The motor control introduce the negative I_d current with the variation of the current phase angle β, which is a negative angle between I_s and the *q*-axis. In an IPMSM, there are a lot of combinations between the negative *d* current and the *q* current that gives the same amount of torque. As literature shows in [2], for a fix torque there is a combination of *d* and *q* currents that gives the lesser stator current I_s. Since the copper losses increase with squared of current, the low value of current I_s will be desired. Since current and torque are proportional, the same explanation can be used to explain what happen for a given and fix stator current. The total amount of output torque will vary with a fix current I_s and the control technique that tries to look for the highest output torque varying the current phase angle β for a given current is the so called maximum torque per ampere (MTPA).

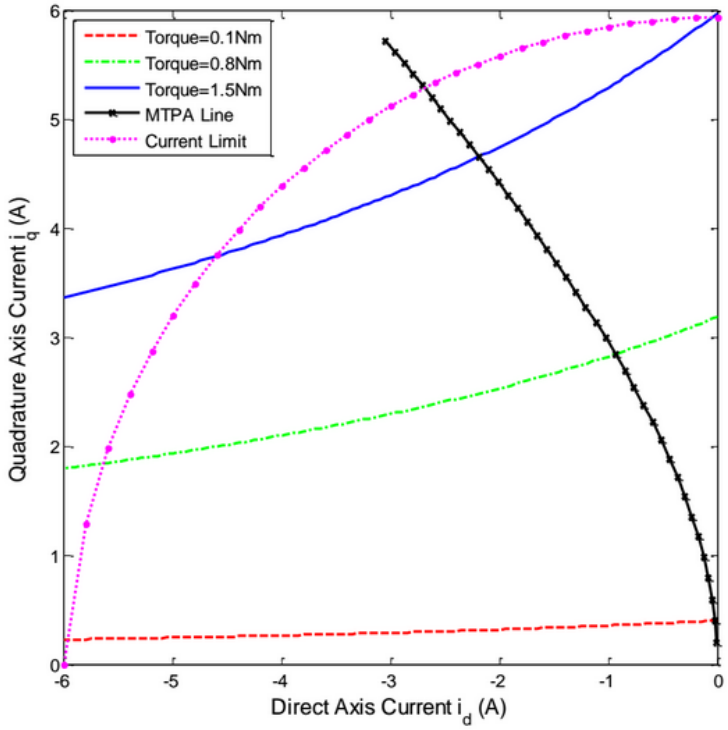

Figure 23: For a given torque there is a combination of currents I_d and I_q, which is the lowest value to minimize the copper losses [2].

2.11. Flux weakening operation

Many applications need to work with a wide range of speeds such as an electrical vehicle, a tooling machine with a high cutting speed and a constant power at the same time or a washing machine with several speed programmes. Permanent magnet synchronous machines allow for work requiring a wide speed range. However, a flux weakening operation has to be implemented when high speeds are achieved in order not to exceed the maximum voltage of the inverter and damage it, since the voltage is proportional to speed and magnetic flux $U_\mathrm{p} \sim \Psi_\mathrm{PM} \cdot n$ [3] [38].

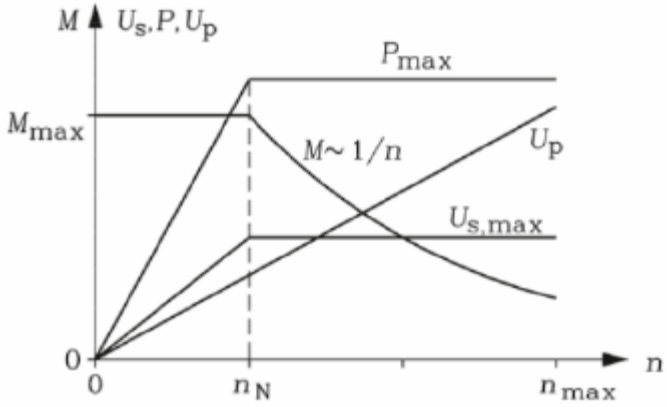

Figure 24: Variables (stator voltage, power, torque, and back-emf) of a PMSM with the increase of speed [3].

Flux weakening operation means that a negative d current has to be introduced to weaken the magnetic flux and hence to stop the voltage rise, if high speeds are achieved. The negative d current makes that the magnetic field of the stator acts against the magnetic field of the magnets. In addition a voltage drop at the stator reactance is introduced $jX_\mathrm{d} \cdot (-I_\mathrm{d})$ and high speeds can be reached as it is showed in Figure 25.

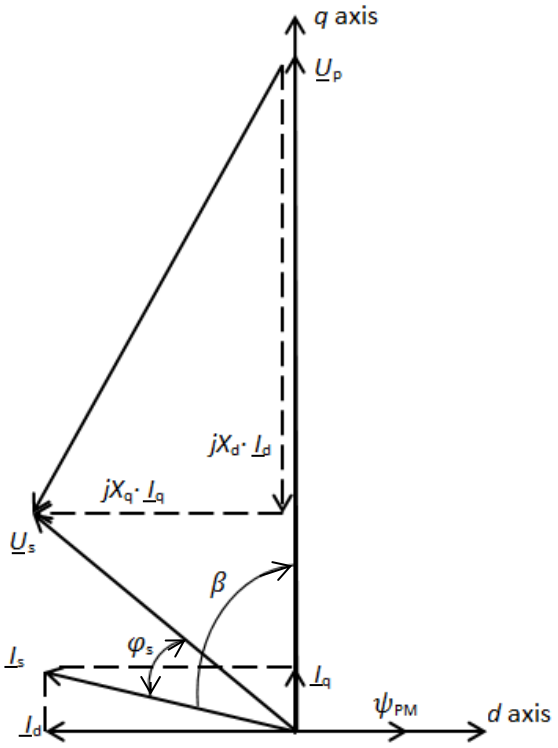

Figure 25: Phasor diagram of a PMSM working in the flux weakening operation.

2.12. Mechanical stress in iron bridges

The utilization of gearless directly coupled high-speed machines such as IPMSM has a lot of benefits like reduction of noise, avoid the maintenance of gear, no gear losses, the nonelectric excitation decreases the rotor losses and small and compact motors can be achieved. However the utilization of high-speed makes the manufacturer think about new mechanical problems such as the mechanical stress in the iron bridges. When an IPMSM is rotating, the iron bridge between the magnet and the rotor edge has to support the stress caused by the centrifugal forces, thus a FEA should be done to guarantee that the bridge will not break due to the centrifugal forces. Additionally, an approximate analytical calculation of the mechanical stress for the rotor structure of IPMSM can be done. For that, an equivalent ring is created with an equivalent mass density ρ_{equiv} [4]. The equivalent ring carries the centrifugal forces that the area of the magnets A_{M} and the area of iron sheets A_{Fe} act on the bridge.

$$\rho_{\mathrm{Fe}} \cdot A_{\mathrm{Fe}} \cdot l_{\mathrm{Fe}} + \rho_{\mathrm{M}} \cdot A_{\mathrm{M}} \cdot l_{\mathrm{Fe}} = \rho_{\mathrm{equiv}} \cdot A_{\mathrm{equiv}} \cdot l_{\mathrm{Fe}} \tag{2.12-1}$$

$$\rho_{\mathrm{equiv}} = \frac{\rho_{\mathrm{Fe}} \cdot A_{\mathrm{Fe}} + \rho_{\mathrm{M}} \cdot A_{\mathrm{M}}}{A_{\mathrm{equiv}}} \tag{2.12-2}$$

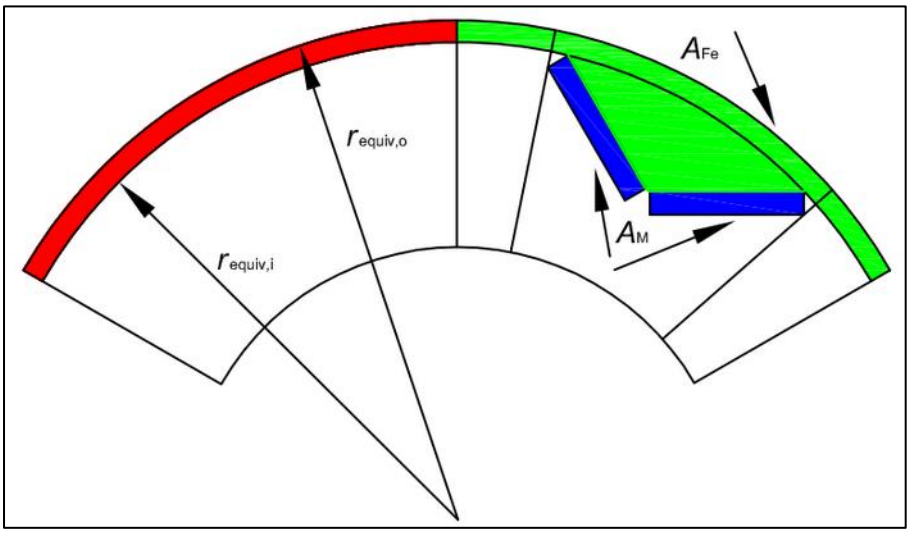

Figure 26: IPMSM with buried V-shape magnets. The parameters for the mechanical stress calculations are drawn. The red area is the equivalent area A_{equiv}, the blue areas are the magnets A_{M} and the green one is the iron area A_{Fe} considered for the calculation.

With the inner and outer radii of the equivalent ring, the equivalent mass density and the rotation speed, the equivalent tangential stress inside of the equivalent ring can be determined as:

$$\sigma_{\mathrm{t,equiv}} = \left(\frac{r_{\mathrm{equiv,o}} + r_{\mathrm{equiv,i}}}{2}\right)^2 \cdot \omega_{\mathrm{overspeed}}^2 \cdot \rho_{\mathrm{equiv}} \tag{2.12-3}$$

As the equivalent tangential stress does not pay attention to the stress at the magnet edges, where is located the maximum stress, a factor of 2 should be considered on the calculation of the tangential stress.

$$\sigma_{\mathrm{t,max}} = 2 \cdot \sigma_{\mathrm{t,equiv}} \tag{2.12-4}$$

The tangential stress inside the iron bridges has to be compared to the stress that the iron sheets material can support before the material starts breaking after a plastic deformation. Thus, some concepts of mechanical stress from materials are explained with the help of Figure 27. The yield strength R_e is the limit stress that a material supports before starts a plastic deformation. The yield strength $R_{p,\,0.2\%}$ is a limit stress that if the material does not exceed it, it can go back to initial state. In contrary case, the material remains with a plastic deformation. The ultimate tensile strength or tensile strength R_m is the point that the material starts breaking.

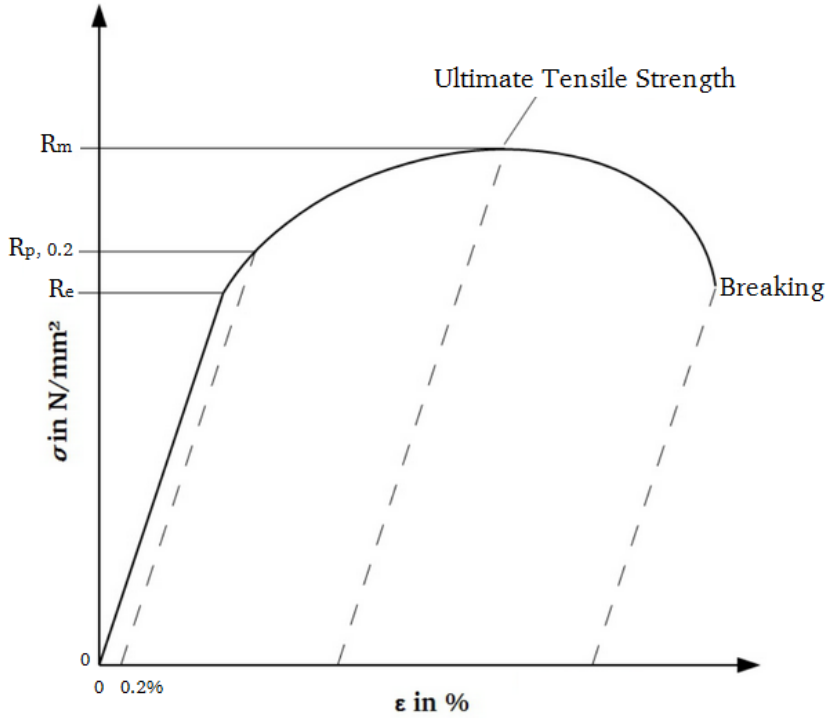

Figure 27: Schematic stress/strain curve for a material with the yield strength R_e, the 0.2%-yield strength $R_{p,\,0.2\%}$ and the tensile strength R_m points [39].

In order to know the life time of a material, a fatigue stress test is carried out to know for a specific stress S how many cycles N the material will remain into the no breaking condition. From the Figure 28 it can be seen a typical S-N curve, which is drawn with a logarithmic scale in the x-axis. The points corresponding to a specific stress and specific number of cycles that are above the $S'f$ curve break for fatigue and below the same curve the material is not breaking.

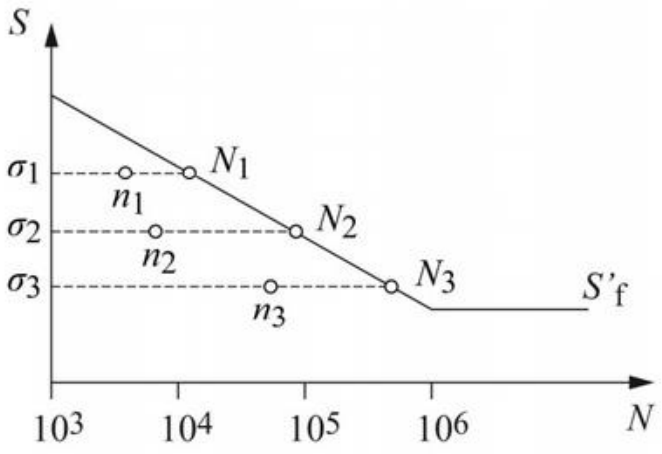

Figure 28: *S-N* curve for the fatigue properties of a given material [40].

2.13. Losses calculations

When an electrical machine is at load condition, there is a difference between the input power and the output power, which are the losses. An electrical motor has several losses such as eddy current and hysteresis losses in iron sheets, ohmic losses in stator windings, friction losses in the air-gap and bearings, losses in the rotor magnets due to space harmonics in the back-mmf, losses due to the inverter supply, losses in the stator windings due to the current displacement effect and other additional losses which are normally smaller than the previous commented [18], [23]. In this thesis, the losses which will be considered are the ohmic losses with the current displacement effect due to the high currents and the iron and friction losses due to high rotating speeds.

2.13.1. Ohmic losses

For an IPMSM the ohmic losses arise from the stator windings. The ohmic losses are proportional to the square of the phase current I_s and proportional to the resistance per phase R_s of the windings. Thus the ohmic losses can be calculated, without taking into account any current displacement effect, with equation 2.13-1.

$$P_{\mathrm{Cu,dc}} = 3 \cdot R_s \cdot I_s^2 \tag{2.13-1}$$

The resistivity of a material varies with the change of the temperature. For that, the copper conductivity, the resistance and hence the ohmic losses will vary for a given temperature ϑ_{Cu} in °C. In that case, the temperature coefficient k_ϑ should be taken into account for the calculations of the ohmic losses, which the equation 2.13-2, and the resistance at a given temperature is calculated with equation 2.13-3.

$$k_\vartheta = \frac{\vartheta_{\mathrm{Cu}} + 235}{255} \tag{2.13-2}$$

$$R_s = R_{s,20°} \cdot \left(1 + \frac{\vartheta_{\mathrm{Cu}} - 20}{255}\right) \tag{2.13-3}$$

When AC current is flowing through conductors with a frequency, current displacement effects appear. These effects mean that the current is not perfectly distributed around the coil, and then it causes displacement. These effects increase with the height of conductors and the supply of high frequencies. There are three components, which cause displacement. The skin effect, which causes current displacement from the conductor itself, the proximity effect which causes current displacement by the proximity of another conductor and the displacement effect or also known as the second order current displacement which causes current displacement in the slot [41].

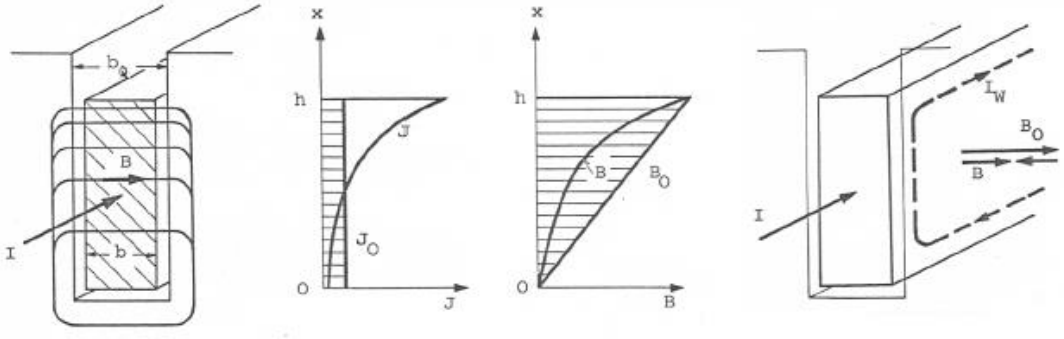

Figure 29: Current displacement effect. Conductor current *I*, slot magnetic flux *B*, slot height *h*, current density *J* [13].

The second order current displacement is explained with Figure 29. This effect is created by the flowing of AC current through the conductors of a slot. The current generates a slot magnetic flux, which induces eddy currents. These eddy currents results in a magnetic self-field that acts against the slot magnetic flux and hence the current is displaced to the upper part of the slot where the opposite magnetic fluxes effect is smaller than in the bottom part [23]. Since there is current displacement in the conductors, the total effective area where the current flows is reduced. Thus a reduction of the area causes an increase of ohmic losses. For that, the current displacement effect should be considerate in the calculation of ohmic losses with a factor $\bar{K}_{\mathrm{R2}}$, instead of the K_{R2}, due to the negligible stray magnetic flux in the winding overhangs [18] [42].

$$P_{\mathrm{Cu,ac}} = 3 \cdot \bar{K}_{\mathrm{R2}} \cdot R_{\mathrm{s}} \cdot I_{\mathrm{s}}^2 \tag{2.13-4}$$

$$\bar{K}_{\mathrm{R2}} - 1 = \frac{K_{\mathrm{R2}} - 1}{(1 + l_{\mathrm{b}}/l_{\mathrm{Fe}})} \tag{2.13-5}$$

$$K_{\mathrm{R2}} = \varphi(\xi) + \frac{m_{\mathrm{v}}^2 - 1}{3} \cdot \psi(\xi) \tag{2.13-6}$$

$$\varphi(\xi) = \xi \cdot \frac{\sinh 2\xi + \sin 2\xi}{\cosh 2\xi - \cos 2\xi} \tag{2.13-7}$$

$$\psi(\xi) = 2\xi \cdot \frac{\sinh \xi - \sin \xi}{\cosh \xi + \cos \xi} \tag{2.13-8}$$

where m_{v} is the number of vertical wire layers in the slot with the equivalent wire height h_{Cu}, and ξ is the reduced conductor height.

$$\xi = h_{\mathrm{Cu}} \cdot \sqrt{\pi \cdot f \cdot \mu_0 \cdot \frac{n_{\mathrm{h}} \cdot h_{\mathrm{Cu}}}{b_{\mathrm{Q}}} \cdot \kappa_{\mathrm{Cu}}} \tag{2.13-9}$$

In equation 2.13-9, f is the stator frequency, n_{h} is the number of horizontal wire layers in the slot with the equivalent wire height h_{Cu}, b_{Q} is the average slot width, κ_{Cu} is the copper electric conductivity at the winding temperature and h_{Cu} is the equivalent wire height for round wires calculated in equation 2.13-10 with the wire diameter d_{Cu}:

$$h_{\mathrm{Cu}} = \sqrt{\pi} \cdot \frac{d_{\mathrm{Cu}}}{2} \tag{2.13-10}$$

2.13.2. Iron losses

The iron losses are created by two components, the hysteresis losses and the eddy current losses. The hysteresis losses depend on the iron sheets material, the magnetic flux density B^2 and the stator frequency f. The eddy currents are induced from the AC main flux in the iron sheets of the stator and rotor core and depend on B^2 and f^2. In order to mitigate or reduce these eddy currents and hence the eddy losses, the iron sheets are laminated with insulation between the sheets, which are also built very thin. The thickness is usually 0.5 mm or 0.35 mm. Also for high frequencies operations, 0.1 mm of thickness is also available.
The IPMSM suffers more iron losses than SPMSM due to the smaller air-gap. The shorter the air-gap length, the more magnetic field oscillations the rotor is exposed to. These oscillations produce on the iron bridges of IPMSM higher amplitudes of the air-gap field harmonics. Thus, contributing to more iron losses due to they are dependable of B^2.

In order to calculate the iron losses analytically, two equations are presented for the iron losses on the teeth $P_{\mathrm{Fe,d}}$ and on the yoke $P_{\mathrm{Fe,y}}$. The difference between both equations will be a higher magnetic flux in the teeth since there is less area than in the yoke. The two punching factors k_{Vd} and k_{Vy} are considered.

$$P_{\mathrm{Fe,d}} = k_{\mathrm{Vd}} \cdot \left(\frac{B_{\mathrm{d,max}}}{1.0}\right)^2 \cdot \left(\rho_{\mathrm{Hy}} \cdot \left(\frac{f}{50}\right) + \rho_{\mathrm{Ft}} \cdot \left(\frac{f}{50}\right)^2\right) \cdot m_{\mathrm{ds}} \tag{2.13-11}$$

$$P_{\mathrm{Fe,y}} = k_{\mathrm{Vy}} \cdot \left(\frac{B_{\mathrm{y,max}}}{1.0}\right)^2 \cdot \left(\rho_{\mathrm{Hy}} \cdot \left(\frac{f}{50}\right) + \rho_{\mathrm{Ft}} \cdot \left(\frac{f}{50}\right)^2\right) \cdot m_{\mathrm{dy}} \tag{2.13-12}$$

The iron losses calculations depend on the specific loss density for each hysteresis losses ρ_{Hy} and eddy current losses ρ_{Ft} and the mass of each iron teeth m_{ds} and iron yoke m_{dy}.
The sum of both equations represents the total iron losses:

$$P_{\mathrm{Fe}} = P_{\mathrm{Fe,d}} + P_{\mathrm{Fe,y}} \tag{2.13-13}$$

2.13.3. Friction losses

The friction losses in the air-gap are very small compared with the ohmic and iron losses. These losses are caused in the air-gap when the machine is rotating and the slot openings contribute to increase these losses [18].
The calculation of friction losses is done with equation 2.13-14, where c_{f} is the friction coefficient, the air mass density ($\rho_{\mathrm{air}} = 0.95\ \mathrm{kg/m^3}$ at 100°C), n is the rotational speed, r_{ro} is the rotor outer radius and l_{Fe} is the iron stack length.

$$P_{\mathrm{fr}} = c_{\mathrm{f}} \cdot \pi \cdot \rho_{\mathrm{air}} \cdot (2\pi \cdot n)^3 \cdot r_{\mathrm{ro}}^4 \cdot l_{\mathrm{Fe}} \tag{2.13-14}$$

The friction coefficient c_{f} is defined by the *Reynolds*-number *Re*, which depends on the air-gap and the kinematic viscosity of air ($\nu_{\mathrm{air}} = 0.23 \cdot 10^{-4}\ \mathrm{m^2/s}$ at 100°C).

$$c_{\mathrm{f}} = 0.035 \cdot Re^{-0.15} \tag{2.13-15}$$

$$Re = 2\pi \cdot n \cdot r_{\mathrm{ro}} \cdot \frac{\delta}{\nu_{\mathrm{air}}} \tag{2.13-16}$$

2.13.4. Motor efficiency

When the total losses in the motor are defined, the efficiency η can be calculated. This parameter gives a relation between the total electrical input power and the total mechanical output power, which the motor uses to generate work.

$$\eta = \frac{P_{\mathrm{m}}}{P_{\mathrm{el}}} = \frac{P_{\mathrm{m}}}{P_{\mathrm{m}} + P_{\mathrm{d}}} \tag{2.13-17}$$

where P_{el} is the electrical input power, P_{m} is the mechanical output power and P_{d} is the sum of all the considered losses in equation 2.13-18:

$$P_{\mathrm{d}} = P_{\mathrm{Cu,ac}} + P_{\mathrm{Fe}} + P_{\mathrm{fr}} \tag{2.13-18}$$

3. Design of the IPMSM with fractional slot windings

In a synchronous machine, the magnetic flux density of the air-gap B_δ that is generated by the electrically excited circuit or the permanent magnets on the rotor, acts with the current i that flows through the conductors on the stator by generating a tangential force F. The current can be replaced for the current loading A. Thus, the tangential force is proportional to the magnetic flux density B_δ, the current loading A, the length of the machine l_{Fe} and the number of poles p. From the tangential force F and the stator inner radius, where the force acts, the electromagnetic torque can be calculated; $M_{\mathrm{e}} = F \cdot r_{\mathrm{si}}$. Furthermore, the internal power of an AC synchronous machine, which comes from the air-gap, can be calculated with the rotational synchronous speed and the electromagnetic torque; $P_\delta = 2\pi \cdot n_{\mathrm{syn}} \cdot M_{\mathrm{e}}$. With the internal power of the machine and the volume of the rotor, the electromagnetic utilization or *Esson´s* number C can be calculated [23].

$$C = \frac{S_\delta}{d_{\mathrm{si}}^2 \cdot l_{\mathrm{Fe}} \cdot n_{\mathrm{syn}}} = \frac{\pi^2}{\sqrt{2}} \cdot k_{\mathrm{w1}} \cdot A \cdot \hat{B}_{\delta 1} \tag{2.13-1}$$

The *Esson´s* number of a machine gives an idea of how much power the machine can generate for a given rotor volume. This number is used when two different machine are compared since a high value of electromagnetic utilization is desired in order to have machines with a high torque with less amount of volume $C \sim M_{\mathrm{e}}/V_{\mathrm{r}}$.
The electromagnetic utilization is proportional to the current loading A and the magnetic flux density B_δ. The first one is higher for machines with fewer poles, for higher current values and higher number of turns per phase. The ohmic losses are proportional to the square of the total amount of current $P_{\mathrm{Cu}} \sim I^2$, which has a limit for thermal properties of the machines. The induced phase voltage U_{p} is proportional to the number of turns per phase, which will be limited for the maximum voltage of the inverter. The magnetic flux density is given for the magnets in case of a PM machine and its value should be high enough for a better electromagnetic utilization. However, care should be given to the saturation issues in the different parts of the machine as well as the speed of the machine since the iron losses are proportional to magnetic flux density and stator frequency f; $P_{\mathrm{Fe}} \sim B^2 \cdot f + B^2 \cdot f^2$. In the end, when building an electrical machine with a lot of parameters such as geometrical, electrical, mechanical, and thermic, on must compromises to design and built a machine suitable for a given case.

3.1. Operational points of work

In this thesis, the reduction of the cogging torque and torque ripple is desired for a compact machine, which can work in a wide range of speeds. In order to design a compact machine, a high *Esson´s* number is selected to be 5.1 kVA·min/m^3. Furthermore, in order to have a machine with high power density and hence, a high electromagnetic utilization, a high thermal utilization is needed, which is selected to be $A{\cdot}J$ = 5000 (A/cm) ·(A/mm^2). Both values are selected to be the same like an IPMSM machine which was built in the Institute of Electrical Energy Conversion of TU Darmstadt. This machine was built with integer slot windings with $q = 2$ and the rotor step-skewed in 5 steps and 2° skewed between each step. This previous machine without stepping and skewing the rotor will be used to make a comparison with the proposed model with fractional slot winding $q = 1.5$, in chapter 6.
When the electromagnetic utilization C and the thermal utilization $A{\cdot}J$ are specified and before starting the calculation of the electrical and geometrical parameters of the IPMSM, the initial requirements of the machine such as the operational points in nominal and maximum power have to be specified. The operational points are described in Table 5 and Figure 30.

The control of the IPMSM will be carried out for an inverter. A maximum voltage of the inverter with 300 V in the DC bus is chosen. Then the flux weakening control can be used to raise the speed up to 10000 min^{-1}. The maximum phase voltage of the motor must not exceed the calculated phase voltage. The inverter generates the 3-phase AC with the pulse width modulation (PWM). The control of the PWM is carried out with the algorithm called space vector modulation (SVM). This control provides to the motor a maximum phase voltage of $1/\sqrt{3}$ of the DC bus voltage not to operate in over modulation. Equation 3.1-1 calculates the maximum phase voltage that the inverter supplies to the motor:

$$V_{\mathrm{ph,max}} = \frac{U_{\mathrm{DC,inverter}}}{\sqrt{2}\cdot\sqrt{3}} = \frac{300}{\sqrt{2}\cdot\sqrt{3}} = 122.5\ \mathrm{V} \tag{3.1-1}$$

Table 5: Required parameters for each operational point for the design of the IPMSM.

operational point	parameter	symbol	units	value
OP1	maximum torque	M_{max}	Nm	110
	nominal speed	n_{N}	rpm	4167
	maximum power	P_{max}	kW	48
OP2	nominal torque	M_{N}	Nm	55
	nominal speed	n_{N}	rpm	4167
	nominal power	P_{N}	kW	24
OP3	torque	M	Nm	45.8
	maximum speed	n_{max}	rpm	10000
	maximum power	P_{max}	kW	48

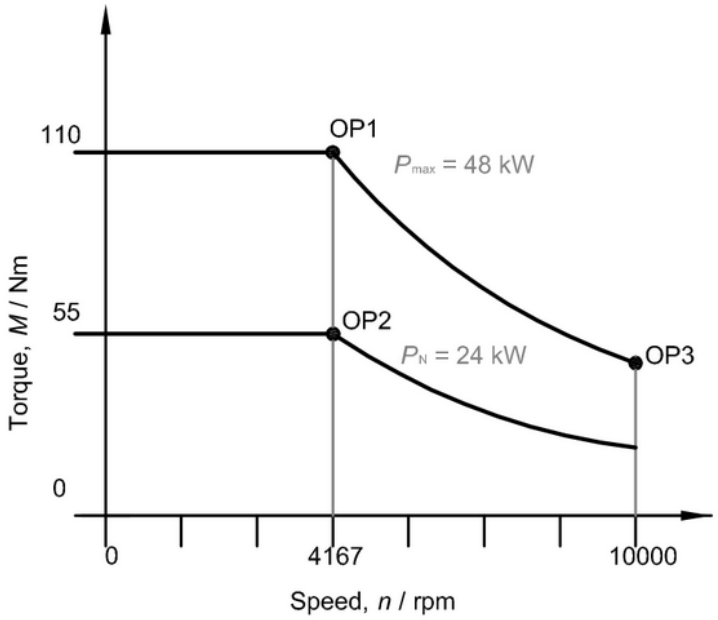

Figure 30: Operational points of the machine at nominal and maximum conditions.

The calculations for the design of the IPMSM will be made for the fractional slot winding model with $q = 1.5$, $Q = 27$ and $p = 6$. Some parameters like the rotor structure, the air-gap length and the outer radius of the stator have been selected as equal as the IPMSM with integer slot winding with $q = 2$, from the Institute. The reason of this selection is to be able to make a comparison between the results of both models of integer slot winding and fractional slot winding machines.

3.2. Materials

The selection of the materials will depend on the purpose of the machine, expected quality and budged. The most appropriate materials will be chosen based on the different characteristics such as magnetic, electrical, mechanical, thermal properties.

3.2.1. Laminated core material

In terms of electromagnetic properties, the iron sheets should have a high permeability to let greater amount of flux flowing. On the other hand, the electrical conductivity should be as low as possible to reduce the eddy currents and hence the Foucault losses. For these reasons the selected material are iron sheets of M270-35A from the SURA® enterprise [43]. The iron sheets have a mass density ρ_{Fe} of 7650 kg/m^3, the thickness of the sheet is 0.35 mm, which is thin enough to reduce eddy currents losses, and the dissipation loss density is 2.7 W/kg at 1.5 T and 50 Hz.
Further parameters of the material can be seen in annex 8.1 and the *B-H* curve of the material at 50 Hz is shown in Figure 31.

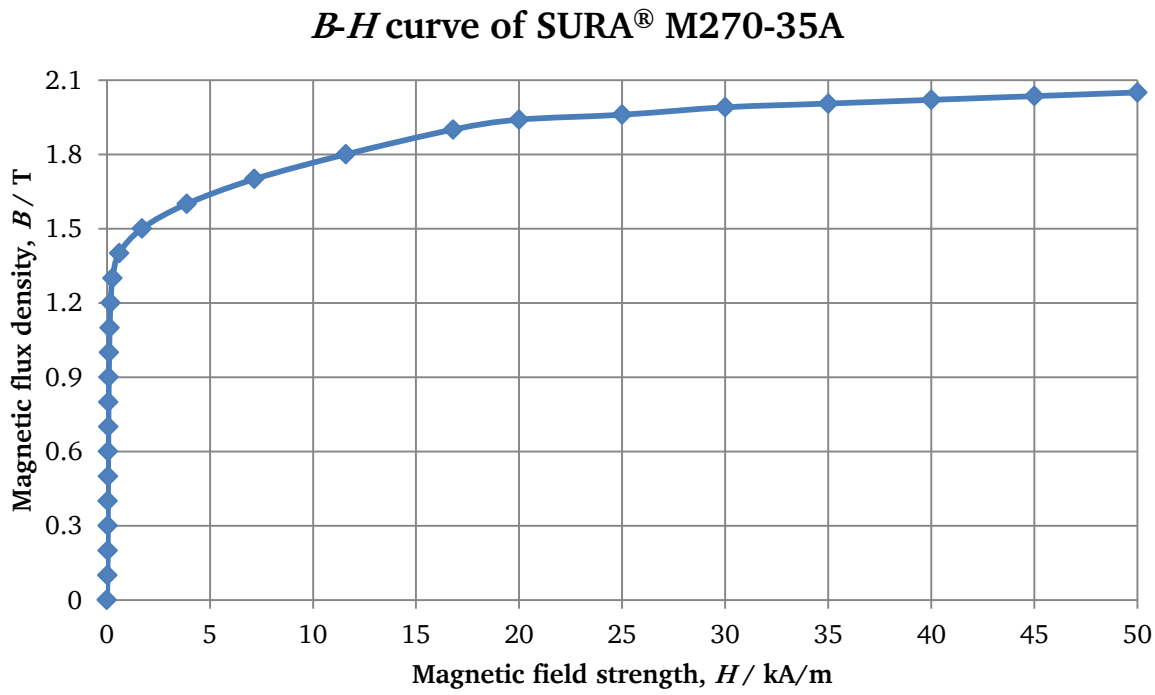

Figure 31: *B-H* characteristic curve of the SURA® material M270-35A at 50 Hz [43].

Since the IPMSM is going to work at high speeds and the iron bridges of the rotor have to support considerable centrifugal forces, the iron sheets materials should have a high value of yield strength to avoid deformations and a high tensile strength to avoid the breaking of the iron sheets. For the proposed material, it has yield strength of 450 N/mm^2 and a tensile strength of 565 N/mm^2.
Since the losses density are not proportional for each value of flux density and also they are not proportional from one value of frequency to another, a table with the losses density for each flux density and frequency is introduced to the FEM program, as can be seen in Figure 32.

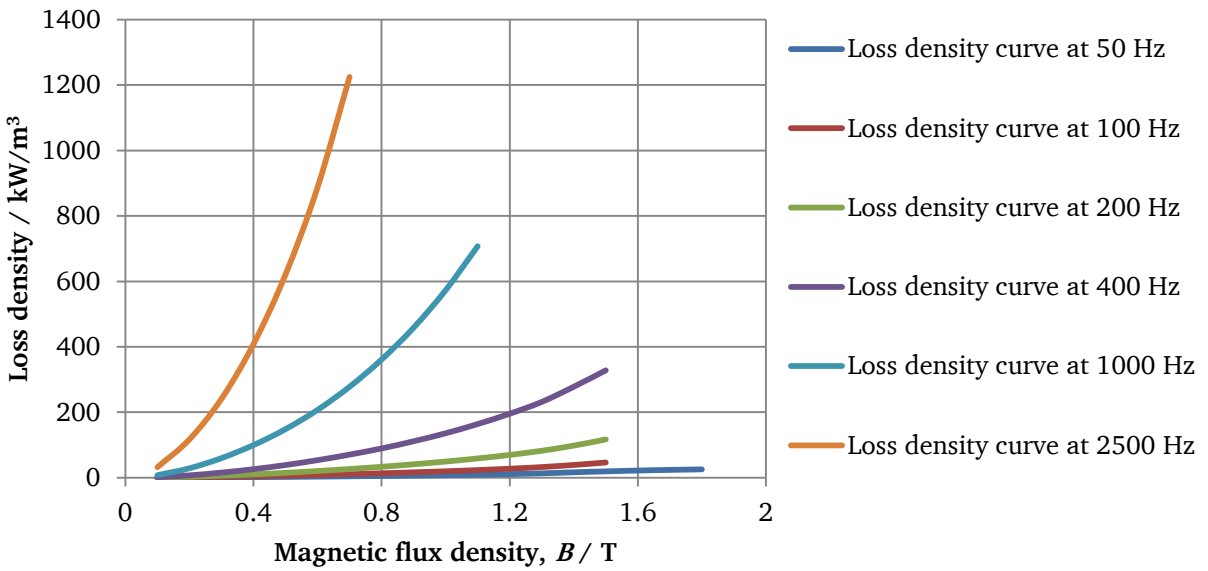

Figure 32: Magnetic flux density versus loss density for different values of frequency of the SURA® material M270-35A [43].

3.2.2. Magnet material

The material for the magnets is the VACODYM 863 TP and it has been selected from the VACUUMSCHMELZE® enterprise [44]. This material with a mass density ρ_M of 7700 kg/m^3, offers a magnetic flux remanence of B_R = 1.29 T and coercivity field strength of H_c = 995 kA/m at 20 °C. For further calculations, the *B-H* curve characteristics for different operating temperatures are shown in Figure 33.

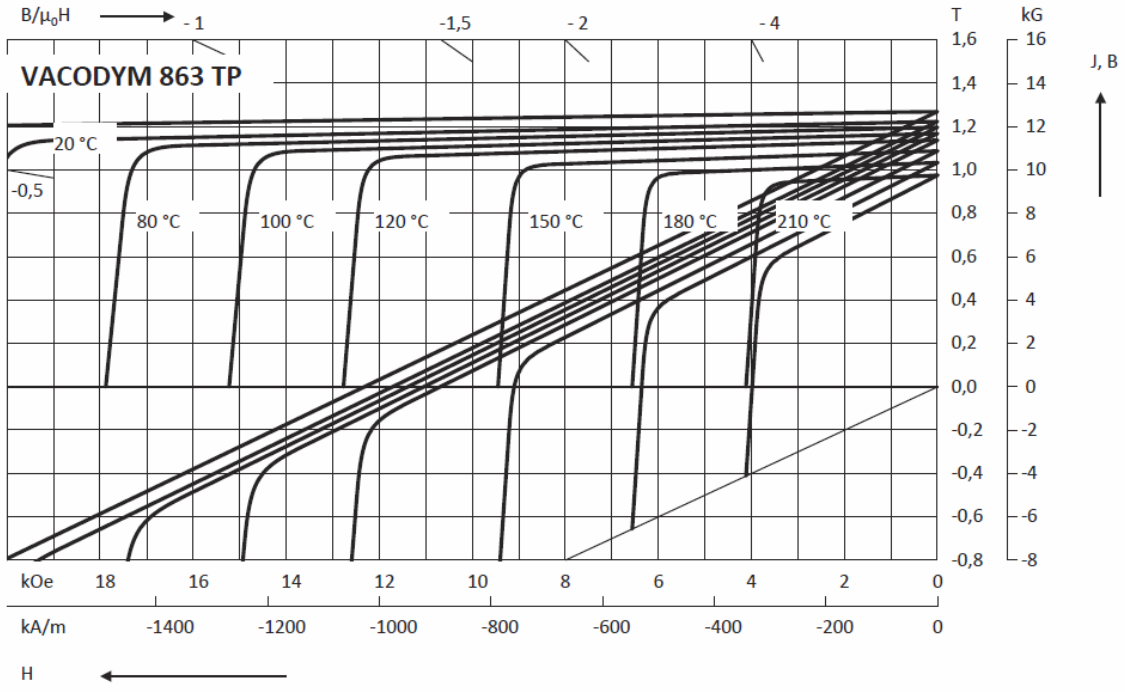

Figure 33: *B-H* curve characteristic of the VACODYM 863 TP material for different operational point´s temperatures [44].

3.3. Analytical calculations for the IPMSM

The design of an electrical machine is calculated for the nominal or rated values of the final machine. Some initial values have to be taken as approximated values from older machines or experience in designing electrical machines. This thesis have the experience of analytical calculations with the IPMSM model with $q = 2$. Therefore, in order to compare the previous machine with the new modifications of $q = 1.5$ and $q = 2.5$, some initial values and parameters are taken as equal. Also if a comparison is going to be made, some geometric structures have to be the same, such as the rotor structure with $p = 6$ and the magnets in a V-shape disposition. The following calculations are done for the IPMSM with fractional slot distributed winding, which case is $q = 1.5$, $Q = 27$, $p = 6$, $m = 3$.

The first values that are considered as approximated are the power factor, which is going to be $\cos\varphi = 1$, the efficiency value $\eta = 0.94$ and a supposition of $P_\delta \cong P_N$. Thus the internal apparent power in the air-gap can be calculated as:

$$S_\delta = \frac{P_\delta}{\eta \cdot \cos(\varphi)} = 25.54\ \text{kVA} \tag{3.3-1}$$

With the internal apparent power and the electromagnetic utilization from equation 2.13-1, the stator inner diameter and the length of the iron stack can be calculated. A parameter that relates the diameter and the length is also needed. This is common used for the analytical calculation of a machine. In this situation a coefficient of $(l_{Fe} / d_{si}) = 1.5$ is selected.

$$C = \frac{S_\delta}{d_{si}^2 \cdot l_{Fe} \cdot n_{syn}} \qquad \begin{matrix} \rightarrow d_{si} = 92.8\ \text{mm} \\ \rightarrow l_{Fe} = 140\ \text{mm} \end{matrix} \tag{3.3-2}$$

Next, with the inner stator diameter d_{si} and the number of poles $2p$, the pole pitch τ_p can be calculated. The pole pitch is the circumference distance that belongs to one pole:

$$\tau_p = \frac{d_{si} \cdot \pi}{2p} = 48.59\ \text{mm} \tag{3.3-3}$$

Before doing the calculation of the number of turns per phase, the calculation of the winding factor $k_{W,1}$ is needed for the fundamental component $v = 1$. Furthermore, in order to know the value of the coil span W, the phasor and voltage diagram for the distributed winding is going to be drawn. The calculation of the fractional slot distributed windings starts with the formulas in section 2.4.4:

$$q = \frac{Q}{2 \cdot p \cdot m} = \frac{z}{n} = \frac{3}{2} \tag{3.3-4}$$

Since the denominator n is an even number, the calculation is carried out with a 2nd-grade definition:

Table 6: Calculation of a fractional slot distributed winding for a 2nd-grade case.

	2nd-grade	value
denominator, n	even	2
t	$2p/n$	3
layer	two	2
Q^*	Q/t	9
p^*	$n/2$	1
t^*	1	1

Table 6 shows the calculated parameters for drawing the phasor and voltage diagram. In this case, the number of basic phasor diagrams t is 3 and the number of slots per basic phasor diagram Q^* is 9. Also with the distance between two adjacent slots α_u and the distance between two slots α_z, the phasor diagram is drawn:

$$\alpha_u = \frac{360 \cdot p^*}{Q^*} = 40° \tag{3.3-5}$$

$$\alpha_z = \frac{360 \cdot t^*}{Q^*} = 40° \tag{3.3-6}$$

Figure 34 shows the phasor diagram with the three basic phasor diagrams t represented with 3 circles. The fist basic phasor diagram contain the slots from 1 to 9, the second diagram has the slots from 10 to 18 and the third one from the slot 19 to 27.

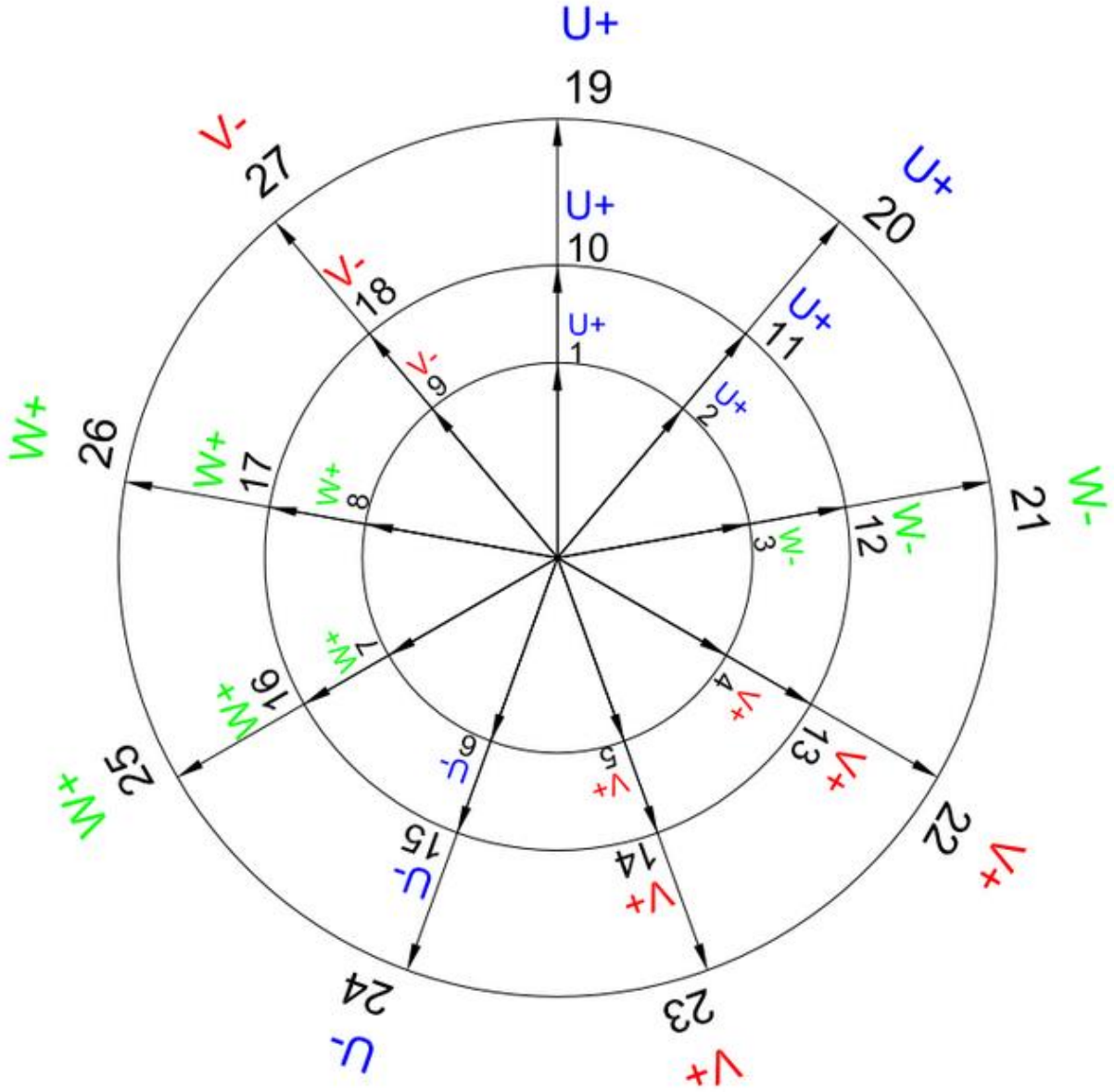

Figure 34: Phasor diagram distribution of the fractional slot distributed winding of 27 slots and 6 poles.

From the phasor diagram, the voltage diagram can be drawn taking each slot voltage and drawing with the same module and angle. The slots are wounded from the positive to the negative site of the coil and the total number of slots of one phase generates the voltage of that phase. For example, the slots (1, 2, 6, 10, 11, 15, 19, 20, and 24) generate the phase voltage U.

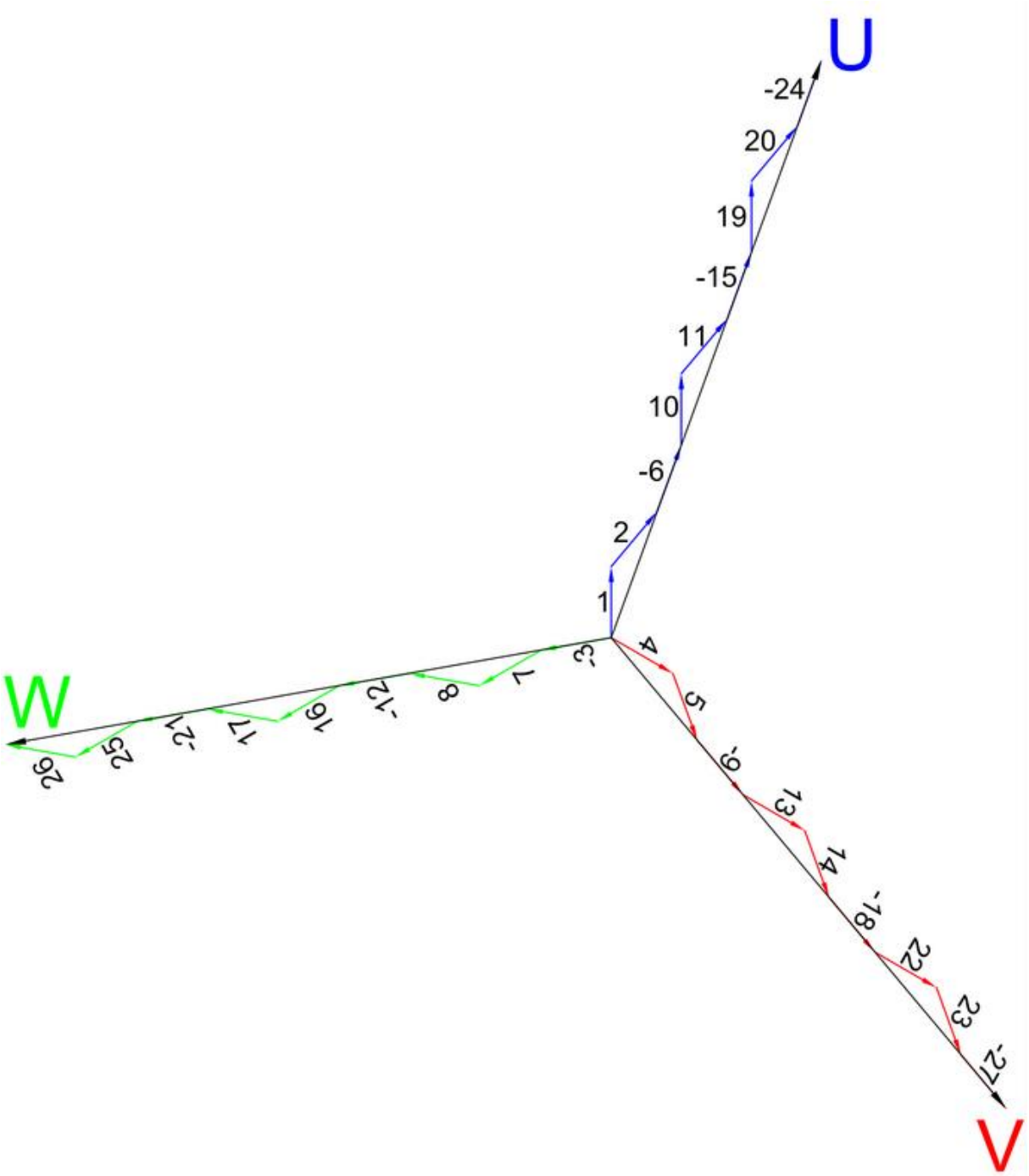

Figure 35: Voltage phase diagram of the fractional slot distributed winding of 27 slots and 6 poles.

Also from the phasor diagram in Figure 34, the slot voltage sequence can be drawn and the coil span W can be deduced from Figure 36:

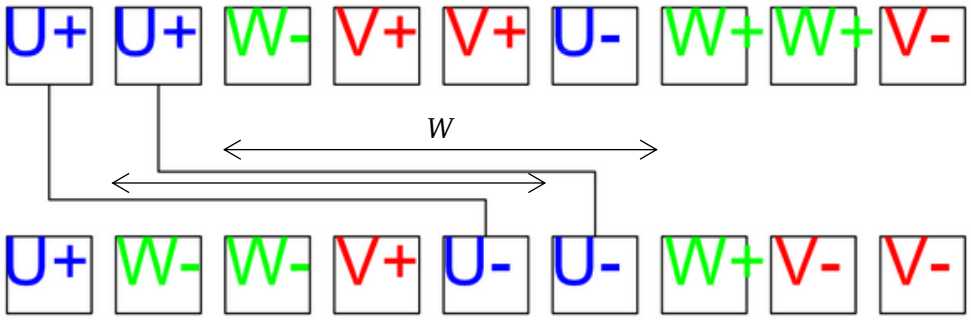

Figure 36: Slot coils sequence for a basic phasor diagram which corresponds to 9 stator slots.

The pole pitch is $\tau_{\mathrm{p}} = \frac{Q^*}{2p^*} = \frac{9}{2} = 4.5$ and the coil span is $W = 4$ as the distribution sequence shows in Figure 36.

When the calculation of the winding is done and since the analytical calculation is for a fractional slot motor, the formulas for calculating the winding factor are taken from the section 2.4.5 for the case of a fractional slot distributed winding. The pitch factor, distribution factor and winding factor are calculated in equations 3.3-7, 3.3-8 and 3.3-9 respectively. The parameters q_1, q_2, α_{u} and Y are calculated in Table 7, from the theory in section 2.4.5, since Q^* is and odd number.

Table 7: Calculated parameters for the pitch and distribution factors.

q_1	2
q_2	1
α_{u}	40°
Y	10

$$k_{\mathrm{p},1} = \sin\left(\frac{1 \cdot W}{\tau_p} \cdot \frac{\pi}{2}\right) = 0.9848 \tag{3.3-7}$$

$$k_{\mathrm{d},1} = \frac{\sin(1 \cdot \alpha_{\mathrm{u}} \cdot Y \cdot q_1/2) - \cos(1 \cdot p^* \cdot \pi \cdot Y) \cdot \sin(1 \cdot \alpha_{\mathrm{u}} \cdot Y \cdot q_2/2)}{(q_1 + q_2) \cdot \sin(1 \cdot \alpha_{\mathrm{u}} \cdot Y/2)} = 0.9598 \tag{3.3-8}$$

$$k_{\mathrm{w},1} = k_{\mathrm{p},1} \cdot k_{\mathrm{d},1} = 0.9452 \tag{3.3-9}$$

The flux per pole Φ_{h} is also calculated, which is necessary for knowing the number of turns per phase. In this calculation another initial assumption is taken as the magnetic flux density in the air-gap. For the fundamental component amplitude it has a value of 1 T. This value is set up as maximum because the magnetic flux density in the stator teeth will be around 1.8 T, which is the limit due to the iron saturation:

$$\Phi_{\mathrm{h}} = \frac{2}{\pi} \cdot \tau_{\mathrm{p}} \cdot l_{\mathrm{Fe}} \cdot B_{\delta 1} = 4.334 \cdot 10^{-3}\ \mathrm{Wb} \tag{3.3-10}$$

In order to calculate the number of turns per phase N_s, the equation of the induced voltage per phase of an AC machine is taken and the induced voltage value is taken with a safety factor of 0.8 of the maximum phase voltage that the inverter can give. The frequency is calculated from the nominal speed requirements, which is $f = 208.35$ Hz.

$$N_s = \frac{V_h}{\sqrt{2} \cdot \pi \cdot f \cdot k_{w,1} \cdot \Phi_h} = 25.44 \tag{3.3-11}$$

The number of turns per phase cannot be a fractional number; it has to be an integer number. Thus, there is the possibility to choose an integer number around 25. In this case, 26 turns give an induced voltage, which is too big. If 25 turns are chosen, it will be difficult to choose the number of turns per coil as it can be seen in equation 3.3-12. Hence, 24 turns per phase is selected. Thus, the number of turns per coil for a two-layer winding can be calculated with a selection of $a = 3$, which is the number of parallel branches of winding in AC machines:

$$N_c = \frac{N_s \cdot a}{2 \cdot p \cdot q} = 8 \tag{3.3-12}$$

The current loading value A_s, which is needed for the calculation of the current phase I_s, can be calculated from *Esson´s* number 2.13-1, where $\hat{A} = \sqrt{2} \cdot k_{w,1} \cdot A_s$:

$$A_s = \frac{C}{\frac{\pi^2}{\sqrt{2}} \cdot k_{w,1} \cdot B_{\delta 1}} = 45674 \text{ A/m} \tag{3.3-13}$$

$$I_s = \frac{A_s \cdot d_{si} \cdot \pi}{2 \cdot m \cdot N_s} = 92.47 \text{ A} \tag{3.3-14}$$

The current loading and the phase current as well as other thermal parameters such as current density and current per coil are used to calculate the area of copper per coil. Thus, the current density J is calculated using the thermal utilization selected for this motor as $A_s \cdot J = 5000$ (A/cm) ·(A/mm^2).

$$J = \frac{5000}{A_s} = 10.95 \text{ A/mm}^2 \tag{3.3-15}$$

Then the current coil and the copper area of a coil are calculated:

$$I_c = \frac{I_s}{a} = 30.84 \text{ A} \tag{3.3-16}$$

$$A_{Cu} = \frac{I_c}{J} = 2.82 \text{ mm}^2 \tag{3.3-17}$$

$$d_{Cu} = \sqrt{\frac{A_{Cu} \cdot 4}{\pi}} = 1.9 \text{ mm} \tag{3.3-18}$$

Since a coil with a copper diameter bigger than 1 mm is tough to wound in small electrical machines, it is considered to calculate parallel wires per turn a_i to make the wound easier. Thus, 6 parallel wires per turn are selected to use a nominal conductor diameter of 0.813 mm. Then the copper area is recalculated with equation 3.3-19.

$$A_{Cu} = \frac{4}{\pi} \cdot (a_i \cdot d_{Cu}) = 3.115 \text{ mm}^2 \tag{3.3-19}$$

The geometry of the stator core begins with the calculation of the teeth and slots dimensions. First of all the area of one stator slot, with a conservative fill factor of $k_f = 0.44$, is calculated as:

$$A_{Qs} = \frac{2 \cdot N_c \cdot A_{Cu}}{k_f} = 112.8 \text{ mm}^2 \tag{3.3-20}$$

Figure 37 shows the parameters of the stator slots, where the tooth breadth b_{st} and the slot height h_{sl} are calculated following the equations 3.3-21 and 3.3-22. The maximum magnetic flux that crosses a tooth $B_{st,max}$ is set up to be 1.8 T to avoid iron saturation and the stack fill factor k_{Fe} is 0.97.

$$B_{\delta 1} \cdot \tau_Q \cdot l_{Fe} = B_{st,max} \cdot b_{st,min} \cdot l_{Fe} \cdot k_{Fe} \qquad \rightarrow b_{st,min} = 6.2 \text{ mm} \tag{3.3-21}$$

$$A_{Qs} = \frac{b_{slu} + b_{slo}}{2} \cdot h_{sl} \qquad \rightarrow h_{sl} = 16.9 \text{ mm}^2 \tag{3.3-22}$$

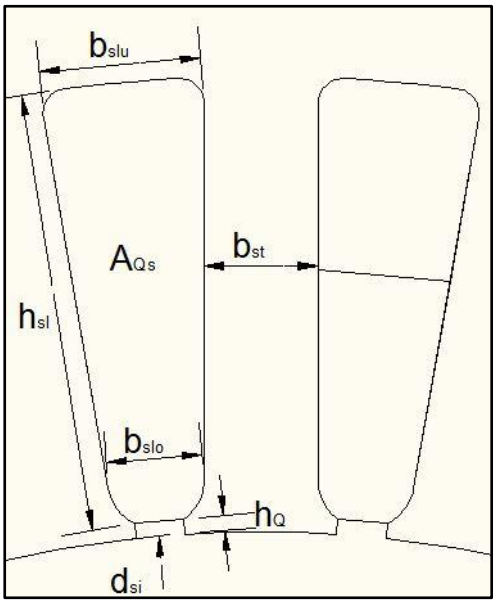

Figure 37: Stator slot parameters.

Finally, the stator yoke can be calculated as it is equal to half of the stator flux that crosses the yoke $\Phi_{ys,1}$ and the flux that comes from the air-gap and goes to the stator $\Phi_{ys,2}$, which both are the same. A parameter that takes into account the dispersed flux in the stator core is introduced $\sigma_s = 0.04$.

$$\Phi_{ys,1} = \frac{1}{2} \cdot \Phi_{\delta} \cdot (1 + \sigma_s) \tag{3.3-23}$$

$$\Phi_{ys,2} = B_{ys,max} \cdot h_{ys} \cdot l_{Fe} \cdot k_{Fe} \tag{3.3-24}$$

$$\Phi_{ys,1} = \Phi_{ys,2} \qquad \rightarrow h_{ys} = 10 \text{ mm} \tag{3.3-25}$$

The last calculations that are needed for the implementation of the designed motor to the FEM program are the resistance per phase R_s and the inductance in the winding overhangs $L_{\sigma b}$. Thus, the resistance is calculated for a work temperature of $\vartheta_{Cu} = 100$ °C with the equation (3.3-27 where some parameters are already calculated, the copper conductivity is $\kappa_{Cu} = 57{\cdot}10^6$ at 20 °C, the parallel wires per turn a_i are 6 and the winding overhang l_b is calculated with equation 3.3-28, where $l_a = 5$ mm is the clearing of main slot insulation and other additional length for bending the conductors in the winding overhangs.

$$R_s = k_{\vartheta} \cdot \frac{1}{\kappa_{Cu,20°C}} \cdot \frac{N_s \cdot 2 \cdot (l_{Fe} + l_b)}{a \cdot a_i \cdot A_{Cu}} = 0.0304\ \Omega \tag{3.3-26}$$

$$k_{\vartheta} = \frac{\vartheta_{Cu} + 235}{255} = 1.3138 \tag{3.3-27}$$

$$l_b = 1.3 \cdot W + 3 \cdot h_{sl} + 2 \cdot l_a = 116.73 \text{ mm} \tag{3.3-28}$$

The inductance in the winding overhangs $L_{\sigma b}$ is calculated with equation 3.3-30, where the leakage inductance coefficient in winding overhangs λ_b is calculated with equation 3.3-29.

$$\lambda_b = 0.075 \cdot \left(1 + \frac{l_b}{\tau_p}\right) = 0.23422 \tag{3.3-29}$$

$$L_{\sigma b} = \mu_0 \cdot N_s^2 \cdot \frac{2}{p} \cdot \lambda_b \cdot l_b = 13.2\ \mu\text{H} \tag{3.3-30}$$

In the present chapter, an analytical calculation of the IPMSM with fractional slot winding with $q = 1.5$ is done. Table 8 is presented with all the final values of the parameters for the studied machine. These values are needed for drawing the machine in the FEM program.
Since this thesis is going to compare machines with integer slot winding and machines with fractional slot winding, the machine from the Institute with $q = 2$ and an additional fractional slot winding machine with $q = 2.5$ have been calculated and implemented as FEM models. In addition, annexes 8.2 and 8.3 show two tables with all the calculated parameters for the models with $q = 2$ and $q = 2.5$. In both tables the initial requirements such as power, speed, torque, electromagnetic utilization, thermal utilization and inverter voltage are not written because all of them are the same for the three machines and these parameters have been discussed in section 3.1.

Table 8: Calculated parameters for the design of the IPMSM with fractional slot winding with $q = 1.5$.

IPMSM – $q = 1.5$			
Q	27	-	number of stator slots
q	1.5	-	number of slots per pole and phase
m	3	-	number of stator phases
p	3	-	number of pole pairs
δ	0.6	mm	air-gap length
d_{si}	92.8	mm	stator inner diameter
l_{Fe}	140	mm	iron stack length
τ_{p}	48.6	mm	pole pitch
W	43.2	mm	coil span
$k_{\mathrm{p,1}}$	0.9848	-	pitch factor
$k_{\mathrm{d,1}}$	0.9598	-	distribution factor
$k_{\mathrm{w,1}}$	0.9452	-	winding factor
N_{s}	24	-	number of turns per phase
N_{c}	8	-	number of turns per coil
a	3	-	number of parallel branches
a_{i}	6	-	number of parallel wires per turn
A_{s}	45674	A/m	current loading
I_{s}	92.47	A	phase current
J	10.95	$\mathrm{A/mm^2}$	current density
I_{c}	30.84	A	current coil
A_{Cu}	3.115	$\mathrm{mm^2}$	copper area of a coil
d_{Cu}	0.813	mm	copper diameter of a wire
A_{Qs}	112.8	$\mathrm{mm^2}$	area of a stator slot
k_{f}	0.44	-	fill factor
b_{st}	6.2	mm	breadth of a stator tooth
h_{sl}	16.9	mm	height of a slot
h_{ys}	10	mm	height of the stator yoke
R_{s}	30.4	mΩ	stator phase resistance at 100 °C
l_{b}	116.73	mm	winding overhang
$L_{\sigma\mathrm{b}}$	13.2	µH	inductance of the winding overhangs

4. FEM modelling

Before the real construction of this machine, an electromagnetic and mechanical analysis should be done with a computational program. This analysis save time and cost of manufacturing and it is useful to calculate and to check the parameters of the designed machines. For example, the post-processing of the electromagnetic analysis shows the magnetic flux density distribution in the air-gap and the cogging torque with the rotor position. Nowadays, the electromagnetic and mechanical analysis of electrical machines is carried out with programs that use finite element methods (FEM), which are also called finite element analysis (FEA).

For the present thesis, after theoretical knowledge and the analytical design of the IPMSM, an electromagnetic and mechanical analysis are carried out with the JMAG®-Designer 14.0 software from JSOL Corporation, which can simulate 2D and 3D models and it uses the *Maxwell* stress tensor method for several calculations which are presented in next chapter 5.

JMAG® is a friendly program that uses two main screens. The initial one, as it shows Figure 38 has a toolbox with material such as different types of iron, copper, aluminium and permanent magnets. It also has a project manager window with all the parameters of the different studies of the machine such as geometry, materials, conditions, circuit properties, mesh, results etc. An upper window is for the general tools of the program for simulations, rotating the views, and useful tools as contour plots, vector plots, flux lines and a graph manager to make *Fourier* analysis of the different electrical parameters. The screen, at the middle, shows the geometry of the machine which can be set with different colours for the different parts of the machine. The second important screen or function of JMAG® is the geometry editor, where a CAD of the machine that is desired to study can be drawn or modified. This screen has all the tools that a CAD program needs for a drawing.

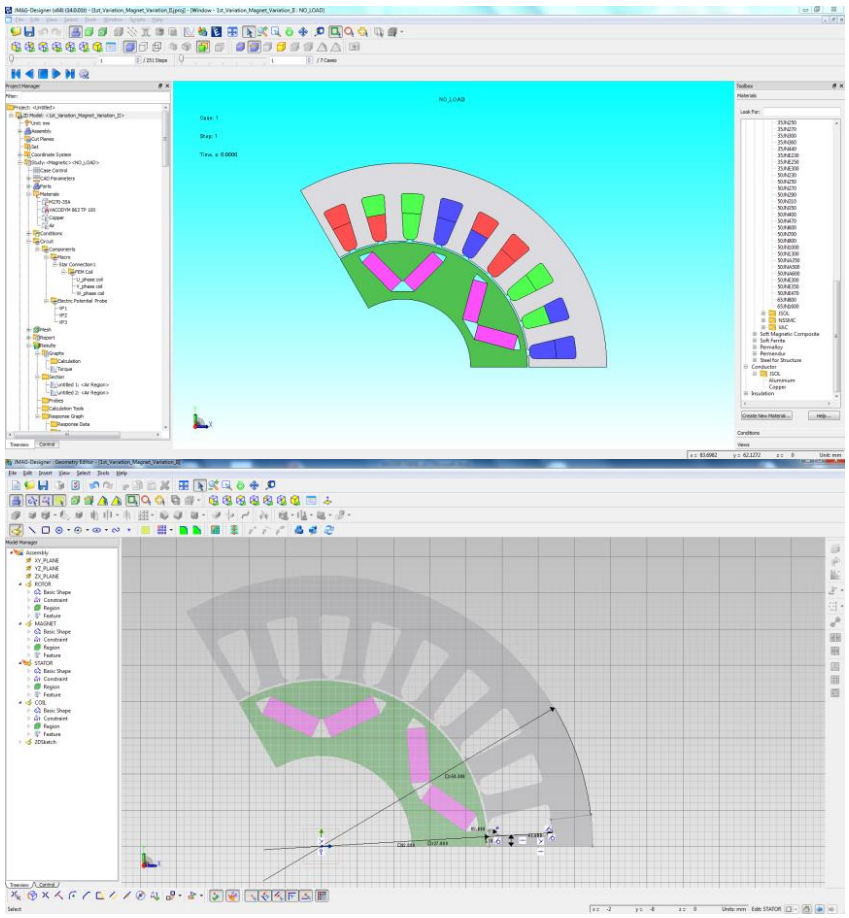

Figure 38: JMAG® screens. (Upper) is the project manager screen, (below) is the geometry editor for CAD.

4.1. Rotor core and V-shape magnets modelling

Since a comparison with the machine with an integer slot winding is going to be made with the new two machines with fractional slot windings, the geometry of the rotor core and the magnets dimensions for all motors are the same. Thus, with the dimensions calculated in section 3.3 and the geometry editor of JMAG®, the first drawings are made for the rotor core and the magnets in a V-shape disposition. It can be seen in Figure 39 the dimensions of the drawings for one pole pitch, which means that the machine has 6 poles and 12 magnets. JMAG® program does not need the drawing of the whole machine; it is enough with one or two pole pitches, depending of the stator structure, since the program can apply the symmetry condition for simulating the whole machine. JMAG® also allows the designer to draw half of a figure, as shows Figure 39, and then a mirror copy or a radial copy tool can be used to copy the second half of the figure. Thus, the drawing is easy and fast.

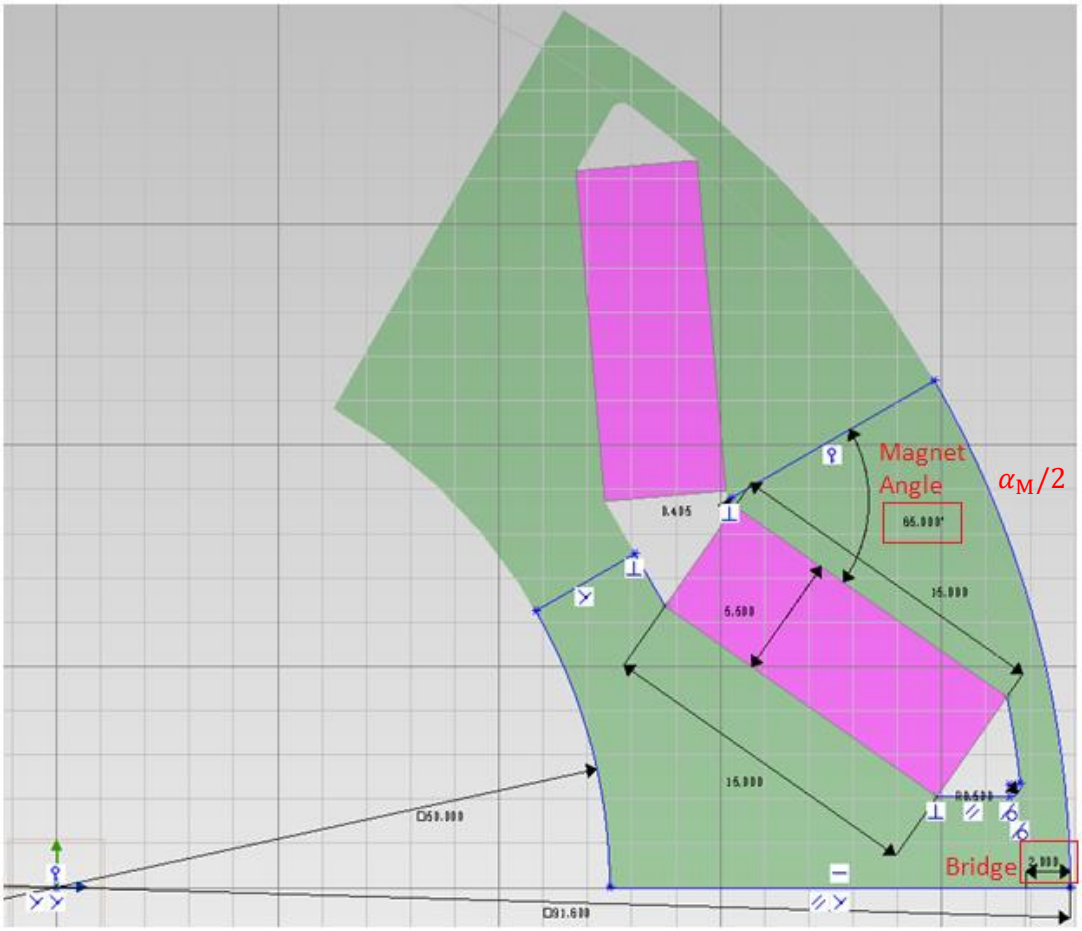

Figure 39: Drawings of the rotor core (green) and V-shape magnets (purple) with the geometry editor of JMAG® software.

The most remarkable parameters are the fixed height of the iron bridge of 2 mm and the variable angle between the magnets α_M, which in this case is 130°. The variation of the magnet angle is set up as half of it and programmed as a CAD variable, as it shows Figure 39. Thus, the angle can be modified directly from the project manager screen. The variation of this angle is another geometric parameter that this thesis looks for reducing the cogging torque and torque ripple. The 2 mm height of the iron bridge is set up as a fixed parameter, independently of the angle between the magnets. The iron bridge and the different centrifugal forces that act to the iron bridge for each variation of the magnet´s angle are shown in section 5.1.4.

4.2. Stator core and coils modelling

The stator core geometry changes from each machine as it is the main purpose of this thesis, from integer to fractional slot winding and each fractional slot machine with different number of stator slots. As the coils and stator dimensions have been calculated in section 3.3, the stator core for the main variation is drawn with $Q = 27$. As it can be seen in Figure 40, the stator core (yellow) has an inner diameter d_{si} of 92.8 mm and an outer diameter d_{so} of 150 mm. The coils (blue) are drawn with a two-layer configuration and the arrangement of the coils will set up in the project manager editor. Also the coils forms are designed with rounded corners for a better flux path.

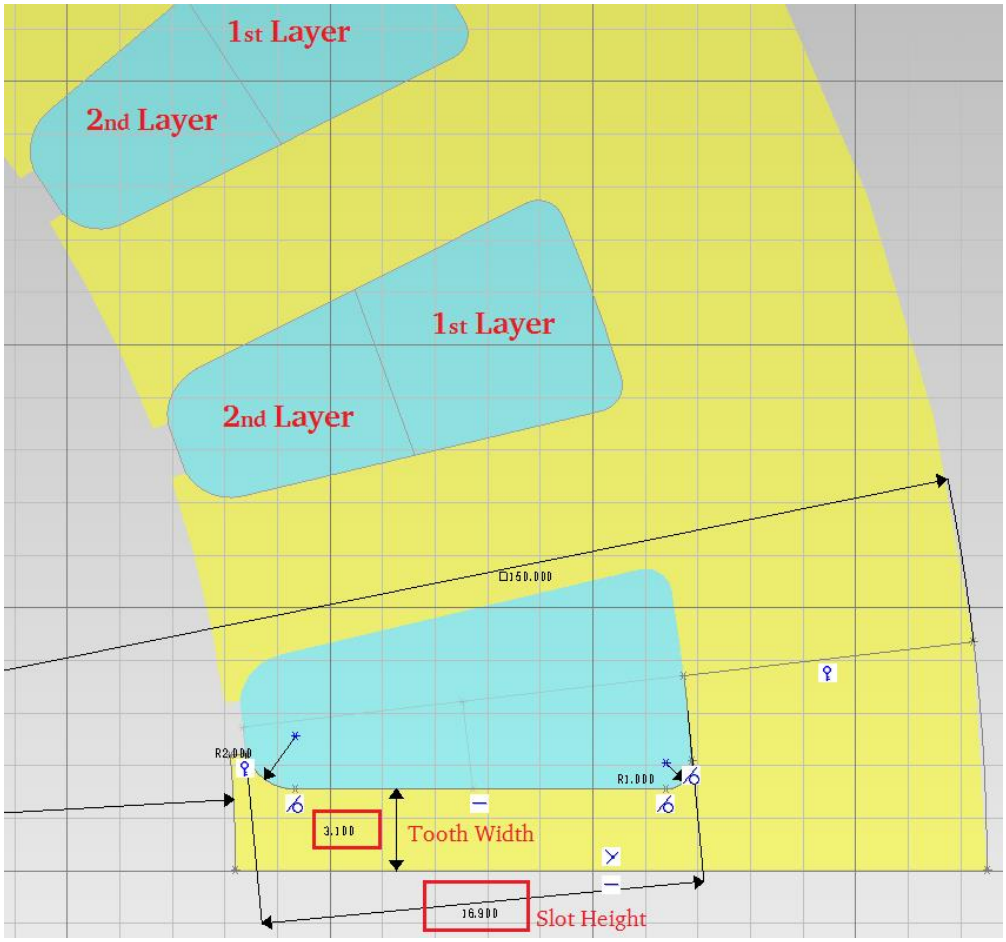

Figure 40: Drawings of the stator core (yellow) and coils (blue) with the geometry editor (CAD) of JMAG® software. This stator core belongs to a motor of $Q = 27$ and $q = 1.5$.

The most remarkable parameters in the drawing of the stator core are the slot height and the tooth width, which in Figure 40 the slot height is $h_{sl} = 16.9$ mm and the tooth width is $b_{st} = 3.1$ mm. Both parameters are also set up as CAD variables, whose values can be directly changed from the project manager screen. The slot geometry is also a design measure for the reduction of cogging torque and torque ripple. Thus, it is also important to find the best combination of slot height and tooth width, without varying the area of the stator slots A_{Qs}, which has been calculated previously. Furthermore, the fact that the stator core is varying, with the variation of the slots geometry, this directly affects the iron losses and hence a reduction of iron losses also is taken into account as well as the improvement of the efficiency. When the geometry of the motor is done, the drawing is saved and the project manager screen import the drawing from the geometry editor, then the geometry can be analysed with a new study case.

5. Electromagnetic analysis of the FEM model

After the design of the motor and the implementation of the model to the FE program, the electromagnetic and the mechanical analyses are carried out. The aim of this chapter is to comment about the simulation results of the proposed model for the cogging torque reduction, which is the distributed two-layer winding with $q = 1.5$ and $Q = 27$. The presented FEM model with JMAG® is shown in Figure 41 with the magnets (pink), rotor (green), stator (grey) and slots (green, red and blue). The stator slots colours represent the phases of each coil: blue for U-phase, red for V-phase and green for W-phase. In this case, the symmetrical phase distribution of the stator slots can be seen.

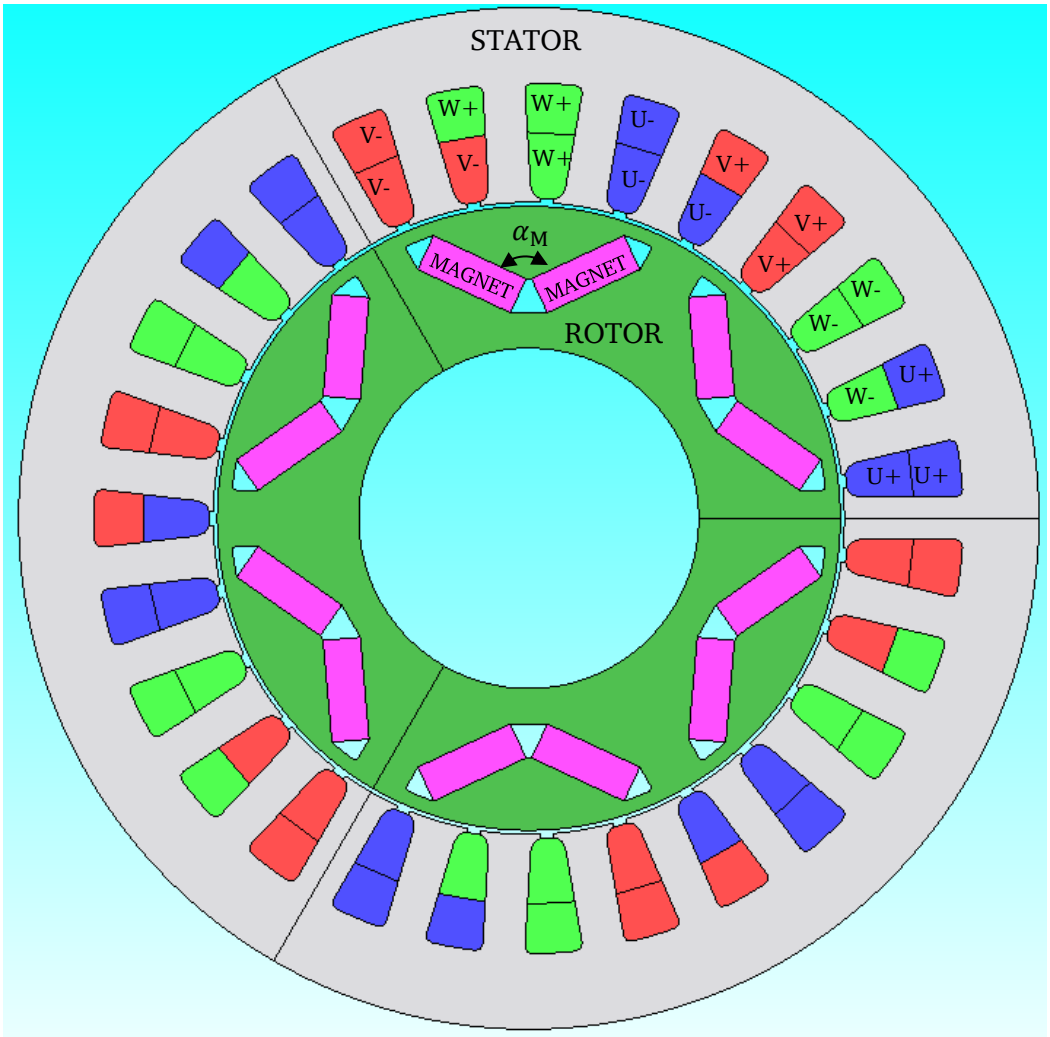

Figure 41: FEM model of an IPMSM with q = 1.5, Q = 27, m = 3 and p = 3. The main parts of the machine are displayed such as magnets (pink), rotor (green), stator (grey) and slots (green, red and blue).

5.1. Design of the model

The model has been implemented in JMAG® from the analytical calculations. In order to improve the reduction of the cogging torque, the magnets of the rotor and the slots of the stator have been optimized with suitable pole-arc to pole-pitch ratio and slots dimensions respectively. After the optimization of the rotor and the stator structures, the model has been tested with a mechanical stress calculation and a sudden short-circuit test. Finally, the simulation results of the optimized model are given for the no-load and load conditions of the motor.

5.1.1. Variation of the angle between magnets

Another method that has been used to reduce cogging torque and torque ripple is the selection of a suitable pole-arc to pole-pitch ratio. In this section the "pole-arc to pole-pitch ratio" will be discussed as the term "angle between magnets" α_M, this is the parameter which varies the mentioned ratio. For the present model, the angle α_M has been modified from 90° to 180° to achieve the less cogging torque and torque ripple. For each angle, the cogging torque, torque ripple and the efficiency have been calculated. The results are shown in Figure 42.

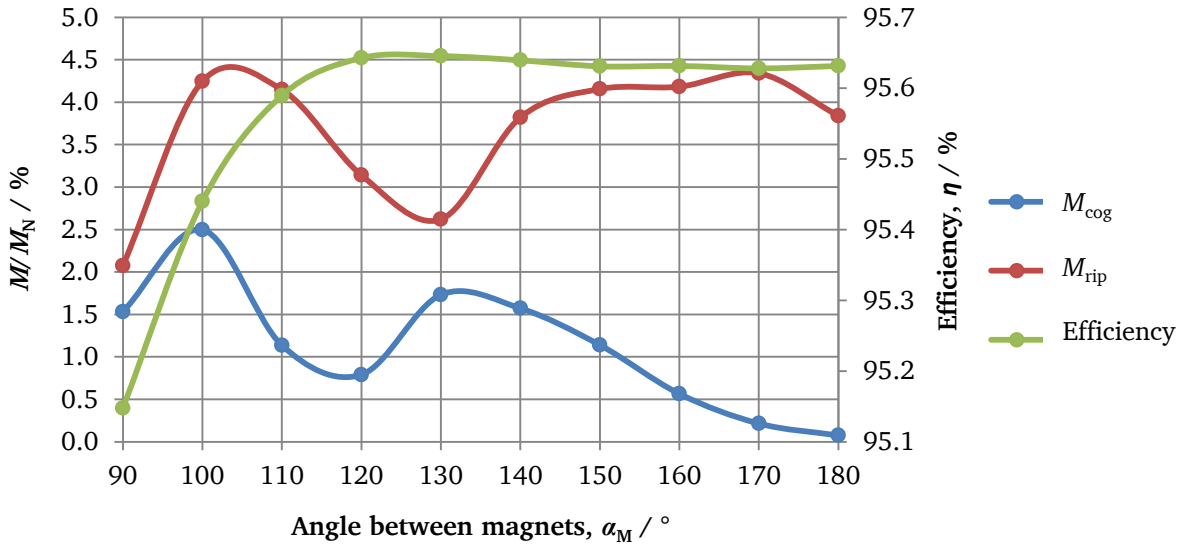

Figure 42: Variation of the angle between magnets α_M for the model q = 1.5 and calculated results of cogging torque, torque ripple and efficiency.

All simulations are carried out with rated operation, which is the rated torque M = 55 Nm and the rated speed n = 4167 min^{-1}.

Table 9: Calculated parameters for each variation of the angle between magnets for the model q = 1.5.

α_M	$\hat{B}_1$	I_s	β	M_N	L_d	L_q	$P_{Cu,dc}$	P_{Fe}	η
-	T	A	-	Nm	µH	µH	W	W	%
90°	0.822	94.4	30°	55.01	329	726	840	363	95.15
100°	0.823	90.9	32.5°	55.10	308	792	779	351	95.44
110°	0.819	88.8	33.5°	55.02	293	835	743	346	95.59
120°	0.813	88.2	34°	55.00	284	851	733	343	95.64
130°	0.805	88.4	34°	55.06	277	851	736	340	95.65
140°	0.797	88.6	34°	55.05	273	852	740	338	95.64
150°	0.791	88.7	34°	55.02	271	854	742	337	95.63
160°	0.786	88.8	34.5°	55.00	269	859	743	335	95.63
170°	0.782	89.0	34.5°	55.04	267	860	746	335	95.63
180°	0.780	89.1	34.5°	55.04	265	857	748	332	95.63

As it can be seen in Table 9, for cases of $\alpha_M = 90°$ and $\alpha_M = 100°$ the current is a little bit higher with respect to other cases, which contributes to an increase of ohmic losses. The inductance L_d is decreasing with higher values of angle between magnets and this allows a smaller field weakening operation. On the other hand, the saliency ratio L_q / L_d is increasing with higher angles and this contributes to a greater reluctance torque production.
From the simulations of different cases of α_M, the cases that give a higher efficiency and a better reduction of both cogging torque and torque ripple are the 120°, 130° and 140°. Although the cases of 160°, 170° and 180° give a bigger reduction of cogging torque, the torque ripple is considered to be too high with respect to other cases. Therefore, the case of 120° is selected as the suitable case, since it has good compromise between cogging torque and torque ripple reduction. The case of 130° could be also a candidate, although the reduction of cogging torque in 120° is 2.2 times the cogging torque in 130°.

5.1.2. Variation of the dimensions of the stator slots

The second geometric parameter that has been modified to achieve more reduction of cogging torque and torque ripple is the geometry of the stator slots. For the chosen angle between magnets of $\alpha_M = 120°$ and without changing the slot area A_{Qs}, the dimensions of the slot width and the slot height have been modified. The slot width has been varied from the CAD file varying the teeth width. Thus, the following Table 10 shows the values for the different combinations of teeth width and slot height. In addition, Figure 43 shows the cogging torque and torque ripple for each combination. The efficiency is not shown since there is no notable difference.

Table 10: Stator slots dimensions with the same slot area A_{Qs}. The parameters that vary are the teeth width b_{st} and the slot height h_{sl}.

Cases	1	2	3	4	5	6	7	8	9	10	11
Tooth width, b_{st} / mm	5	5.2	5.4	5.6	5.8	6.0	6.2	6.3	6.6	6.8	7.0
Slot height, h_{sl} / mm	14.7	15.1	15.4	15.7	16.1	16.5	16.9	17.2	17.7	18.1	18.5

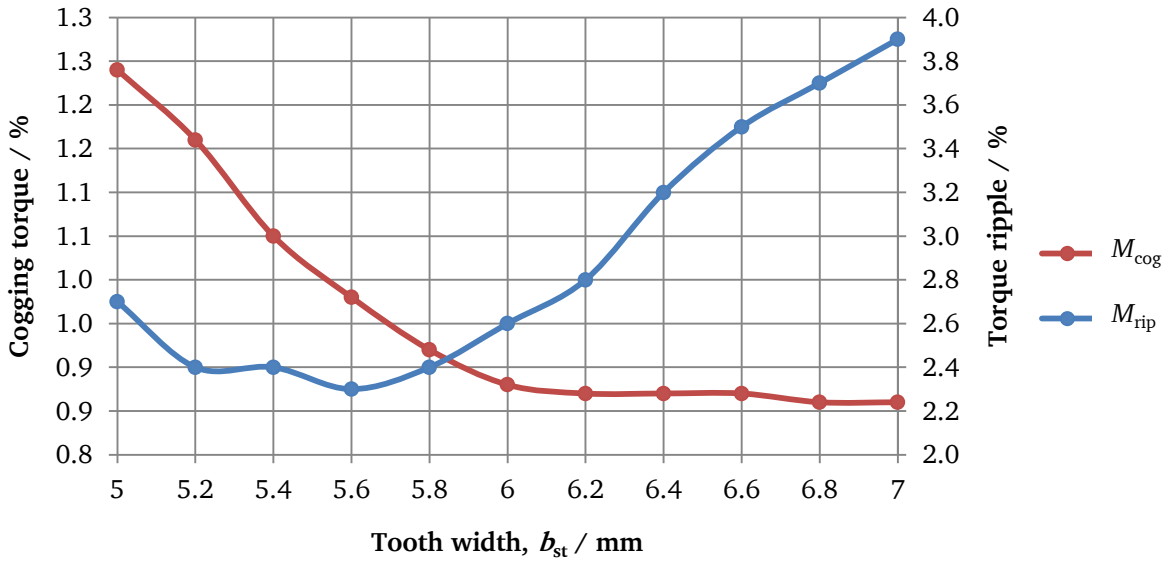

Figure 43: Cogging torque and torque ripple for each tooth width of the stator slots.

The Figure 43 shows clearly the dependence between the slot dimensions and the total amount of cogging torque and torque ripple. Figure 43 also shows that a reduction of the cogging torque does not mean a reduction of the torque ripple. It means that a compromise between both parameters should be chosen. For that, the case 5 with the stator slot dimensions of $b_{st} = 5.8$ mm and $h_{sl} = 16.1$ mm are selected.

5.1.3. Irreversible demagnetization of the magnets for a sudden short-circuit

The angle between magnets determines the area of the magnets exposed to irreversible demagnetization when there is a sudden short-circuit. For that, a three-phase sudden short-circuit simulation is carried out in order to check how much area of the magnets is going to be irreversible demagnetized. The simulation is carried out at no-load condition, for a temperature of 150° which decreases the coercive field strength. The calculations are made in the threshold of this temperature, which shows the irreversible demagnetization after crossing the knee point. As it can be seen in Figure 43, the sudden short-circuit happens at time 2.4 ms. The stator current raises and its field, which acts against the magnetic field of the magnets, causes the irreversible demagnetization to the magnets.

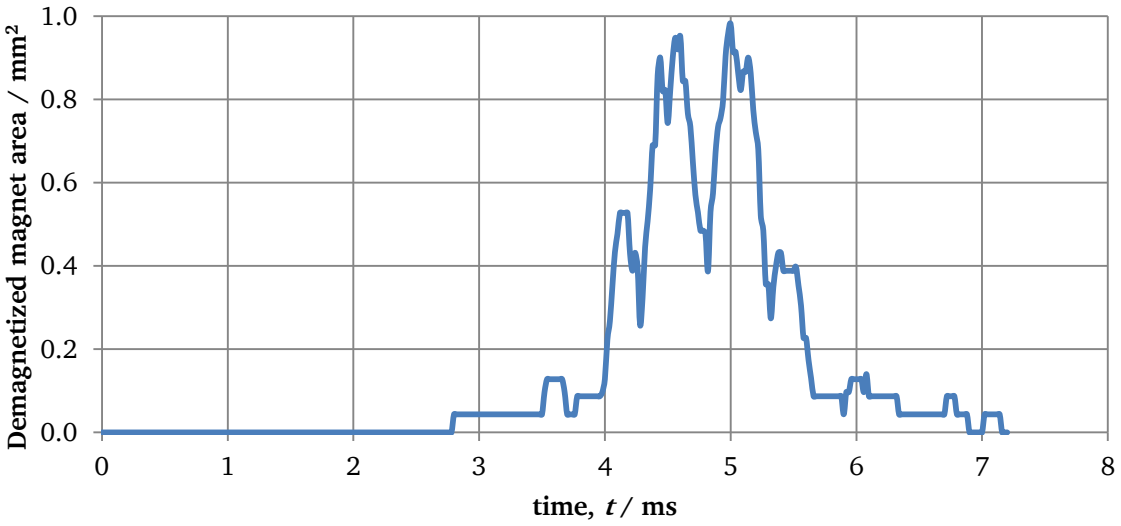

Figure 44: Magnetic field strength simulation for checking the demagnetized area of the magnets of 1 pole when a sudden short-circuit in the three phases is carried out.

The simulations are made for angles between the magnets α_M from 90° to 180°, thus a comparison between all of them can be done to find the optimum angle to avoid irreversible demagnetization of the magnets. In Figure 45, the calculation results of the demagnetized area are checked for the region above the threshold of 723 kA/m. The demagnetized area represents a percentage of the total area of 1 pole, equivalent to two magnets.
After the sudden short-circuit test, it can be seen from Figure 45, that the angle between magnets that is exposed to less irreversible demagnetized area is the case with $\alpha_M = 130°$. However, the already selected angle of 120° is also a good candidate for having few demagnetized area.

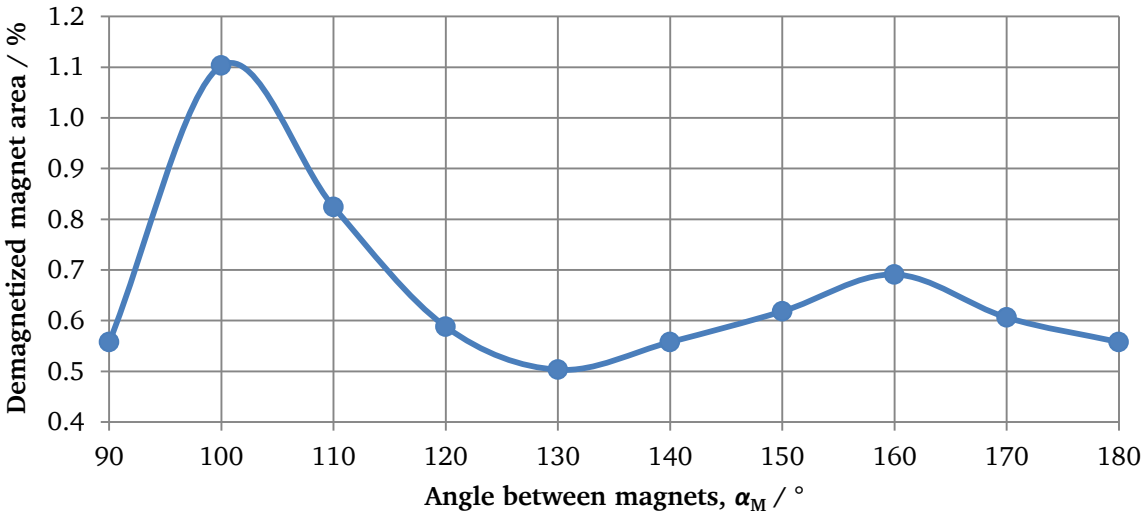

Figure 45: Percentage of demagnetized area of 1 pole, for a given angle between the magnets α_M.

5.1.4. Mechanical stress in iron bridges

For the verification of the mechanical stress that the iron bridges support caused by the centrifugal forces that the magnets produce when the rotor structure is rotating, an analytical calculation has been done with the theory from section 2.12 and also a FEM simulation has been calculated with JMAG®. The calculations and simulations have been carried out for different angles between magnets α_M, from 90° to 180°, with the rotational speed of n = 12000 min^{-1}, which is 1.2 times the maximum speed.
For the analytical calculation, the equivalent tangential stress that V-shape magnets produces onto the iron bridge have been multiplied by a factor of 2 to take into account an increased stress at the magnet edges. Furthermore, the tensile strength value of the iron sheets has been divided for a factor by 2 consider the lifetime cycles caused by fatigue. For that, Figure 46 shows half of the tensile strength (red) with a value of 254.25 N/mm^2 and the corresponding double value of the tangential stress in iron bridges (blue) for each angle between the magnets.

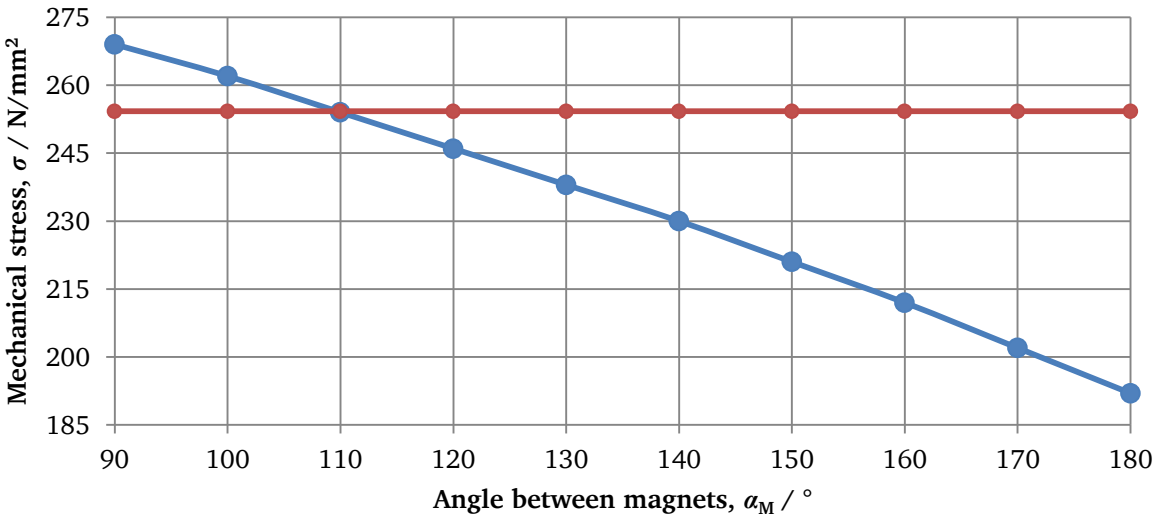

Figure 46: The calculated tangential stress (blue) on the iron bridge due to the centrifugal forces of the magnets for a given angle between magnets and half of the tensile strength (red) of the iron sheets SURA®, material M270-35A.

From the mechanical stress calculation in Figure 46, it can be seen that the angles between magnets that cannot be chosen since the iron bridge could break due to the centrifugal forces, are 90° and 100°. In addition, the case of 110° is also discarded since it is at the limit of the safety value of tensile strength. A simulation of the mechanical stress that the iron bridge suffers is carried out, for the selected angle between magnets of 120°. As it can be seen in Figure 47, the mechanical stress along the iron bridge is under the limit of half of the tensile strength of 254.25 N/mm^2. However, the inner part of the iron bridge which is in red colour surpasses the limit of 254.25 N/mm^2. This area is considered small enough to not have a significant effect on the iron bridge structure, since the tensile strength limit has a safety factor of 2.

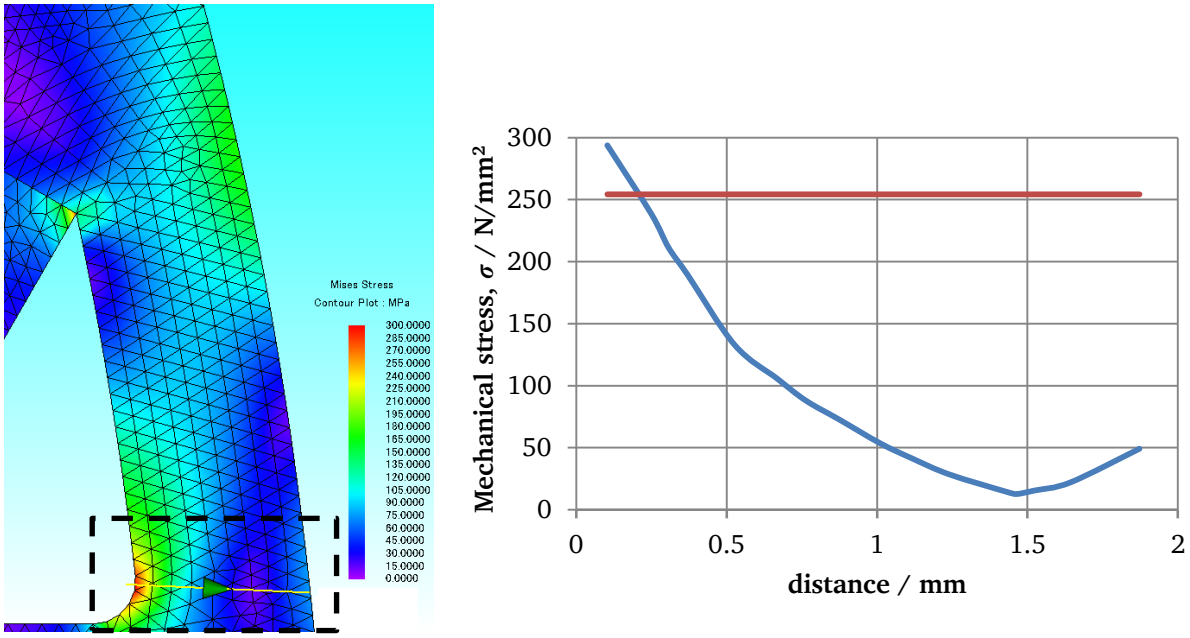

Figure 47: Mises Stress simulation for checking the iron bridge strength due to centrifugal forces at n = 12000 min^{-1} (left). Comparison of the Mises Stress simulated, at n = 12000 min^{-1} and α_M = 120°, and the limit of half of the maximum tensile strength that the material can support (right).

The designed and studied model of the IPMSM with two-layer and distributed windings with $q = 1.5$ and $Q = 27$ has been improved with FEA, from the analytical calculation of the motor. Finally, the selected parameters are; an angle between magnets of $\alpha_M = 120°$ and a stator slot dimensions of $b_{st} = 5.8$ mm and $h_{sl} = 16.1$ mm. These rotor and stator parameters improve the reduction of cogging torque and torque ripple. Now, the final IPMSM model is done and the simulations and results of it can be discussed.

5.2. Results of the electromagnetic calculation of the machine at no-load condition

5.2.1. Magnetic flux density distribution

At no-load condition of the motor and hence no-load circuit parameters, a 2D simulation of the magnetic flux density provided by the permanent magnets is generated to show the flux distribution around the stator and rotor cores. This simulation verifies that no saturation parts are in the machine and the flux lines goes from a north pole to a south pole of the magnets. The results are displayed with a contour plot that shows the magnetic flux distribution with a colour scale and the flux lines that show the magnetic lines through the machine. In Figure 48 it can be seen that the most critical parts of the machine are the iron bridges, where more flux concentrates since it is easier to close the flux path to the same magnet than crossing the air-gap, with values between 2-2.3 T. The iron bridges are built so thin to reduce the flux leakage from the magnets. Other parts that are critical are the stator teeth, which in this case they show a value of 1.2 T.

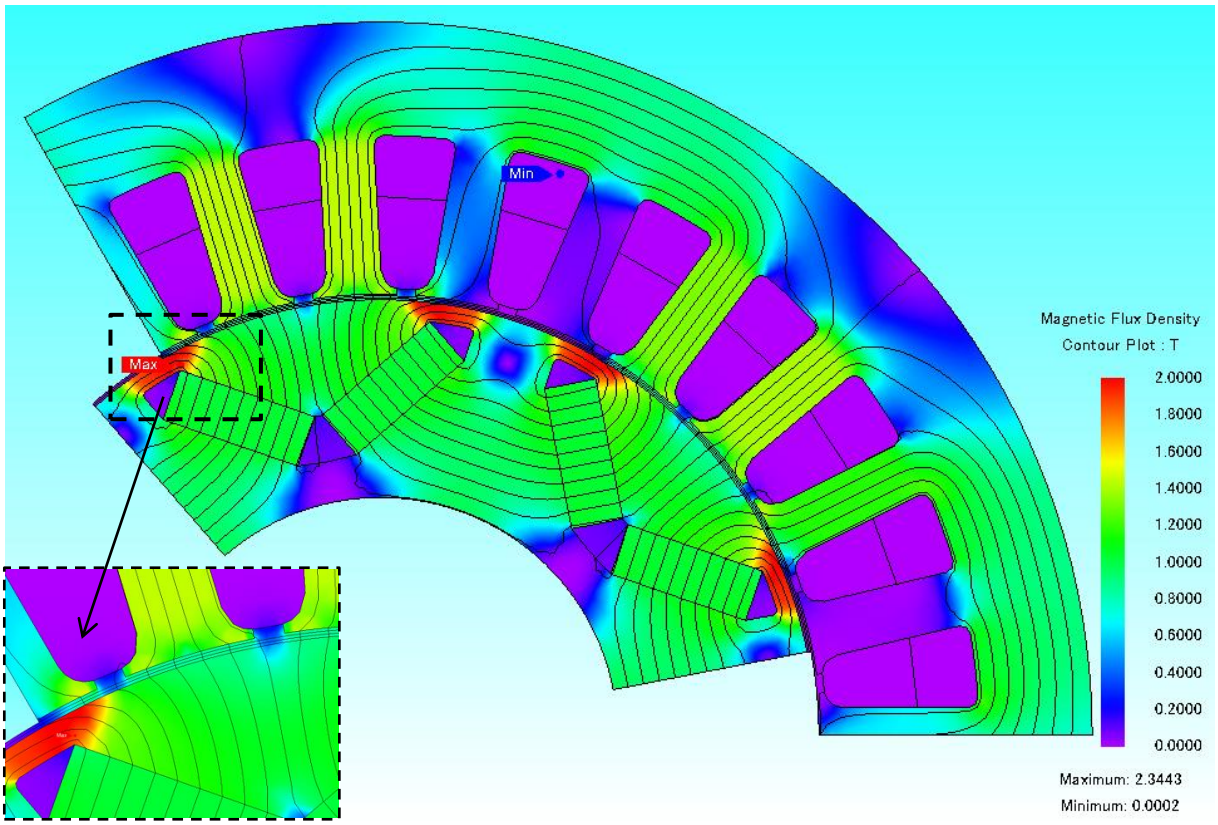

Figure 48: Magnetic flux density distribution thought the stator and rotor cores at no-load condition.

In order to check the shape of the function of the magnetic flux density distribution in the air-gap, an arc section through the air region in the middle of the air-gap is carried out and the radial component of the magnetic flux density is displayed in Figure 49. The magnetic flux density in the air-gap for one electrical period is the superposition of all the magnetic flux waves for all harmonics, which arise from distortions. Furthermore, the influence of the slot opening effect can be seen as well. Thus the stator slots have to be chosen with a small slot opening. In the present model a rather small slot opening of 2 mm was chosen. Since the model is for a fractional slot winding $q = 1.5$, it causes an asymmetry of the magnetic flux density in the x-axis and hence even harmonics orders appear. In addition, the fundamental component of the magnetic flux density is also displayed in the same graph using the FFT, in order to compare both functions and see how sinusoidal is the magnetic flux density in the

air-gap compared to its fundamental component. The fundamental component of the magnetic flux density distribution has a peak value of $\hat{B}_{\delta 1} = 0.81$ T.

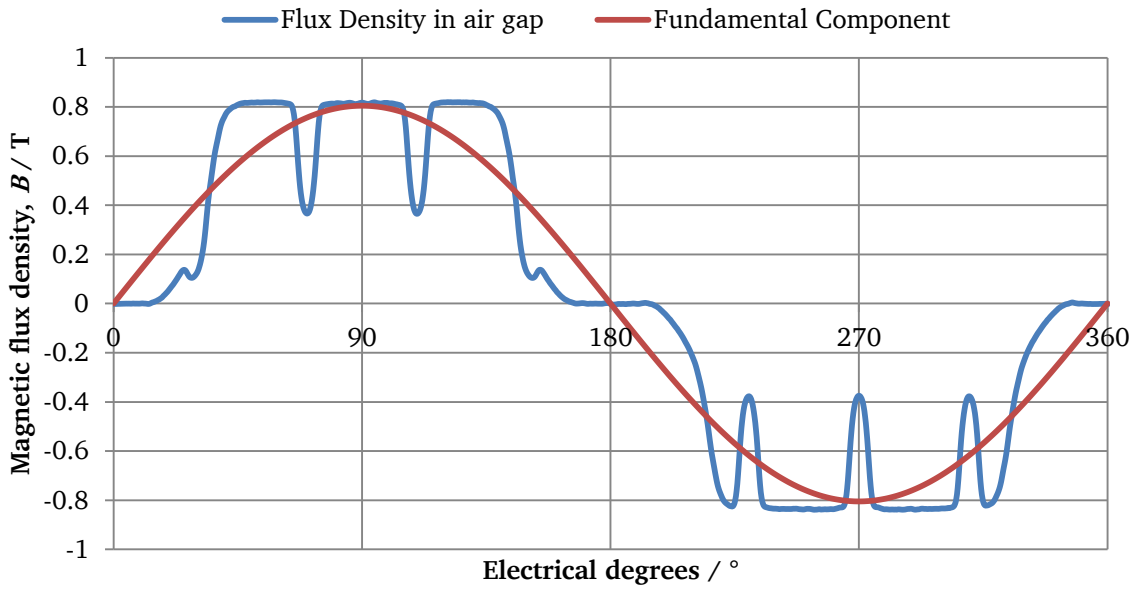

Figure 49: The radial component of the magnetic flux density (blue) and the fundamental component (red) in the air-gap at no-load condition.

From the magnetic flux distribution, a *Fourier* analysis is carried out to see the harmonic content. The Figure 50 shows a zoom of the harmonic component of the magnetic flux density of the present model with $Q = 27$. Furthermore, a *Fourier* analysis of the same model without stator slots has been done to see the different harmonic components that appear when the slots are incorporate. It can be seen that with the slotless configuration only odd harmonic orders appear in the *Fourier* analysis, although in the presented model with $q = 1.5$ also even order harmonics appear.

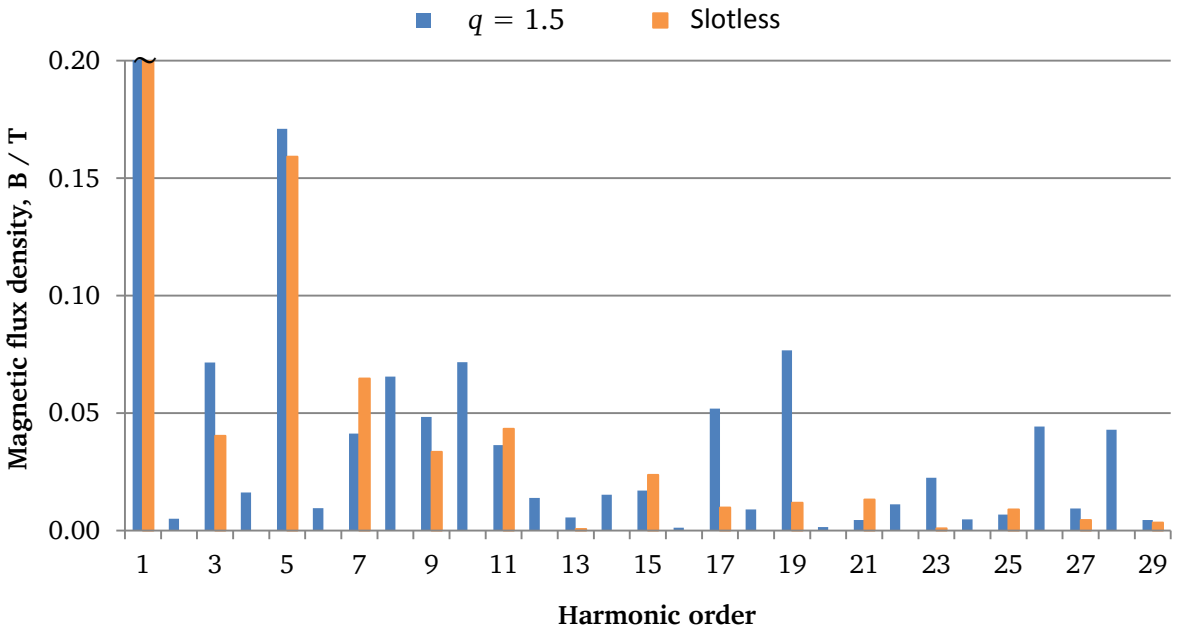

Figure 50: FFT of the magnetic flux density in the air-gap at no-load condition.

The harmonic components of the magnetic flux density in the air-gap due to the slot effect can be analytically calculated from equation 2.8-4, where the circumferential mechanical angle γ_m is transformed to electrical degrees. When this equation is considered for each rotor harmonics order μ, the harmonic components that appear in the magnetic flux density in the air-gap are deduced from $\mu \pm (Q \cdot l)/p$. For the present model of $Q = 27$ and $p = 3$, the harmonic components in the magnetic flux density in the air-gap are calculated in Table 11. The calculations are done with the parameter $l = 1$ and $l = 2$ to get the harmonic orders with biggest amplitudes. However, by increasing the l parameter more harmonics will appear, although their amplitudes will be smaller.

Table 11: Calculated harmonic orders of the magnetic flux density distribution in the air-gap from the interaction of the rotor harmonics orders μ and the stator slots Q.

rotor space harmonics	parameter	harmonic number	harmonic number
μ	l	$\lvert\mu - (Q \cdot l)/p\rvert$	$\lvert\mu + (Q \cdot l)/p\rvert$
1	1	8	10
	2	17	19
3	1	6	12
	2	15	21
5	1	4	14
	2	13	23
7	1	2	16
	2	11	25

5.2.2. Induced phase voltage

At no-load condition, the induced phase voltage is simulated. Since the induced phase voltage is proportional to the magnetic flux density $U_{p1} = \sqrt{2} \cdot f \cdot k_{w,1} \cdot N_s \cdot 2 \cdot \tau_p \cdot l_{Fe} \cdot B_{\delta 1}$, it can be seen in Figure 51 the sinusoidal waves of the voltage phases. However, it can be also noticed the slot opening effect on the top of the waves. The induced phase voltage waveforms are the sum of all harmonic components and the amplitude of the fundamental induced phase voltage is 103.3 V. Having a short pitched configuration of $W/\tau_p = 4/4.5$ introduces the pitch factor and having group of coils $q > 1$, which in this case is 1.5, introduces the distributed factor. Both factors give the winding factor which helps to reduce the amplitudes of the harmonic components and therefore the induced phase voltage is more sinusoidal. However, the amplitude of the fundamental component is also reduced.

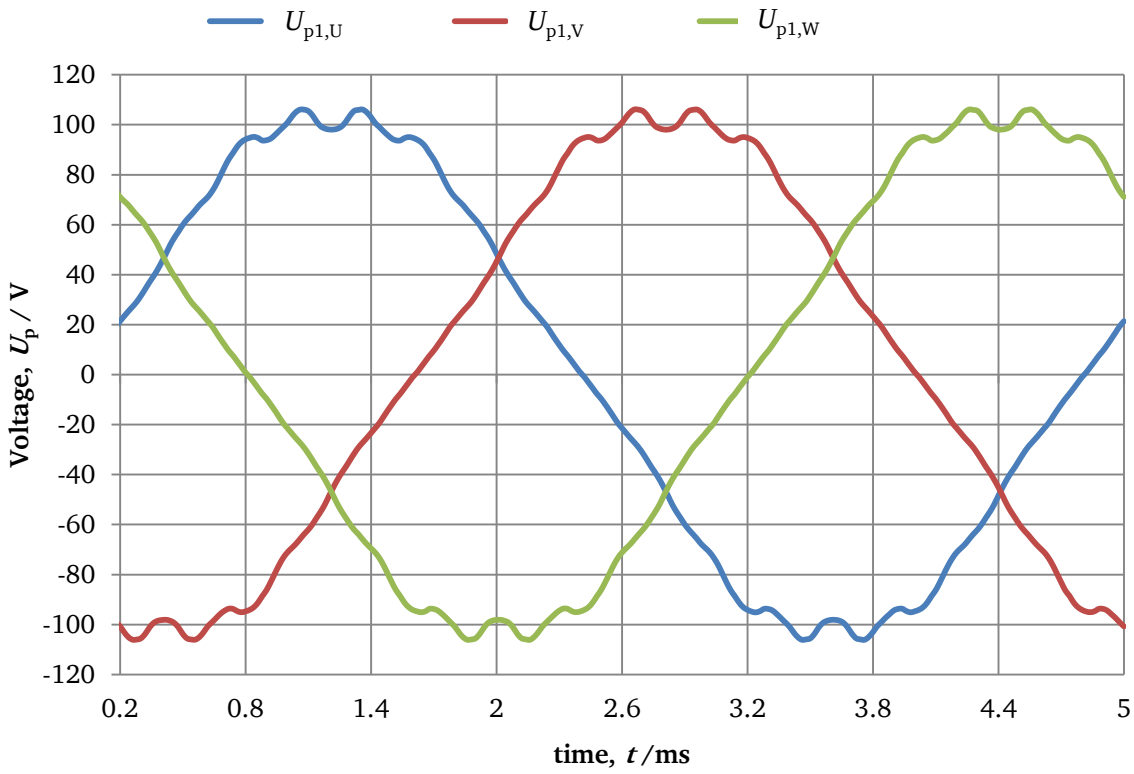

Figure 51: Induced phase voltage at no-load condition. Phase *U* (blue), phase *V* (red) and phase *W* (green).

5.2.3. Cogging torque

As it has been shown in sections 5.1.1 and 5.1.2, cogging torque is fully dependable on geometric parameters such the pole-arc to pole-pitch ratio and the dimensions of the stator slots. The simulations results of the cogging torque gives a peak value of 0.47 Nm and a percentage of the peak value of cogging torque of 0.85 %, from the rated torque of 55 Nm.
The periodicity of the cogging torque, that the Figure 52 shows can be analytically calculated as in theory 2.6 has been explained. Thus, for the present model of $Q = 27$ and $p = 3$, the periodicity of the cogging torque for one slot pitch is:

$$N_{\text{period}} = \frac{2p}{\text{GCD}\,\{Q, 2p\}} = \frac{6}{3} = 2 \tag{5.2-1}$$

The total number of cogging torque periods for one circumferential rotation of the rotor is 54, since there are 27 stator slots and each slot pitch τ_Q has 2 periods. The analytical calculation is verified with the simulation of Figure 52, which shows that for 360° electrical degrees there are 18 cogging torque periods and hence for 360° mechanical degrees there are 54 periods.

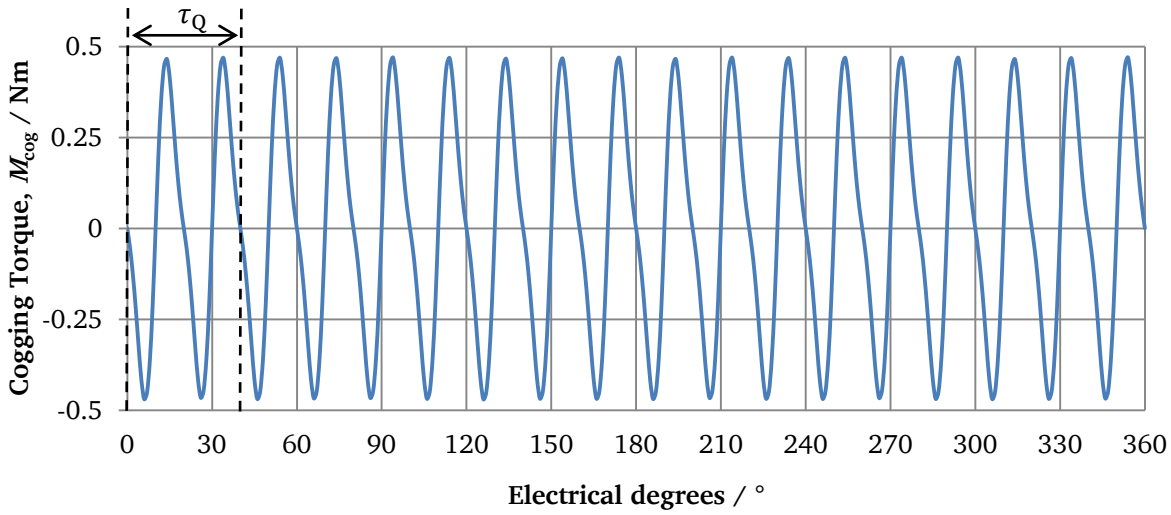

Figure 52: At no-load condition, simulation of the cogging torque M_{cog} for one electrical period T.

The *Fourier* analysis of the cogging torque is carried out with JMAG®. As it can be seen in Figure 53, the harmonic components that are more significant are the 18th and the 36th. The main harmonic 18th coincide with 18 cogging periods N_{period} that the cogging torque shows in one electrical period.

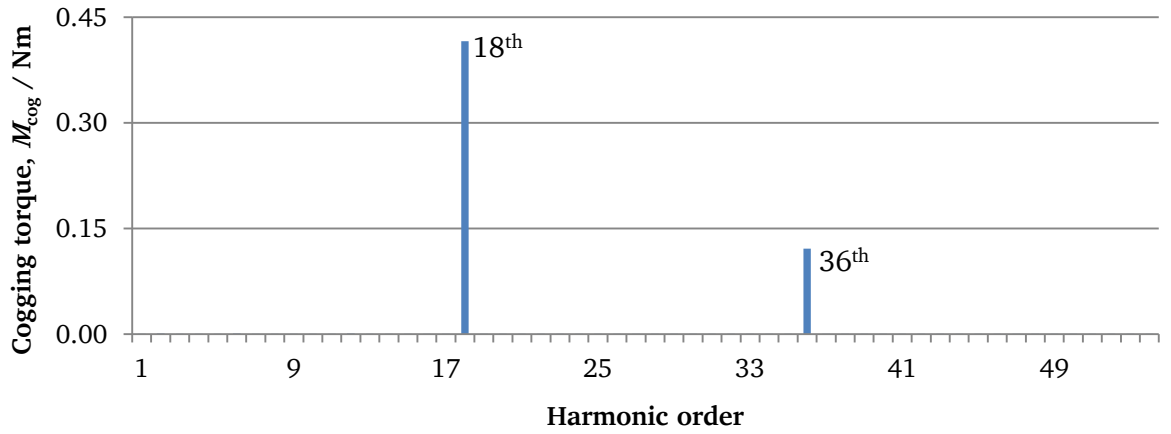

Figure 53: *Fourier* analysis of the cogging torque.

The harmonic orders that appear in the *Fourier* analysis of the cogging torque can be analytically calculated from theory 2.8.5. A table with the values of the most important harmonics orders and the parameters needed for calculating them are shown in Table 12. In addition, the peak value and the electrical frequency of each harmonic are also added from the *Fourier* analysis.

Table 12: Harmonic content of the cogging torque for q = 1.5. The parameters l and k for the analytically calculation of the harmonics numbers are shown for each harmonic order as well as the amplitude.

l	k	harmonic order	$\widehat{M}_{cog}$ / Nm	frequency, f_l / Hz
2	9	18	0.42	3750
4	18	36	0.12	7500
6	27	54	0.003	11250
8	36	72	0.003	15001

5.3. Results of the electromagnetic calculation of the machine at rated load condition

5.3.1. Voltage and current

At rated load condition of the motor, the voltage phases and the current phases can be drawn after the FEM simulation. As it can be seen in Figure 54, the current phase *W* (green) shows a perfect sinusoidal shape since the inverter is considered to feed the motor without any current ripple or distortion. The amplitude of the fundamental phase current has a value of 126.51 A. The phase voltage *W* (green) shows a little distortion due to the harmonic components. A Fourier analysis has been carried out to obtain the amplitude of the fundamental component of the phase voltage. The peak value is 141.6 V with a frequency of 208.35 Hz.
The representation of the fundamental phase voltage in the same graph of the phase current is made to calculate the fundamental power factor of the motor. For that, as it can be seen in Figure 54, two black lines are shifted in the peak of the fundamental phase voltage and the phase current. From both peak values, the times are read. The difference between these two times can be converted to degrees since one electrical period is equivalent to 360° or $1/f$ with equation 5.3-1. Finally, the power factor can be obtained with equation 5.3-2:

$$\varphi_1 = \Delta t \cdot f \cdot 360° \tag{5.3-1}$$

$$\text{Power Factor} \rightarrow \cos\varphi_1 \tag{5.3-2}$$

The time difference between the peak amplitudes is 0.31 ms, the frequency is 208.35 Hz and the power factor result is 0.93.

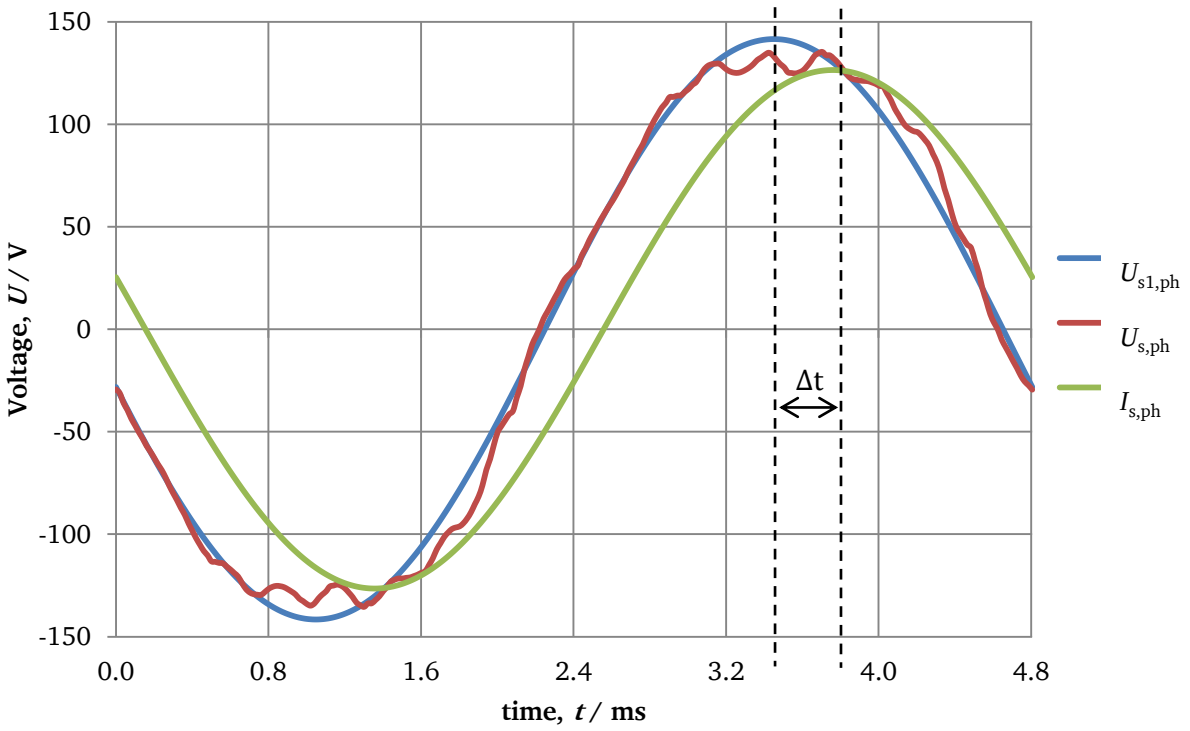

Figure 54: For one electrical period, the phase voltage *W* (red), the phase current *W* (green) and the fundamental component of the phase voltage *W* (blue) are displayed.

5.3.2. Torque ripple and torque production with MTPA

At the rated load condition, where a constant torque is desired, the torque ripple percentage of 2.45 % has been calculated from the time graph of Figure 55 where the average torque is 55.14 Nm.

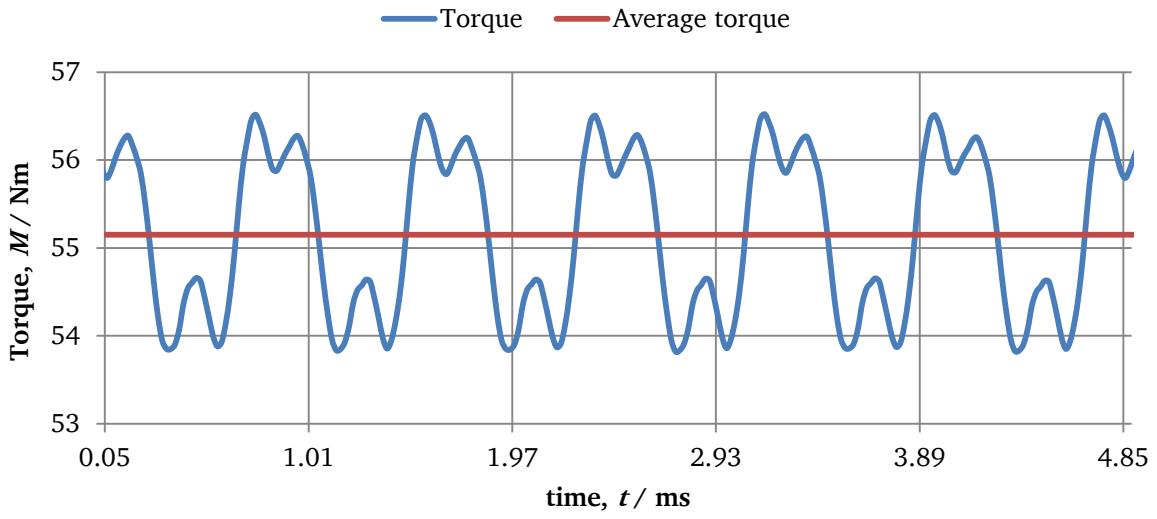

Figure 55: Torque response of the IPMSM q = 1.5 model for the rated load condition. It can be seen the torque response (blue) and the average torque (red).

At rated load condition as well, four different currents has been simulated for different current angles β. The angles changes from 0° to -90°. For a given phase current, there is a current angle that gives a maximum torque since the IPMSM has a saliency ratio which gives an extra reluctance torque. For that reason, the optimal current angle has to be found for each stator current in order to have maximum torque production and minimum ohmic losses. The control technique that finds the optimal current angle is known as the maximum torque per ampere technique (MTPA).

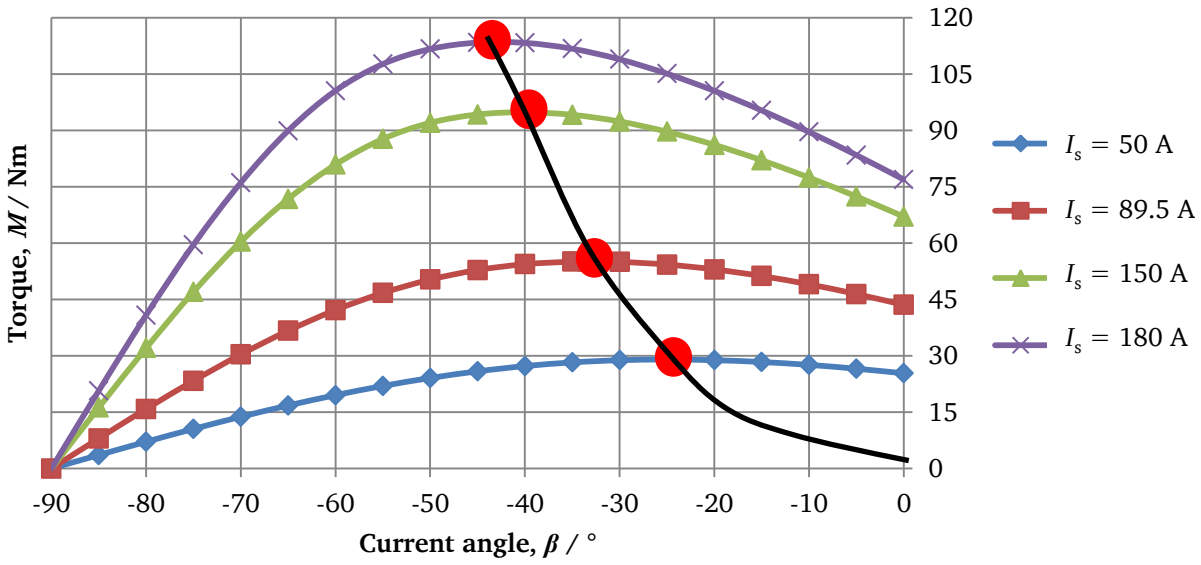

Figure 56: Torque curve depending on the phase current and the current angle at rated speed n = 4167 min^{-1}. MTPA technique finds the maximum torque M for a given stator current I_s by finding the optimal current angle β.

For the OP2 with a stator phase current of 89.5 A, the optimal current angle is -33.4° for a maximum torque of 55.14 Nm. For each current of Figure 56, a comparison between the torque generated at current angle $\beta = 0°$ and when the angle is for maximum torque is done in Table 13, in order to see how much extra percentage of torque can be achieved when a suitable current angle from MTPA technic is chosen. This extra torque is the reluctance torque that the machine generates by having the saliency ratio.

Table 13: For a given stator current I_s, the variation of produced torque between current angle β at 0° and the angle which gives maximum torque.

Phase current, I_s	Torque at $\beta = 0°$	Maximum torque	β for maximum torque	Variation
A	Nm	Nm	°	%
50	25.35	29.02	-25.0	+14.48
89.5	43.58	55.14	-33.4	+26.53
150	67.07	94.85	-40.0	+42.42
180	76.93	113.38	-45.0	+47.38

5.3.3. Calculated parameters of q = 1.5 model

For each operational point, the calculated parameters of the proposed model have been taken from the simulation results and some of them have been calculated in the post-processing. The rotor speed n and the frequency f are basic parameters introduced to the JMAG®, the induced voltage U_{p1} is a parameter simulated at no-load condition for the different frequencies which operates each operational point. At load condition, torque ripple M_{rip} has been calculated from the torque graph, the fundamental phase voltage U_{s1} and current I_{s1} are simulated for the suitable current phase β. The phase current in d and q axes are calculated with equations:

$$I_{sd} = I_{s1} \cdot \sin\beta \tag{5.3-3}$$

$$I_{sq} = I_{s1} \cdot \cos\beta \tag{5.3-4}$$

The fundamental power factor $\cos\varphi$ is the angle difference between the fundamental peak values of the phase voltage and the phase current. Finally, the inductances in d and q axes have been calculated applying the dq reference equations from 2.10-1.

$$L_d = \frac{(U_{sq} - U_{p0} - R \cdot I_{sq})}{\omega \cdot I_{sd}} \tag{5.3-5}$$

$$L_q = -\frac{(U_{sd} - R \cdot I_{sd})}{\omega \cdot I_{sq}} \tag{5.3-6}$$

Table 14: Calculated parameters of q = 1.5 model for each operational point.

	units	OP1	OP2	OP3
Speed, n	min^{-1}	4167	4167	10000
Frequency, f	Hz	208.35	208.35	500
Induced phase voltage, U_{p1}	V	73	73	175
Torque, M	N·m	110.7	55.14	46
Torque ripple, M_{rip}	%	1.66	2.45	9.4
Fundamental phase voltage, U_{s1}	V	114.2	100.2	123.6
Fundamental phase current, I_{s1}	A	175.4	89.5	135.7
Current phase, β	°	-42.5	-33.4	-72.9
Phase current of d-axis component, I_{sd}	A	-118.5	-49.3	-129.7
Phase current of q-axis component, I_{sq}	A	129.3	74.7	39.9
Fundamental power factor, $\cos\varphi$	-	0.862	0.93	0.995
Stator winding self-inductance of d-axis per phase, L_d	µH	280	275	373
Stator winding self-inductance of q-axis per phase, L_q	µH	624	824	935

The different losses explained in the theory section 2.13, have been calculated for each operational point of the motor. In addition, as mentioned before, only iron, ohmic and friction losses have been considered to calculate the mechanical and electrical power and the efficiency for each operational point. Introducing to JMAG® the iron losses density of the material for different frequencies, the FE program calculates the eddy current and hysteresis losses of the iron, and it gives the total value of the iron losses. The iron losses that JMAG® gives have been multiplied by a conservative coefficient of 1.5. This coefficient also involves the punching of the stator slots of the iron sheets, which damages the insulation between iron sheets and contributes to higher eddy current losses. For the ohmic losses calculation, which arise when the current crosses the conductor, a working temperature of 100 °C has been supposed. The DC ohmic losses have been calculated for the winding resistance per phase of 30.4 mΩ and the current phase of each operational point. Furthermore, the current displacement effect has been considered to have the AC ohmic losses and to see how much difference of ohmic losses is between operational points. The most remarkable parameter, which contributes to higher ohmic losses due to the current displacement, is the frequency. This phenomenon is explained since the penetration depth of the slot d_E is reduced with higher frequency $d_E \sim 1/\sqrt{f}$, and it decreases the effective copper area of the slot, giving higher copper losses. The friction losses are calculated in the air-gap and the only parameters that vary for this calculation from one OP to another is the speed of the rotor. Although the increased speed is 2.4 times, the friction loss has increased 12 times since the calculation of the friction losses $P_{d,fr} \sim n^3$.

The electrical power, which is supplied to the motor, can be calculated with the sum of the mechanical power and the total amount of losses. The mechanical power, which the motor needs for producing the net-work, has been calculated from the average torque that JMAG® gives, minus the iron and friction losses. The average torque that the FE program calculates, using the *Maxwell* stress tensor, is the torque in the air-gap and it does not consider the iron and friction losses. Finally, the efficiency of the motor for each operational point can be easily calculated with the mechanical and electrical power.

Table 15: Calculated results of the motor with q = 1.5 for each operational point.

	units	OP1	OP2	OP3
Temperature of the stator winding, ϑ_{Cu}	°C	100	100	100
Ohmic losses, $P_{d,Cu,dc}$	W	2806	731	1680
Ohmic losses by current displacement, $\Delta P_{d,Cu}$	W	17.5	4.6	60.4
Ohmic losses, $P_{d,Cu,ac}$	W	2824	736	1740
Iron losses, $P_{d,Fe}$	W	300	216	701
Iron losses with conservative factor 1.5, $P_{d,Fe}$	W	450	324	1052
Friction losses, $P_{d,fr}$	W	2.1	2.1	25.4
Total losses, $P_d = P_{d,Cu,ac} + P_{d,Fe} + P_{d,fr}$	W	3276	1062	2818
Mechanical power, P_m	kW	47.85	23.74	47.1
Electrical power, P_e	kW	51.1	24.8	49.9
Efficiency, η	%	93.6	95.7	94.4

5.3.4. Maximum torque for loss minimization

As section 5.3.2 shows, the control technic maximum torque per ampere (MTPA) tries to find the maximum torque that the motor can produce for a fixed current and by changing the current angle. There is another technic that tries to find the highest efficiency by minimizing the total losses for the maximum torque that the motor can achieve. This technique is called the maximum torque for loss minimization and tries to find the optimal point by adjusting the *d*-axis stator current [46].
In the present section, the maximum torque for loss minimization technique is applied for the rated load operational point (OP2) and for the maximum torque operational point (OP1). Two figures are going to be presented for each OP with a table which summarises the most suitable parameters to achieve the MTPA and the loss minimization.

5.3.4.1 – Maximum torque for loss minimization at the OP2

At the rated operational point with M_N = 55 Nm and n = 4167 min^{-1}, Figure 57 shows the efficiency η and the stator current I_s depending on the *d*-axis stator current I_{sd}. The blue line is the stator current depending on the *d*-axis stator current. All the points gives the rated torque M_N = 55 Nm, although there is one case which has the minimum stator current and hence minimum ohmic losses are expected as it can be seen in Figure 58. This case is found by using the MTPA technique and corresponds to I_{sd} = -48.8 A. However, when all the losses of the machine are considered, there is one *d*-axis stator current that gives the rated torque with the highest efficiency, which is I_{sd} = -55.1 A, as the red line shows in Figure 57. The technique which finds the maximum torque for the minimum total losses is called the maximum torque for losses minimization. In addition, Table 16 shows the main parameters of the optimal point that gives the rated torque by using the MTPA technique and the optimal point that gives the rated torque and minimum losses by using the maximum torque per losses minimization (MTPLM). As it can be seen in Figure 58 the ohmic losses $P_{d,Cu,ac}$ shows the same shape like the stator current I_s in Figure 57 since $P_{Cu} \sim I_s^2$. Also in Figure 58 the iron losses $P_{d,Fe}$ decrease when the negative *d*-axis stator current I_{sd} increase. That happens since the introduction of a negative *d* current reduces the magnetic flux in the stator and hence the iron losses.

Table 16: At the operational point for the rated torque M_N = 55 Nm; calculated parameters for the optimal points of MTPA and Loss Minimization techniques.

	I_{sd}	I_s	β	M_N	$P_{d,Cu,ac}$	$P_{d,Fe}$	P_d	P_m	P_e	η
	A	A	-	Nm	W	W	W	kW	kW	%
MTPA	-48.8	89.2	33.2°	55	730	324	1056	23.7	24.73	95.73
MTPLM	-55.1	89.6	37.2°	55	739	307	1049	23.7	24.74	95.76

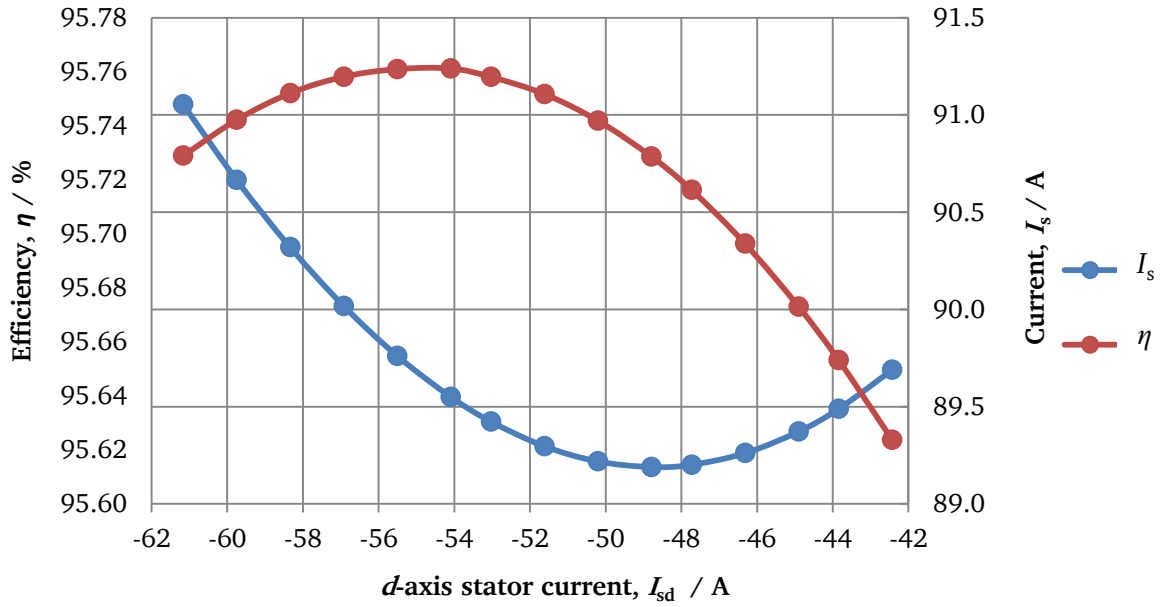

Figure 57: At the rated operational point; efficiency η and stator current I_s depending on the *d*-axis stator current I_{sd}.

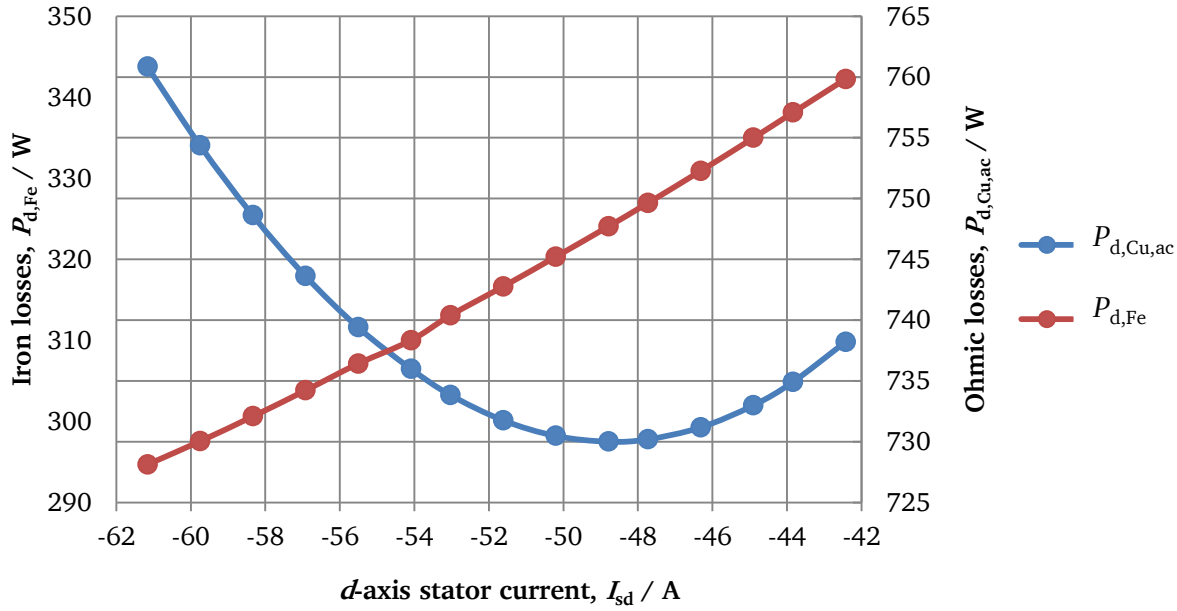

Figure 58: At the rated operational point; iron losses $P_{d,Fe}$ and ohmic losses $P_{d,Cu,ac}$ depending on the d-axis stator current I_{sd}.

5.3.4.2 – Maximum torque for loss minimization at the OP1

At the operational point 1, for a maximum torque of the motor M_{max} = 110 Nm at the rated speed n = 4167 min^{-1}, the calculated parameters for the optimal points of MTPA and MTPLM are shown in Table 17. Furthermore, Figure 59 shows for the OP1 the relation between the *d*-axis stator current with the stator current and with the efficiency of the motor. In addition, Figure 60 shows for the OP1 the relation between the *d*-axis stator current with the iron and ohmic losses.
The results between the OP2 and the OP1 show a different variation between the I_{sd} for the case of MTPA and MTPLM techniques. For the OP2 the difference of I_{sd} between both techniques is 13 % and the I_{sd} difference in the OP1 between both techniques is 2.7 %. The explanation of that relies on the difference between the ohmic and iron losses in both operational points. When the ohmic losses are dominant, as the case of OP1, the difference in I_{sd} is lesser since both techniques consider the ohmic losses.

Table 17: At the operational point for the maximum torque M_{max} = 110 Nm; calculated parameters for the optimal points of MTPA and Loss Minimization techniques.

	I_{sd}	I_s	β	M_N	$P_{d,Cu,ac}$	$P_{d,Fe}$	P_d	P_m	P_e	η
	A	A	-	Nm	W	W	W	kW	kW	%
MTPA	-117.7	174.2	42.5°	110	2784	447	3233	47.6	50.8	93.63
MTPLM	-120.9	174.3	43.9°	110	2788	441	3231	47.6	50.8	93.64

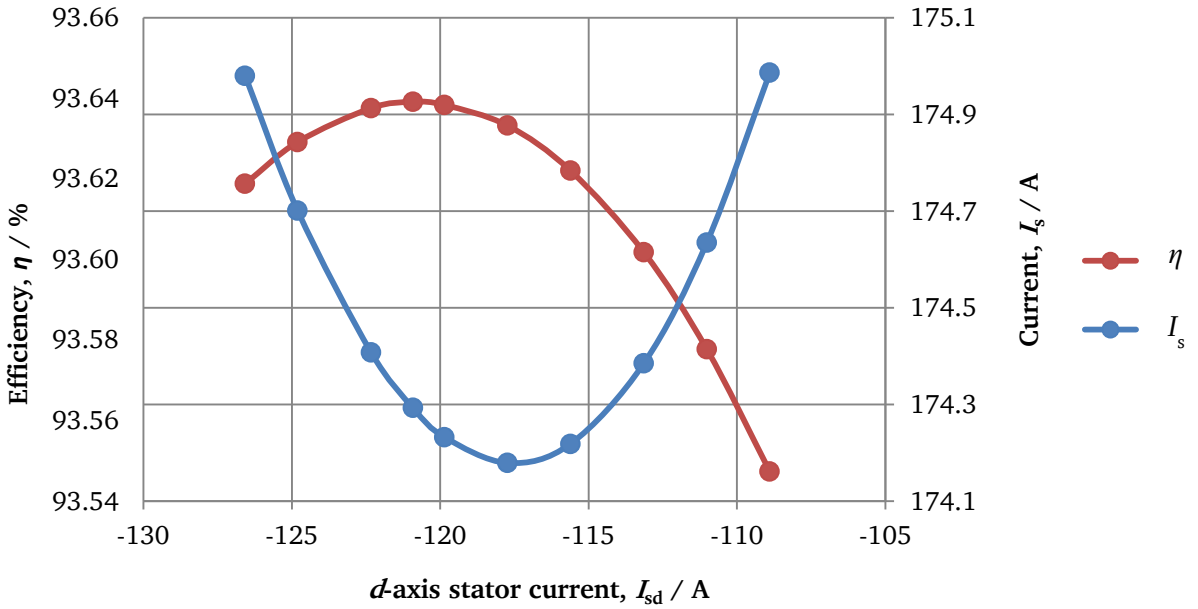

Figure 59: At the operational point for M_{max}; efficiency η and stator current I_s depending on the *d*-axis stator current I_{sd}.

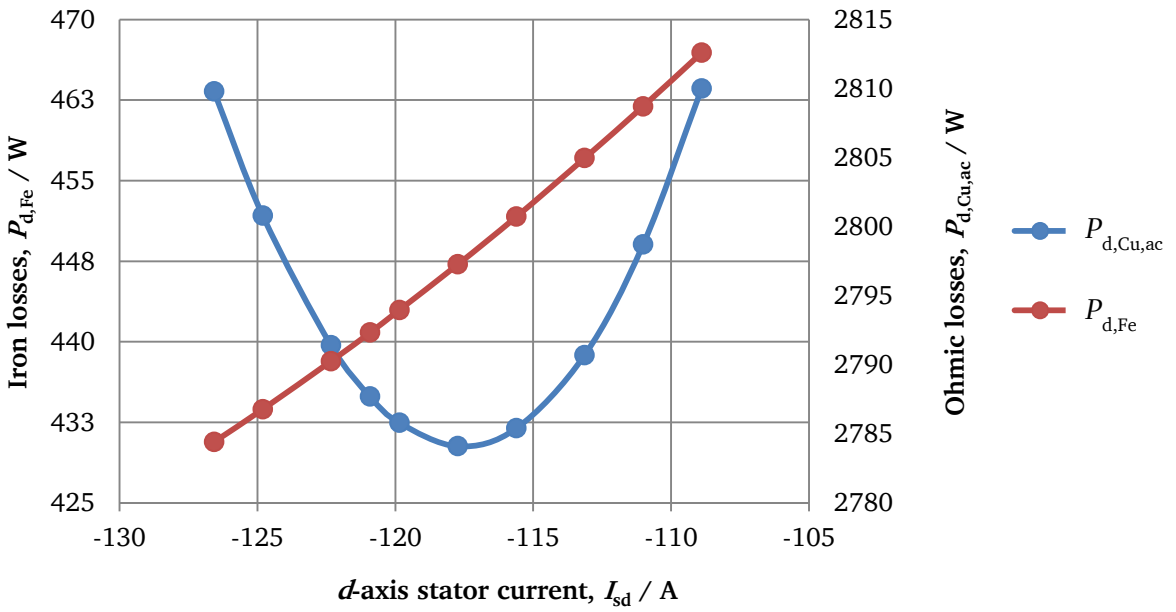

Figure 60: At the operational point for M_{max}; iron losses $P_{d,Fe}$ and ohmic losses $P_{d,Cu,ac}$ depending on the d-axis stator current I_{sd}.

5.4. Radial pressure for vibration and electromagnetic noise calculation

From the magnetic flux distribution, the radial and tangential components of the electromagnetic forces can be calculated by using the *Maxwell* stress tensor. In this thesis, the calculation of the radial pressure is achieved using the radial and the tangential components of the magnetic flux density with the equation 2.5-5. The Figure 61 shows the internal radial pressure caused by the radial electromagnetic forces at the no-load and load condition of the motor. As it can be seen, the radial pressure at load condition is much higher and distorted since the flux distribution in the air-gap for this condition is affected for the interaction by the magnetic flux coming from the magnets and the magnetic flux induced in the stator slots.

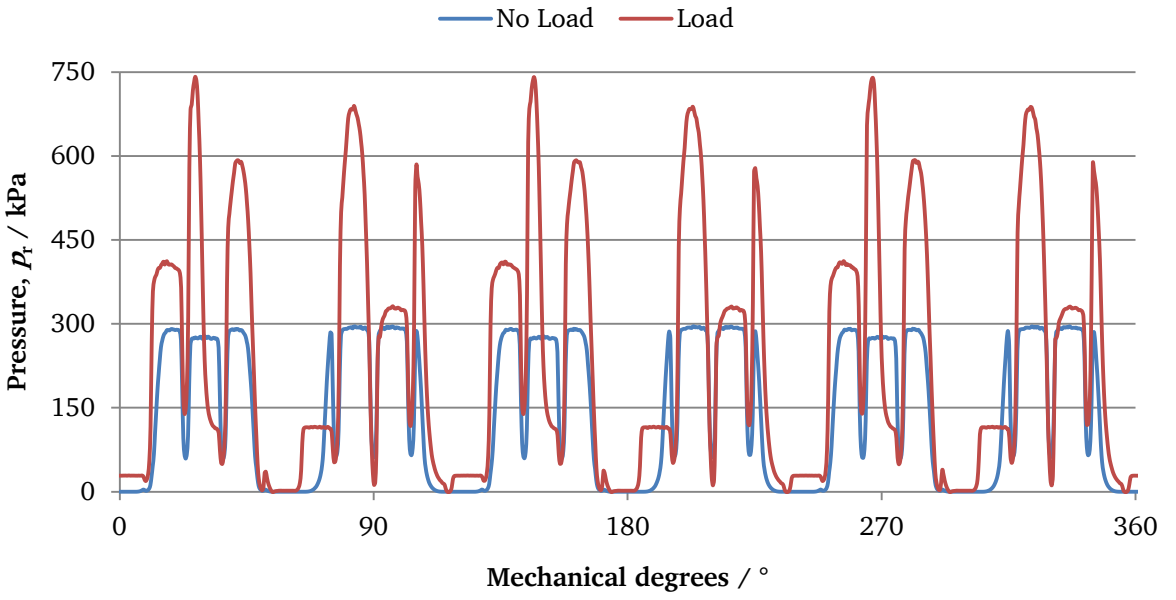

Figure 61: Radial pressure at no-load and load condition caused by the electromagnetic forces for the model q = 1.5.

A *Fourier* analysis of the radial pressure is carried out in order to see the harmonic content. The Figure 62 shows the harmonic components of the radial pressure at no-load and load condition. In addition, it can be noticed that the higher amplitudes for both condition of the motor are achieved with the 6^{th} and the 27^{th} harmonics, which both harmonic orders coincide with the number of poles and the number of stator slots of the motor. This fact confirms that the harmonic content of the radial pressure is going to be affected by the number of poles and stator slots. For the study of the vibrations and electromagnetic noise of the machine, the harmonic with the higher amplitude is of higher interest, since the higher the amplitude of the radial pressure, the higher will be the vibration of the stator core structure and hence the electromagnetic noise since it has been explained in section 2.9.

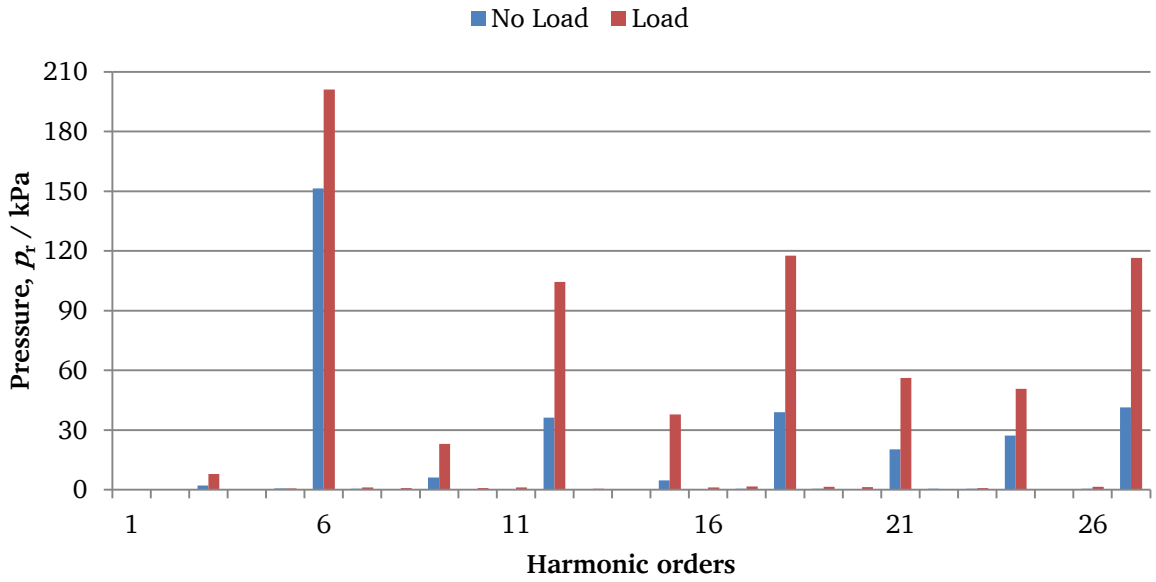

Figure 62: *Fourier* analysis of the radial pressure at no-load and load condition for the model $q = 1.5$.

6. Comparisons of four IPMSM models

6.1. Parameters comparison between the 4 models

The challenge of the present thesis is to reduce the cogging torque of an IPMSM by using a fractional number of stator slots per pole and phase $q = 1.5$. This reduction should be compared with a previous IPMSM with integer number of slots per pole and phase $q = 2$ without stepping and skewing the rotor. When this comparison is achieved, two more models have been designed and carried out in JMAG® to reduce the cogging torque as well. These two additional models are the step-skewed machine, which was built in this department, and a second fractional slot winding model with $q = 2.5$. For all models, the rotor structure was selected to be the same with 6 poles and the magnets in a V-shape configuration. Furthermore, the air-gap length and the outer stator diameter are also the same. In order to know the differences between the four models, the Table 18 shows the main parameters of each model and the Figure 63 shows the FEM models.

Table 18: The main parameters of the four IPMSM models.

	Original	Step-skewed	1st Variation	2nd Variation
Number of slots per pole and phase, q	2	2	1.5	2.5
Number of stator slots, Q	36	36	27	45
Angle between magnets, α_M / °	130	130	120	130
Number of pole pairs, p	3	3	3	3

The step-skewed model has the same parameters than the model with $q = 2$ (original). However, to reduce the cogging torque the step-skewed model has its rotor step-skewed in 5 steps with the angular difference of 2° between each step.

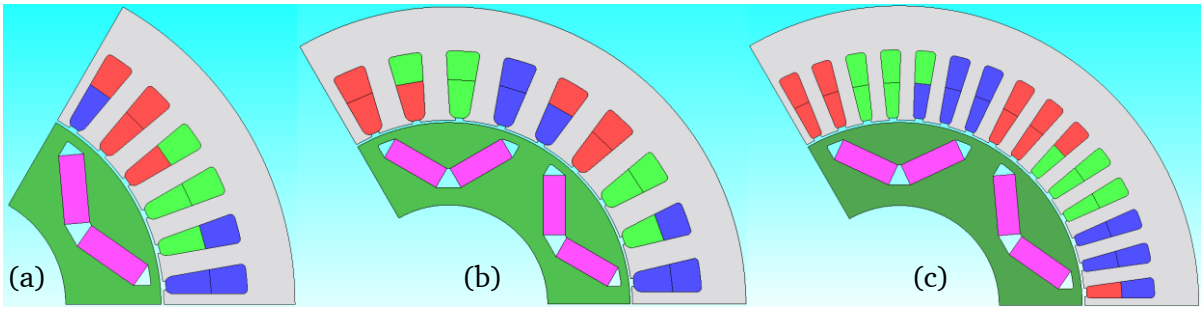

Figure 63: (a) Original model with $q = 2$, (b) 1st Variation model with $q = 1.5$, (c) 2nd Variation model with $q = 2.5$.

Table 19 shows the main calculated parameters for each model. The simulations were done for the rated operation with the rated torque 55 Nm and the rated speed 4167 min^{-1}. Although the four models have the same rotor structure and the same angle between magnets of 130°, the model with $q = 1.5$ has been selected with a magnet angle of 120° since it shows the best compromise of cogging torque and torque ripple reduction. At this condition, the results show an important reduction of the torque ripple from the original model with $q = 2$ to the model with $q = 1.5$. Furthermore, the steep-skewed model is the best one for the reduction of the torque ripple and the model with $q = 2.5$ reduces also the torque ripple from the original model with $q = 2$. It can be seen that each model has a different induced fundamental phase voltage U_{p1}, which is proportional to the winding factor k_w. In addition, the ohmic losses $P_{d,Cu,ac}$ vary since they are proportional to the square of the current phase I_s, the phase resistance R_s and the current displacement effect. The losses calculations consider

the ohmic losses with the current displacement effect, the iron losses with a punching factor and the friction losses. The sum of all losses for each model does not show a big difference between models and hence the efficiencies are quite similar for the four models.

Table 19: Calculated parameters for the 4 IPMSM models at rated operational point of M = 55 Nm and n = 4167 min^{-1}.

	Original	Step-skewed	1st Variation	2nd Variation
Number of slots per pole and phase, q	2	2	1.5	2.5
Rated speed, n / min^{-1}	4167	4167	4167	4167
Induced fundamental phase voltage, U_{p1} / V	71.4	70.6	73	75.4
Winding factor, k_w	0.934	0.934	0.9452	0.9514
Rated torque, M / Nm	55.04	55.01	55.14	55.13
Torque ripple, M_{rip} / %	10.6	1.86	2.45	3.1
Fundamental phase current, I_{s1} / A	90.72	92.63	89.5	85.21
Current phase, β / °	-35.4	-34.4	-33.4	-37.6
Stator winding self-inductance of d-axis per phase, L_d / µH	264	283	275	320
Stator winding self-inductance of q-axis per phase, L_q / µH	809	802	824	972
Phase resistance, R_s / mΩ	30.21	30.21	30.4	32.1
Ohmic losses, $P_{d,Cu,ac}$ / W	751	783	736	705
Iron losses, $P_{d,Fe}$ / W	348	351	324	344.4
Friction losses, $P_{d,fr}$ / W	2.1	2.1	2.1	2.1
Total losses, P_d / W	1101	1136	1062	1052
Efficiency, η / %	95.6	95.4	95.7	95.8

6.2. Magnetic flux distribution comparison between the 3 models

At no-load condition, the *Fourier* analysis of the magnetic flux distribution is carried out, for the original model with $q = 2$ and the models with $q = 1.5$ and $q = 2.5$. The Figure 64 shows a zoom of the *Fourier* analysis to emphasize the harmonic content that each model has. The integer slot model with $q = 2$ does not show any even harmonic. On the other hand, the fractional slot models with $q = 1.5$ and $q = 2.5$ shows odd and even harmonic orders. The rotor harmonic components, deduced from the *Fourier* analysis of the magnetic flux density, have to be equal to the harmonic components of the equivalent current loading to generate cogging torque, as it has been explained in section 2.8.5.

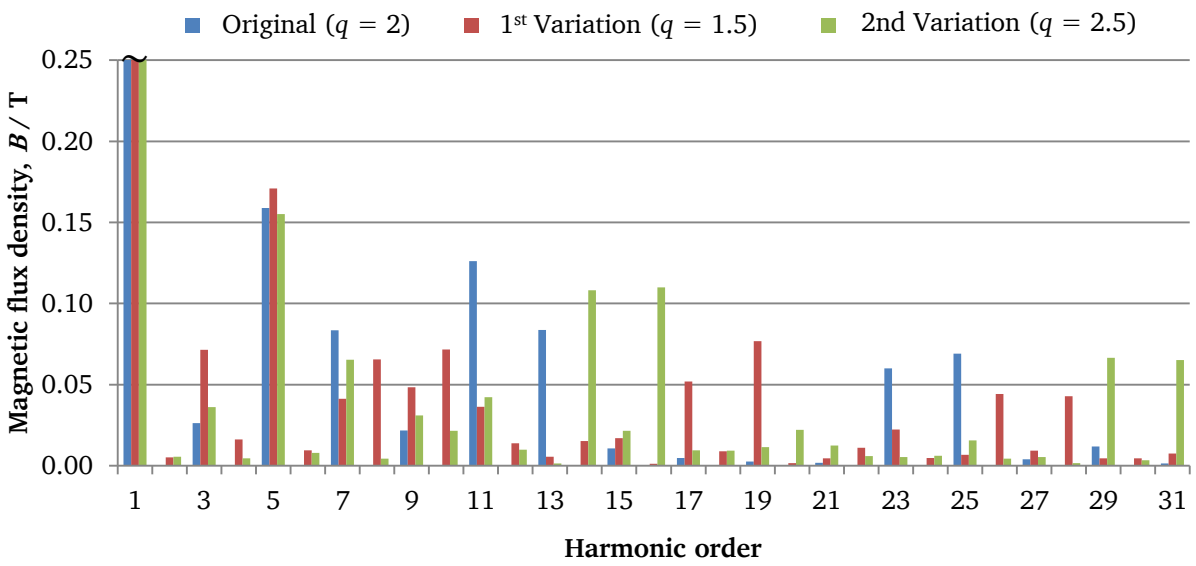

Figure 64: Fourier analysis of the magnetic flux distribution, at no-load, for the models with q = 2, q = 1.5 and q = 2.5.

The harmonics of the rotor μ which contribute to generate cogging torque have been calculated in Table 20. Thus, it can be seen that the amplitude of the harmonics of the rotor B_μ affects directly to the amplitude of the cogging torque M_{cog}, since $B_\mu \sim 1/\mu$ and $\lambda_l \sim 1/l$ and hence $M_{\text{cog}} \sim B_1 \cdot B_\mu \cdot \lambda_l$. The harmonics of the rotor μ have been calculated for the lowest integer parameter l, which gives the harmonics with the highest amplitudes. The Table 20 shows, for each model, the parameters that have been used to calculate the harmonics of the rotor μ.

Table 20: Calculated rotor harmonics μ that contribute to the generation of the cogging torque for each model.

	number of stator slots	number of pole pairs	parameter	dominant rotor harmonics μ
	Q	p	l	$\mu = \lvert 1 \pm l \cdot Q/p \rvert$
Original, q = 2	36	3	1	11, 13
1st Variation, q = 1.5	27	3	2	17, 19
2nd Variation, q = 2.5	45	3	2	29, 31

It can be seen in Table 20, that the model with integer slot winding shows the smallest l and the smallest μ harmonic orders. For that reason, the cogging torque amplitude will be the highest. For the cases of the fractional slot windings, it can be seen that when the number of slots per pole and phase is increased, the harmonic components from the rotor as well as the lower integer parameter l are also increased, which imply more reduction of the cogging torque amplitude.

6.3. Cogging torque comparison between the 4 models

Figure 65 shows the waves of the cogging torque for each model. The cogging torque percentage can be calculated as well as the periodicity of the cogging torque. For example, the original model with $q = 2$ shows 12 cogging torque periods for each electrical period and the model with $q = 1.5$ shows 18 cogging torque periods.

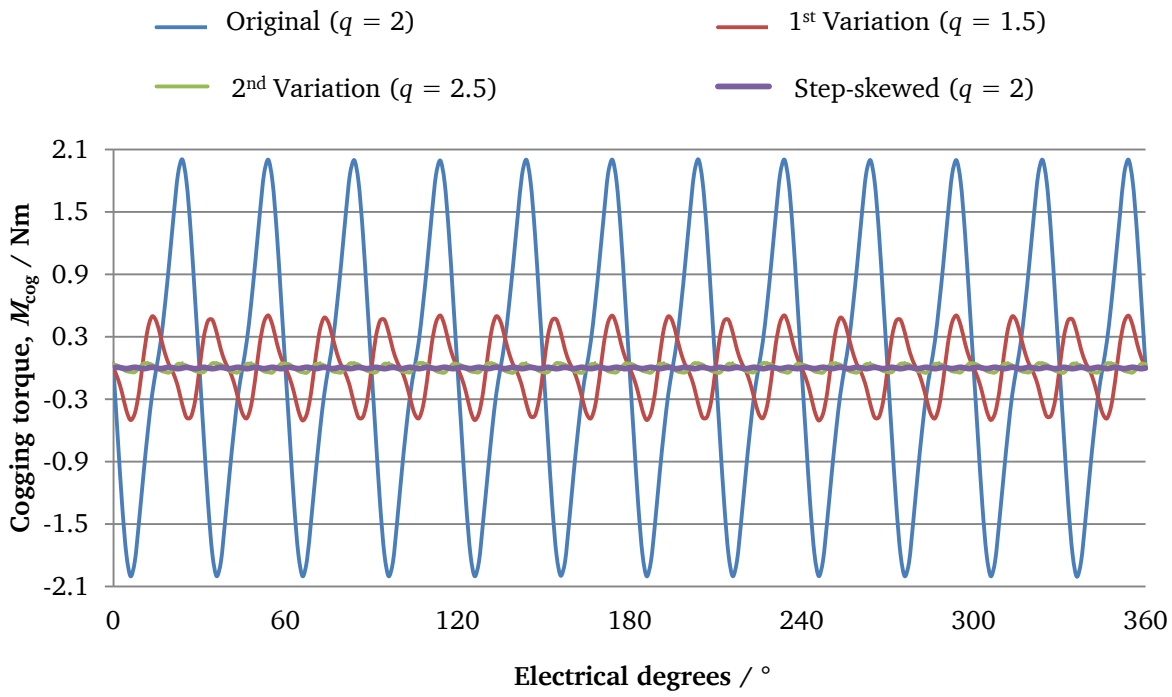

Figure 65: Cogging torque waves for each IPMSM model.

Table 21 shows the number of periods that each model has per electrical period, which have been calculated with equation 2.6-3. However, the periodicity of the step-skewed model has to be mathematically calculated due to the steps, and it has 60 periods. Table 21 also shows the percentage of the cogging torque respect of the rated torque of 55 Nm, for each model. The original model with $q = 2$ shows the fewest cogging torque periods per electrical period, although the amplitude is the highest with a 3.64 %. The model with $q = 1.5$ shows a great reduction in comparison with the original model with a cogging torque percentage of 0.85 %, although the highest reductions are with the step-skewed model and the model with $q = 2.5$, which show cogging torque percentages of almost 0 %.

Table 21: For each model, the calculated periodicity and percentages values of the cogging torque.

	Original	Step-skewed	1st Variation	2nd Variation
Number of slots per pole and phase, q	2	2	1.5	2.5
Number of stator slots, Q	36	36	27	45
Cogging torque periods per slot pitch N_{period}	1	-	2	2
Number of stator slots per electrical period	12	12	9	15
Total cogging torque periods per electrical period	12	60	18	30
Cogging Torque, M_{cog} / %	3.64	0.013	0.85	0.085

Figure 66 shows the periodicity of the cogging torque for 1 slot pitch, for each model:

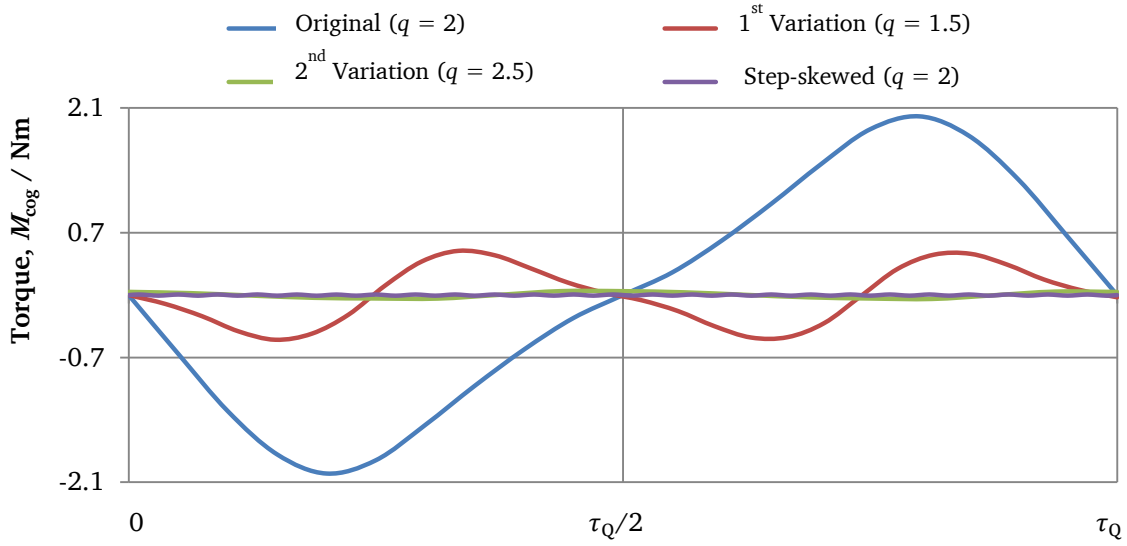

Figure 66: For each model, the periodicity of the cogging torque for 1 slot pitch.

As it has been explained in the theory in section 2.8.5, the main reason for using fractional slot windings is the fact that the rotor harmonic orders, which produce cogging torque, are higher in these fractional configurations than in the ones that use integer slot windings. In this situation, with higher rotor harmonic orders the amplitudes of the magnetic flux for each harmonic order will be smaller due to $B_\mu \sim 1/\mu$. Thus, a reduction of the cogging torque is expected since $M_{cog} \sim B_1 \cdot B_\mu \cdot \lambda_l$. Figure 67 shows a zoom of the *Fourier* analysis of the cogging torque for each model.

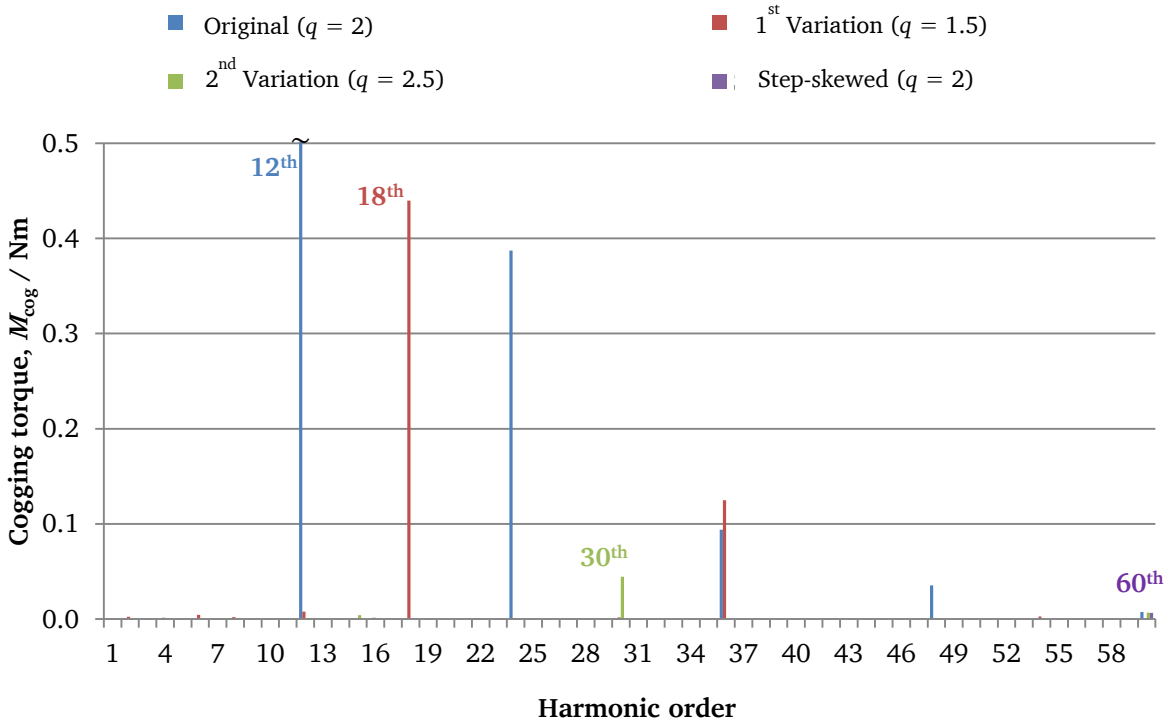

Figure 67: *Fourier* analysis of the cogging torque for each IPMSM model.

Table 22 shows, for each model, the highest harmonic amplitude and its order of the cogging torque. The most relevant harmonic for the model $q = 2$ is the order 12^{th} and for the model with $q = 1.5$ is the 18^{th}, which both coincide with the total cogging torque periods per electrical degree showed in Figure 65 and calculated in Table 21. Also it is seen the reduction of the cogging torque by using fractional slot windings. As Table 20 showed, using fractional slot windings makes that the rotor harmonic orders μ that produces cogging torque are higher than rotor harmonic orders that produce cogging torque in integer slot winding. Thus, a higher reduction of the cogging torque is achieved in fractional slot windings. In addition, when the number of stator slots per pole and phase is increased in the fractional slot windings, which is the case of the model with $q = 2.5$, the most relevant rotor harmonic orders that produces cogging torque are even higher, which contribute to a higher reduction of the cogging torque. It is noticed, for all models, that their most relevant harmonic component of the cogging torque coincides with the periodicity of the cogging torque per electrical period.

Table 22: For each model, the highest harmonic amplitude and its order of the cogging torque.

Model		harmonic order	$\widehat{M}_{cog}$ / Nm
Original	$q = 2$	12	1.782
Step-skewed	$q = 2$	60	0.007
1^{st} Variation	$q = 1.5$	18	0.42
2^{nd} Variation	$q = 2.5$	30	0.0446

6.4. Radial pressure comparison between 3 models

As it has been shown in theory 0, the stator structure suffers deformations caused by the radial forces from the magnetic flux distribution. The radial electromagnetic forces are calculated by using the *Maxwell* stress tensor. The radial forces are converted to radial pressure to have the force per unit area at any point of the air-gap. A *Fourier* analysis of the radial pressure is done to see the harmonic orders and their amplitudes. The highest amplitude of the *Fourier* analysis contribute to a highest displacement of the stator structure and hence more vibrations. Since the vibrations of the motor and hence the level of electromagnetic noise are proportional to the radial pressure, the radial pressure distribution is calculated from the magnetic flux density distribution. Figure 68 and Figure 69 show the calculated radial pressure distribution at no-load and load condition for each model.

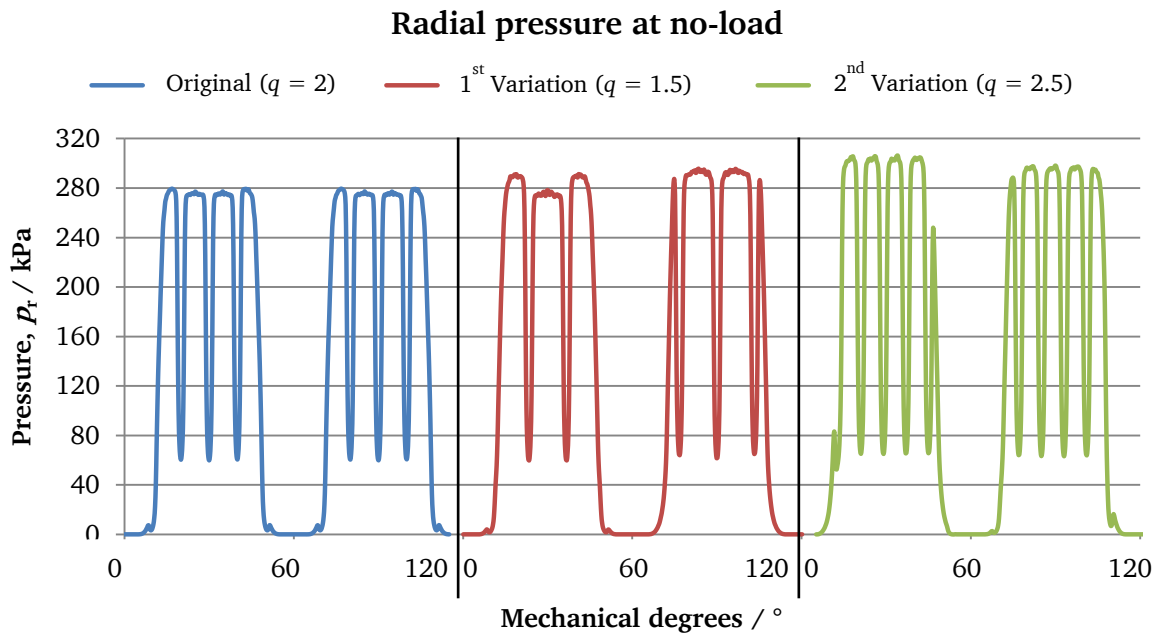

Figure 68: Radial pressure distribution calculated from the magnetic flux distribution, at no-load condition for each model.

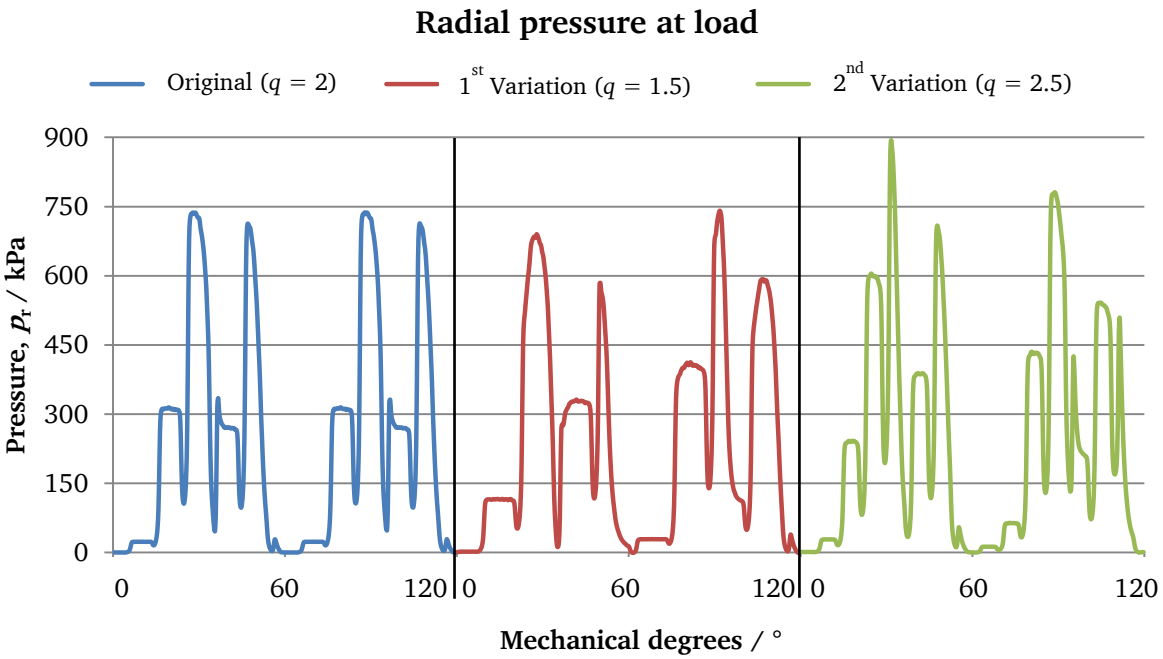

Figure 69: Radial pressure distribution calculated from the magnetic flux distribution, at load condition for each model.

A *Fourier* analysis of the radial pressure distribution has been carried out to see which harmonic components appear as well as their amplitudes. The Figure 70 and Figure 71 show the *Fourier* analysis results at no-load and load condition for each motor. The orders of the harmonics which give highest amplitudes of radial pressure are the 6^{th}, 27^{th}, 36^{th} and 45^{th}, which coincide with the number of poles and the number of stator slots. At no-load condition, the model which has highest internal radial pressure is the model with $q = 1.5$ and at load condition the highest amplitude of radial pressure can be found in the model with $q = 2.5$. It

can be said, from both graphs, that apparently the configurations with fractional slot windings produces more internal radial pressure which affects the stator core structure.

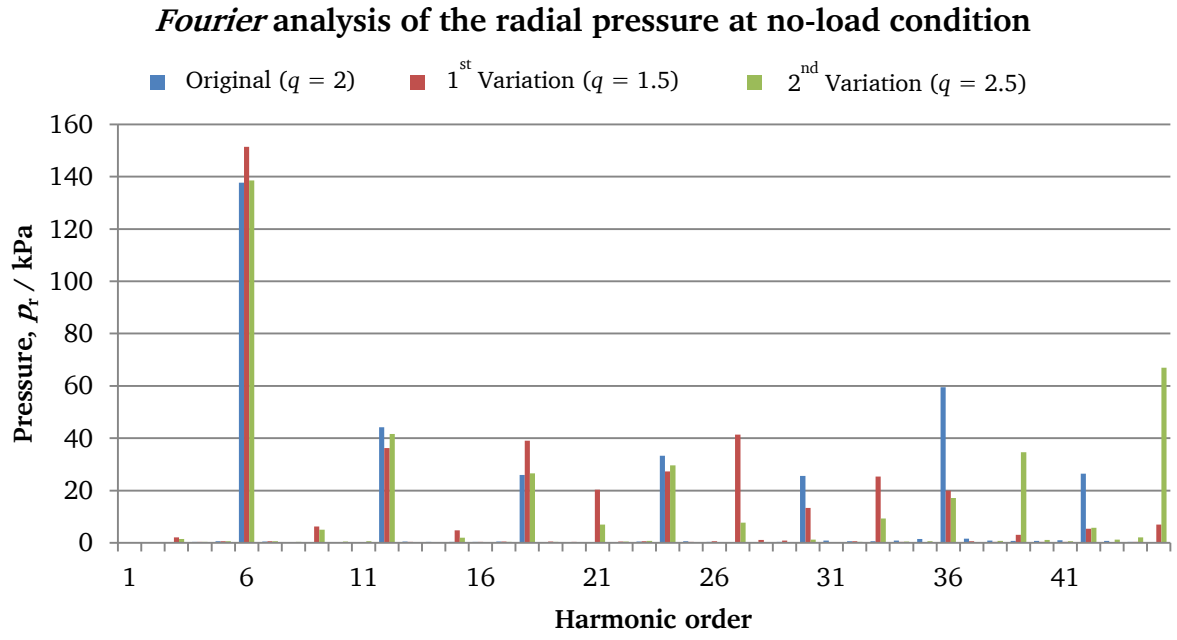

Figure 70: *Fourier* analysis of the radial pressure at no-load condition for the Original, 1st Variation and 2nd Variation.

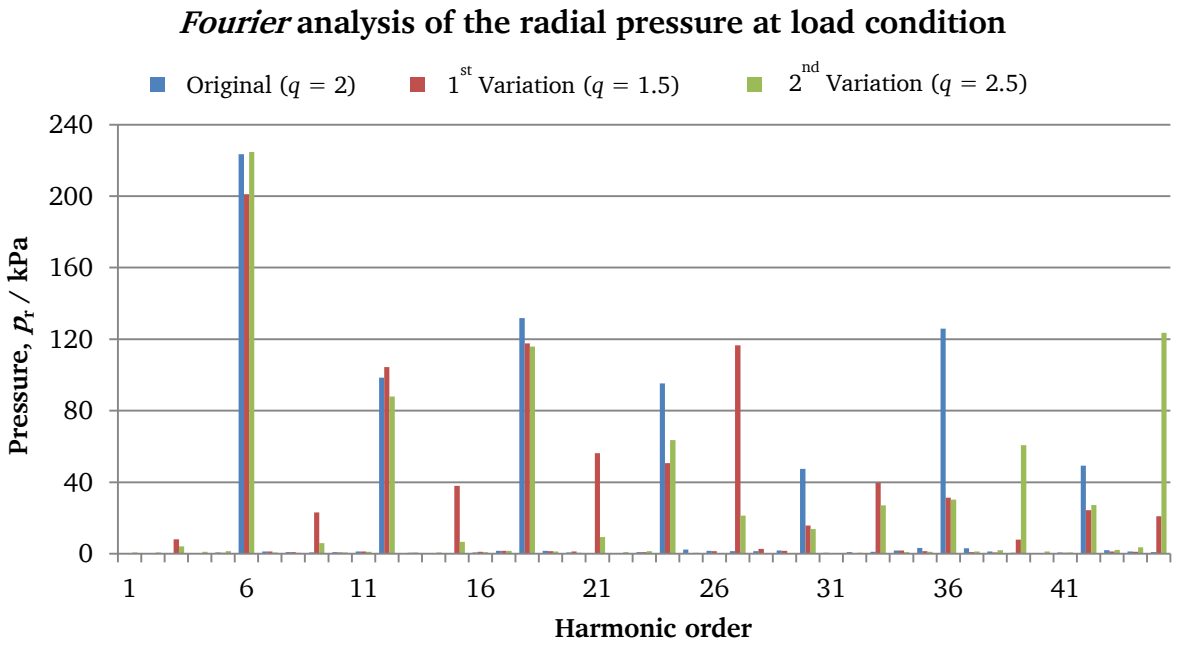

Figure 71: *Fourier* analysis of the radial pressure at load condition for the Original, 1st Variation and 2nd Variation.

6.5. Results comparison between 3 models

This chapter concludes with a comparison with the final values of all four models. Table 23 shows the percentages values of the cogging torque respect the rated torque and the torque ripple respect the average torque at rated load with $M = 55$ Nm and $n = 4167$ min^{-1}. This table also compares between each model the cogging torque, the torque ripple, the efficiency and the manufacturing associated costs by using a goodness scale of (--, -, 0, +, ++), where (--) is the worst case and (++) is the best case.

Table 23: Final comparison between the 4 IPMSM models in terms of cogging torque, torque ripple, efficiency and the manufacturing associated costs.

	Original	Step-skewed	1st Variation	2nd Variation
	$q = 2$	$q = 2$	$q = 1.5$	$q = 2.5$
Cogging torque $\widehat{M}_{\text{cog}} / M_{\text{N}}$	3.64 %	0.013 %	1.86 %	0.085 %
	-	++	+	++
Torque ripple $\widehat{M}_{\text{rip}} / M_{\text{av}}$	10.6 %	1.86 %	2.45 %	3.1 %
	--	++	+	0
Efficiency η	95.6 %	95.4 %	95.7 %	95.8 %
	+	+	++	++
Manufacturing associated costs	+	-	++	0

Table 23 shows the challenge of reducing the cogging torque and the torque ripple from the original model with $q = 2$ to the model with $q = 1.5$, which reductions are 76 % and 77 % respectively. Also an important reduction of the cogging torque is achieved by using the second model of fractional slot winding with $q = 2.5$, where the number of stator slots is higher than the model with $q = 1.5$. However, the torque ripple increases from the model with $q = 1.5$ to the model with $q = 2.5$. This shows that a reduction of the cogging torque does not imply a directly reduction of the torque ripple. The step-skewed rotor model shows the highest reduction of both cogging torque and torque ripple, for that their goodness scales are (++). The efficiency percentages do not change a lot between models, although the best efficiencies are achieved with the fractional slot winding models with $q = 1.5$ and $q = 2.5$. The step-skewed model is expensive due to the cost of manufacturing time, for that it has a (--) in this comparison. For the other models, the costs associated with the manufacturing rise as the number of stator slots of the machine increase. For that, the cheapest machines would be the model with $q = 1.5$.
At the end a compromise between the desired reduction of the cogging torque and torque ripple, the efficiency and the manufacturing associated costs has to be chosen. For the reasons explained above, the designed model with $q = 1.5$ has been selected as the model with has the best compromise with between the compared parameters in Table 23.

7. Conclusions

In order to design an interior permanent synchronous machine (IPMSM), the advantages and disadvantages of the machines have been studied and they have been taken into account for the designed model. These kinds of machines are preferable for a lot of applications, with a better performance. Therefore, the responses have to be accurate with low cogging torque and torque ripple. Thus, the cogging torque origins have been studied and the methods which help to reduce this phenomenon from the geometrical parameters of the motor have been analysed and implemented. The main method is the implementation of a fractional number of stator slots per pole and phase. Furthermore, other methods like the variation of the slot opening effect, the variation of the dimensions of the stator slots and the variation of the pole-arc to pole-pitch ratio have been studied and implemented too. Therefore, high reductions in cogging torque and torque ripple are achieved. The mechanical stress acting on the iron bridges in the rotor due to centrifugal forces, for magnets mounted inside the rotor, have been studied as well as the irreversible demagnetization of the magnets in a critical case of a three phase sudden short-circuit. For the design of the motor, it can be seen that in some cases the calculations differ from the integer slot winding such as the calculations of the stator windings with a distributed configuration with the consideration of the winding factor. When the design is made, a finite element analysis with the computational program JMAG® has been carried out to check the performance of the designed machine as well as the torque response and hence the cogging torque and the torque ripple. From the FE analysis, the magnetic flux distribution in the air-gap has been meticulously studied since it is used for the prediction of the electromagnetic forces. The radial and the tangential components of the electromagnetic forces, which are calculated by the *Maxwell* stress tensor, are used to calculate the internal radial pressure that the stator structure suffers.

The preferable utility of the IPMSM has been demonstrated since they show high efficiencies. Also they can generate additional reluctance torque due to the saliency ratio and by using the MTPA technic the current angle which gives the maximum torque can be achieved. In addition, the proposed model of IPMSM has the possibility of working in the OP3, which is $M = 46$ Nm and $n_{max} = 10000$ min^{-1}, with a strong field weakening control. It has been analytically proved, that using a fractional number of stator slots per pole and phase reduces the cogging torque since the rotor harmonic orders that contribute to its generation are high and hence their amplitudes are low. Thus, the reduction of the cogging torque from an integer slot winding motor to a fractional slot winding motor has been achieved with two models of fractional number of stator slots per pole and phase $q = 1.5$ and $q = 2.5$. The reductions of the cogging torque from the integer slot winding model with $q = 2$ to the two fractional slot winding models with $q = 1.5$ and $q = 2.5$ have been 76 % and 99 % respectively. The reductions of the torque ripple have been 77 % and 70 % respectively. These reductions have been achieved by using the main method of fractional number of slots per pole and phase and also by using two additional methods such as the optimization of the dimensions of the stator slots and the optimization of the pole-arc to pole-pitch ratio. The results also show that a reduction of the cogging torque does not mean a directly reduction of the torque ripple, as it could be seen in the variation of the stator slots method and the results of the model with $q = 2.5$. The highest reductions of cogging torque and torque ripple are achieved with the step-skewed model. However, the time and cost of manufacturing of this method is expensive, which makes the method of using a fractional number of stator slots per pole and phase a good candidate to reduce the cogging torque and torque ripple since it does not increase the manufacturing time. The radial pressure has been calculated, by using the *Maxwell* stress tensor, from the magnetic flux distribution in the air-gap. Thus, a comparison of the radial pressures between models can be achieved to predict which model can produce more vibrations and hence more electromagnetic noise.

The designed and proposed model with $q = 1.5$ to reduce the cogging torque and torque ripple is a good candidate from the 4 compared IPMSM since it shows a good compromise between both reductions of cogging torque and torque ripple as well as the efficiency and the manufacturing associated costs.

8. Annexes

8.1. Iron sheets material M270-35A from Sura®

Typical data for SURA® M270-35A

T	W/kg at 50 Hz	VA/kg at 50 Hz	A/m at 50 Hz	W/kg at 100 Hz	W/kg at 200 Hz	W/kg at 400 Hz	W/kg at 1000 Hz	W/kg at 2500 Hz
0,1	0,03	0,06	30,0	0,04	0,09	0,21	0,99	4,10
0,2	0,07	0,17	39,6	0,16	0,37	0,92	3,67	14,9
0,3	0,13	0,29	46,0	0,34	0,79	1,99	7,63	30,7
0,4	0,22	0,44	52,0	0,55	1,31	3,33	12,7	52,0
0,5	0,31	0,61	58,2	0,80	1,91	4,94	18,9	79,1
0,6	0,43	0,81	65,2	1,06	2,61	6,84	26,4	113
0,7	0,54	1,04	73,3	1,38	3,39	9,00	35,4	156
0,8	0,68	1,31	83,1	1,73	4,26	11,4	46,0	209
0,9	0,83	1,63	95,5	2,10	5,23	14,2	58,4	274
1,0	1,01	2,04	112	2,51	6,30	17,3	73,0	353
1,1	1,20	2,58	136	2,98	7,51	20,9	90,1	
1,2	1,42	3,38	178	3,51	8,88	24,9		
1,3	1,70	4,90	272	4,15	10,5	29,5		
1,4	2,12	9,64	596	4,97	12,5	35,4		
1,5	2,47	28,0	1700	5,92	14,9	41,8		
1,6	2,80	72,3	3880					
1,7	3,05	149	7160					
1,8	3,25	264	11600					

Loss at 1.5 T , 50 Hz, W/kg	2,47
Loss at 1.0 T , 50 Hz, W/kg	1,01
Anisotropy of loss, %	10
Magnetic polarization at 50 Hz	
H = 2500 A/m, T	1,54
H = 5000 A/m, T	1,65
H = 10000 A/m, T	1,77
Coercivity (DC), A/m	40
Relative permeability at 1.5 T	700
Resistivity, μΩcm	52
Yield strength, N/mm²	450
Tensile strength, N/mm²	565
Young's modulus, RD, N/mm²	185 000
Young's modulus, TD, N/mm²	200 000
Hardness HV5 (VPN)	215

RD represents the rolling direction
TD represents the transverse direction
Values for yield strength (0.2 % proof strength) and tensile strength are given for the rolling direction
Values for the transverse direction are approximately 5% higher

cogent
Surahammars Bruks AB

June 2008

8.2. Design parameters for the original model with $q = 2$ and $Q = 36$.

IPMSM – $q = 2$			
Q	36	-	number of stator slots
q	2	-	number of slots per pole and phase
m	3	-	number of stator phases
p	3	-	number of pole pairs
δ	0.6	mm	air-gap length
d_{si}	92.8	mm	stator inner diameter
l_{Fe}	140	mm	iron stack length
τ_p	48.6	mm	pole pitch
W	40.5	mm	coil span
$k_{p,1}$	0.966	-	pitch factor
$k_{d,1}$	0.966	-	distribution factor
$k_{w,1}$	0.934	-	winding factor
N_s	24	-	number of turns per phase
N_c	12	-	number of turns per coil
a	6	-	number of parallel branches
a_i	3	-	number of parallel wires per turn
A_s	46645	A/m	current loading
I_s	94.44	A	phase current
J	10.72	A/mm^2	current density
I_c	15.73	A	current coil
A_{Cu}	1.56	mm^2	copper area of a coil
d_{Cu}	0.813	mm	copper diameter of a wire
A_{Qs}	90	mm^2	area of a stator slot
k_f	0.416	-	fill factor
b_{st}	4.6	mm	breadth of a stator tooth
h_{sl}	17.7	mm	height of a slot
h_{ys}	10	mm	height of the stator yoke
R_s	30.21	mΩ	stator phase resistance at 100 °C
l_b	115.63	mm	winding overhang
$L_{\sigma b}$	14.2	μH	inductance of the winding overhangs

8.3. Design parameters for the 2nd Variation model with $q = 2.5$ and $Q = 45$.

IPMSM – $q = 2.5$			
Q	45	-	number of stator slots
q	2.5	-	number of slots per pole and phase
m	3	-	number of stator phases
p	3	-	number of pole pairs
δ	0.6	mm	air-gap length
d_{si}	92.8	mm	stator inner diameter
l_{Fe}	140	mm	iron stack length
τ_{p}	48.6	mm	pole pitch
W	45.36	mm	coil span
$k_{\mathrm{p,1}}$	0.9945	-	pitch factor
$k_{\mathrm{d,1}}$	0.9567	-	distribution factor
$k_{\mathrm{w,1}}$	0.9514	-	winding factor
N_{s}	25	-	number of turns per phase
N_{c}	5	-	number of turns per coil
a	3	-	number of parallel branches
a_{i}	6	-	number of parallel wires per turn
A_{s}	46086	A/m	current loading
I_{s}	89.58	A	phase current
J	10.85	A/mm^2	current density
I_{c}	29.86	A	current coil
A_{Cu}	3.115	mm^2	copper area of a coil
d_{Cu}	0.813	mm	copper diameter of a wire
A_{Qs}	68.8	mm^2	area of a stator slot
k_{f}	0.453	-	fill factor
b_{st}	3.7	mm	breadth of a stator tooth
h_{sl}	17	mm	height of a slot
h_{ys}	10	mm	height of the stator yoke
R_{s}	32.1	mΩ	stator phase resistance at 100 °C
l_{b}	119.83	mm	winding overhang
$L_{\sigma\mathrm{b}}$	16.3	µH	inductance of the winding overhangs

References

[1] J. Pyrhönen, T. Jokinen and V. Hrabovcová, *Design of rotating electrical machines*, The Atrium, Southem Gate, Chichester, United Kindom: John Wiley & Sons, Ltd, 2008.

[2] A. Ahmed, *Maximum Torque Per Ampere (MTPA) control for permanent magnet synchronous machine drive system*, Akron, Ohio, USA, 2013.

[3] A. Binder, Lecture notes: *Motor Development for Electrical Drive Systems*, Darmstadt, Hessen, Germany, 2010.

[4] A. Binder, T. Schneider and M. Klohr, "Fixation of Buried and Surface-Mounted Magnets in High-Speed Permanent-Magnet Synchronous Machines," in *2016 IEEE Transactions on Industry Applications,* vol. 42, no. 4, pp. 1031-1037, July/August 2006.

[5] J. An and A. Binder, "Analysis of sudden short-circuit current of interior permanent magnet synchronous machines," in *International Symposium on Power Electronics, Electrical Drives, Automation and Motion*, Anacapri, Italy, pp. 1324-1329, June 2016.

[6] E. Muljadi and J. Green, "Cogging Torque Reduction in a Permanent Magnet Wind Turbine Generator," in *21st American Society of Mechanical Engineers Wind Energy Symposium*, Reno, USA, Janualy 2002.

[7] R. Islam and I. Husain, "Analytical Model for Predicting Noise and Vibration in Permanent-Magnet Synchronous Motors," in *IEEE Transactions on Industry Applications,* vol. 46, no. 6, pp. 2346-2354, November/December 2010.

[8] M. Chabchoub, I. Ben Salah, G. Krebs, R. Neji and C. Marchand, "PMSM Cogging Torque Reduction: Comparison between different shapes of magnet," in *1st International Conference on Renewable Energies and Vehicular Technology,* Hammamet, pp. 206-211, 2012.

[9] C. Bianchini, F. Immovilli, E. Lorenzani, A. Bellini and M. Davoli, "Review of Design Solutions for Internal Permanent-Magnet Machines Cogging Torque Reduction," in *IEEE Transactions on Magnetics,* vol. 48, no. 10, pp. 2685-2693, October 2012.

[10] Pinky K and P. R. S. V. , "Torque Improvement in IPMSM for Electric Vehicle Application," in *International Conference on Control, Communication & Computing India*, Trivandrum, India, pp. 224-229, 2015.

[11] R. Islam, I. Husain, A. Fardoun and K. McLaughlin, "Permanent-Magnet Synchronous Motor Magnet Designs With Skewing for Torque Ripple and Cogging Torque Reduction," in *IEEE Transactions on Industry Applications,* vol. 45, no. 1, pp. 152-160, January/February 2009.

[12] M. Sanada and S. Morimoto, "Efficiency Improvement at High-Speed Operation using Large Air-gap Configuration for PMSM," in *Proceedings of the 2008 International Conference on Electrical Machines*, Vilamoura, 2008.

[13] A. Binder, *Elektrische Maschinen und Antriebe* [Electrical Machines and Drives] (in German), Heidelberg, Hessen, Germany: Springer, 2012.

[14] J. F. Gieras and M. Wing, *Permanent Magnet Motor Technology*, Second Edition Hrsg., New York, New York, USA: Marcel Dekker, Inc., 2002, p. 590.

[15] P. Salminen, *Fractional Slot Permanent Magnet Synchronous Motors for Low Speed Applications*, dissertation, Lappeenranta, Finland, 2004.

[16] W. Ren , Q. Xu and Q. Li, "Reduction of Cogging Torque and Torque Ripple in Interior PM Machines with Asymmetrical V-type Rotor Design," in *IEEE Transactions on Magnetics,* vol.52, no. 7, pp. 1-5, July 2016.

[17] A. Vagati, G. Pellegrino and P. Guglielmi, "Comparison between SPM and IPM motor drives for EV application," in *19th International Conference on Electrical Machines*, Rome, Italy, 2013.

[18] C. Z. Deák, *Modular Permanent-Magnet Synchronous Motors with high Electromagnetic Utilization*, dissertation, Darmstadt, Hessen, Germany, 2011.

[19] Y.-Y. Choe, S.-Y. Oh, S.-H. Ham, I.-S. Jang, S.-Y. Cho, J. Lee and K.-C. Ko, "Comparison of Concentrated and Distributed Winding in an IPMSM for Vehicle Traction," in *2nd International Conference on Advances in Energy Engineering*, 2012.

[20] C. Carvajal Almendros, *Design and Analysis of a Fractional-Slot Concentrated-Wound Permanent-Magnet-Assisted Synchronous Reluctance Machine*, dissertation, Stockholm, Sweden, 2015.

[21] "Drives & Controls: *Single-tooth motors could bite into the EV market*," (9 July 2013) [Online]. Available: http://www.drivesncontrols.com/news/fullstory.php/aid/4009/Single-tooth_motors_could_bite_into_the_EV_market.html.

[22] P. B. Reddy, A. M. EL-Refaie and K.-K. Huh, "Effect of Number of Layers on Performance of Franctional-Slot Concentrated-Windings Interior Parmanent Magnet Machines," in *8th International Conference on Power Electronics*, Jeju, South Korea, pp. 1921-1928, 2011.

[23] A. Binder, Lecture notes: *Energy Converters - CAD and Systems Dynamincs*, Darmstadt, Hessen, Germany, 2010.

[24] A. Iraolagoitia and P. Fernández, "Comparative study of PMSM with integer-slot and fractional-slot windings," in *19th International Conference on Electrical Machines*, Italy, Rome, 2010.

[25] "Your Electrical Home: *Single Layer and Double Layer Winding*," (24 August 2012) [Online]. Available: http://yourelectrichome.blogspot.de/2012/08/single-layer-and-double-layer-winding.html.

[26] Y. Asano, Y. Honda, H. Murakami, Y. Takeda and S. Morimoto, "Novel Noise Improvement Technique for a PMSM with concentrated Winding," *Power Conversion Conference,* vol. 2, pp. 460-465, Osaka, 2002.

[27] L. W. Matsch, "Capacitors, Magnetic Circuits and Transformers: *Inductance in terms of magnetic reluctance and magnetic permeance*," [Online]. Available: http://www.vias.org/matsch_capmag/matsch_caps_magnetics_chap4_05.html.

[28] N. Bianchi and S. Bolognani, "Design Techniques for Reducing the Cogging Torque in Surface-Mounted PM Motors," in *IEEE Transactions on Industry Applications,* vol. 38, no. 5, pp. 1259-1265, September/October 2002.

[29] N. Levin, S. Orlova, V. Pugachov, B. Ose-Zala and E. Jakobsons, "Methods to Reduce the Cogging Torque in Permanent Magnets Synchronous Machines," *ELEKTRONIKA IR ELEKTROTECHNIKA,* vol. 19, no. 1, pp. 23-26, 2013.

[30] M. Okubo and M. Kawamura, "Brushless Motor with Skewed Rotor Segments". United States Patent US 7,906,880 B2, 15 March 2011.

[31] Z. Q. Zhu, S. Ruangsinchaiwanich, N. Schofield and D. Howe, "Reduction of Cogging Torque in Interior-Magnet Brushless Machines," in *IEEE Transactions on Magnetics,* vol. 39, no. 5, pp. 3238-3240, September 2003.

[32] Pushek Madaan, "EDN Network: *Brushless DC Motors - Part I: Construction and Operating Principles*," (11 February 2013), [Online]. Available: http://www.edn.com/design/sensors/4406682/Brushless-DC-Motors---Part-I--Construction-and-Operating-Principles.

[33] Y. Chen, J. Shen and Z. Fang, "Topology and Preliminary Design of Slotless Brushless DC Motor," in *IEEE International on Electric Machines and Drives Conference Record, 1997. IEEE International,* Milwaukee, Wisconsin, USA, 1997.

[34] L. Dosiek and P. Pillay, "Cogging Torque Reduction in Permanent Magnet Machines," in *IEEE Transactions on Industry Applications,* vol. 43, no. 6, pp. 1565-1571, November/December 2007.

[35] S.-H. Han, T. M. Jahns, W. L. Soong, M. K. Güven and M. S. Illindala, "Torque Ripple Reduction in Interior Permanent Magnet Synchronous Machines Using Stator with Odd Number of Slots per Pole Pair," in *IEEE Transactions on Energy Conversion,* vol. 25, no. 1, pp. 118-127, March 2010.

[36] D. G. Dorrell and M. Popescu, "Odd Stator Slot Numbers in Brushless DC Machines - An Aid to Cogging Torque Reduction," in *IEEE Transactions on Magnetics,* vol. 47, no.10, pp. 3012-3015, October 2011.

[37] G. Dajaku and D. Gerling, "New Methods for Reducing the Cogging Torque and Torque Ripple of PMSM" in *2014 4th International Electric Drives Production Conference (EDPC),* Nuremberg, Germany, 2014.

[38] Microsemi Corporation, "Park, Inverse, Park and Clarke, Inverse Clarke Transformations," [Online]. Available: http://www.microsemi.com/document-portal/doc_view/132799-park-inverse-park-and-clarke-inverse-clarke-transformations-mss-software-implementation-user-guide.

[39] T. M. Jahns, "Flux-Weakening Regime Operation of an Interior Permanent-Magnet Synchronous Motor Drive," in *IEEE Transactions on Industry Applications,* vol. IA-23, no. 4, pp. 681-689, July 1987.

[40] WÜRTH. [Online]. Available: http://media.wuerth.com/stmedia/shop/masterpages0000/LANG_de/09139.pdf.

[41] J. Martinez Miralles, *Tema 2. Fallada per fatiga mecànica* [Unit 2. Failure due to mechanical fatigue] (in Catalan). ETSEIB, Barcelona, Catalunya, Spain, 2014.

[42] F. Endert, T. Heidrich, U. Schwalbe, T. Szalai and S. D. Ivanov, "Effects of current displacement in a PMSM traction drive with single turn coils," in *IEEE International on Electric Machines & Drives Conference, 2013 IEEE International,* Chicago, Illinois, USA, pp. 160-165, 2013.

[43] G. Bergmann, *Five-Axis Rotor Magnetic Suspension with Bearingless PM Motor Levitation Systems*, dissertation, Darmstadt, Hessen, Germany: Shaker, 2013.

[44] Cogent Surahammars Bruks AB, Typical data for SURA® M270-35A, June 2008, Germany. [Online]. Available: http://cogent-power.com/cms-data/downloads/m270-35a_1.pdf.

[45] VACUUMMSCHMELZE, Material Property of VACODYM 863 TP, 6 March 2015. [Online]. Available: http://www.vacuumschmelze.com/en/products/permanent-magnets-assemblies/permanent-magnets/nd-fe-b/vacodym/vacodym-863-tp.html.

[46] T. Bariša, D. Sumina and M. Kutija, "Comparison of maximum torque per ampere and loss minimization control for the interior permanent magnet synchronous generator," in *2015 International Conference on Electrical Drives and Power Electronics (EDPE),* Tatranska Lomnica, Slovakia, pp. 497-502, 2015.